Z-scan methods for ultrashort pulsed laser microprocessing of transparent materials

Francesc Caballero Lucas

Z-scan methods for ultrashort pulsed laser microprocessing of transparent materials

Francesc Caballero Lucas

UNIVERSITAT DE BARCELONA

Z-scan methods for ultrashort pulsed laser microprocessing of transparent materials

Memòria presentada per optar al grau de doctor per la
Universitat de Barcelona

Programa de doctorat en Nanociències

Autor: Francesc Caballero Lucas
Directors: Juan Marcos Fernández Pradas, Pere Serra Coromina

Tutor: Pere Serra Coromina

Barcelona, Juliol de 2019

UNIVERSITAT DE BARCELONA

Departament de Física Aplicada
Martí i Franquès 1, 08028 Barcelona

A les meves famílies

Acknowledgements

Aquesta secció està dedicada a fer un petit agraïment a la gent que ha tingut un paper més destacat en la consecució de l'elaboració d'aquesta tesi doctoral. Sense la col·laboració, ajuda i motivació de totes aquestes persones (i segurament d'alguna altra que malauradament em deixaré de mencionar) no hagués estat possible la realització de tal fita. És per aquests motius que vull aprofitar l'ocasió i reconèixer breument en les següents línies una gran part de les aportacions rebudes, ja sigui pel temps que m'han dedicat en l'exigent tasca de la recerca o pel recolzament que n'he rebut al llarg d'aquests anys. Així doncs totes les persones incloses en aquesta secció formen part de la feina presentada en aquesta tesi.

En primer lloc, voldria agrair de forma especial al Dr. Pere Serra el seu oferiment per a la realització del treball de màster i de la tesi doctoral al seu grup de recerca. Tant ell com el Dr. Juan Marcos Fernández han estat els meus directors de tesi, complint aquest càrrec en tot moment mitjançant un acompanyament que s'ha estès al llarg de totes les etapes d'aquest llarg procés de recerca. A part de ser uns excel·lents professors com afortunadament vaig poder comprovar durant el desenvolupament de la Llicenciatura, igualment he tingut la sort de poder comptar amb el seus coneixements i suport durant la recerca així com a l'hora de prendre decisions o demanar consell. Per això els vull reconèixer tot el temps dedicat en la meva formació en tots els aspectes.

Per altra banda també cal agrair a la resta de professors del Departament de Física Aplicada la seva ajuda i col·laboració, especialment durant les pràctiques en laboratoris realitzades durant el doctorat associades a l'ajuda predoctoral rebuda, així com el seu tracte proper com a un membre més del departament.

The research stay at Keio University in Tokyo, Japan is the reason to thank Dr. Mitsuhiro Terakawa for his trust and dedication during the three months I spent at his laboratory. The amazing time spent there was a result of the combination of the

friendly environment found in his group and endorsed by him plus the possibility of carrying out experiments with a different experimental setup and following other strategies. I would also like to thank the other members of the research group which also made the stay a really nice experience. Specially, I want to name Naonari, Taiga, Manan and Dr. Yasutaka Nakajima for their priceless help both inside the lab and outside. 本当にありがとうございます。

Also with regard to the research stay in Japan, I would like to thank all the friends in Tokyo for their warming welcome and contributing to the great summertime I enjoyed there. In particular, I want to thank Marcelo for his kindness and cheerfulness. Muito obrigado.

També vull donar les gràcies i dedicar aquesta tesi i algunes paraules d'agraïment a totes les següents persones:

A tot el personal de la secretaria del Departament, per la seva dedicació en les tasques associades a tràmits administratius que ha estat de gran ajuda, amb especial menció a les persones amb qui he compartit més temps: la Maite i en Jordi.

Als companys de departament, pels moments compartits i per la seva ajuda i disposició, amb especial menció a en David, company també de despatx fins fa poc.

Als estudiants tant de grau, màster com de doctorat que són o han estat membres del grup de recerca, per la seva col·laboració i el bon ambient que han creat. Cal mencionar en aquest grup especialment en Pol, company de grup i de despatx ja fa un bon temps i amb el que hem compartit un bon nombre d'experiències i peripècies tant al laboratori com durant la resta de temps en dinars, congressos, viatges i trobades. El seu estil de treball i força de voluntat sempre han tingut la meva més sincera admiració.

A la Dra. Leyre Martínez de Olcoz, que tot i les formalitats que cal complir en aquesta secció d'agraïments de la tesi doctoral degut al títol que posseeix, sempre l'he considerada una de les persones més accessibles i properes que he conegut. La seva presència al despatx de la universitat durant els primers anys del doctorat ha estat una experiència memorable que guardo amb molta estima.

Al Dr. Camilo Florian, un altre company al que les formalitats del tractament no m'impedeixen de descriure com una persona amb la que he compartit grans moments, tant com a company de despatx, del grup de recerca i com a bon amic. La seva organització, eficiència, amabilitat i bon humor sempre han estat objecte d'admiració per part meva. Així doncs, la seva finalització del doctorat i de la recerca conjunta amb ell va consistir un punt d'inflexió degut a la seva total disposició i ajuda en tot moment. L'agraïment especial és en aquest cas per la gran quantitat de temps i d'activitats que vam compartir juntament amb la seva inesgotable ajuda i col·laboració. Muchas gracias, Camilo.

Als meus amics i companys, especialment pels bons moments gaudits plegats jugant a jocs de taula i aprofitant els caps de setmana junts, amb especial èmfasi cap a en Ricard i en Joan, sempre disposats a oferir casa seva per passar-ho bé.

A l'Alonso, pel seu somriure omnipresent, la seva presència tranquil·la i el seu bon humor que m'han acompanyat aquests últims mesos.

A en Dani, company en la meva vida des de ja fa molts anys i amb el que he compartit molts moments especials. La seva admiració incondicional i incansable generositat han estat sempre presents i de gran ajuda per arribar fins aquí.

I finalment a la meva família, tant la considerada directa com l'extensa, per tot el suport rebut especialment aquests anys però durant tota la meva vida. I amb una menció destacada als meus pares, a qui he d'agrair el seu suport incondicional i esforç dedicat per a què sempre hagi pogut gaudir de la millor educació possible. L'agraïment es difícil de verbalitzar en paraules per tot el significat que conté. Moltes gràcies de tot cor.

Contents

Outline

Digital manufacturing commenced an authentic revolution that is transfiguring industrial fabrication processes beginning with the very early stages of research and development, and extending to all the steps of production, commercialization and marketing owing to the feasible opportunities that digital process innovation entails. Among these, adaption and implementation of the demands of the market and even individual customization required by consumers to satisfy their use of the produced goods and provided services stand out. The reason for this is that digital manufacturing offers the extremely convenient option of performing design changes through modification of virtual prototypes in computerized systems. This possibility obviously contrasts with the traditional approach of altering an already fabricated physical prototype, the common strategy applied in manufacturing processes previously to the implementation of digital techniques. This fact resulted in faster, efficient and more precise production processes, specially needed as the possibilities offered by digital manufacturing increase the complexity of the processes involved for production of goods and services that every time satisfy their purposes in a more successful and convenient way.

One of the requirements of the novel digital techniques that scientists and engineers must continuously address is miniaturization, which constitutes a basic strategy in prominent areas such disparate as electronics, all the fields related to biomedical studies like pharmaceutics and chemical-biological sensing, and the development of functional materials to name a few. Lasers are a versatile tool that can meet the exposed demands of flexibility, speed, resolution and compatibility with processing large regions of materials with high accuracy. Since their invention in 1960 by Theodore H. Mainman, lasers have been utilized in an unstoppably growing number of applications and hence can be found in areas such diverse as industrial manufacturing, medicine, telecommunications and natural sciences. The principal advantages of laser light have their origin in its high directionality (collimation) and high monochromaticity. The combination of these properties makes

possible the generation of high intensities that can be focused into extremely small volumes, what promotes lasers as an ideal tool for the accurate processing of almost any kind of materials at the micro- and nanoscale.

Laser direct-write microprocessing through ablation is the most straightforward microprocessing technique since it just consists in the irradiation of a material with a focused laser beam. Under the adequate conditions, the intense absorbed laser energy causes the alteration of a small portion of material, leaving a modified area at the irradiated spot. In many instances, the principal goal in microprocessing is achieving the highest possible spatial resolution. Heat transfer from the absorbed laser energy to the material is often detrimental for this aim. This situation can be dodged with the use of ultrashort laser pulses. Their extremely short duration delivers all the laser pulse energy to the material in a period of time shorter than the lattice thermal relaxation time, leading to a radical reduction of the undesired heat dissipation beyond the irradiated region. Moreover, several applications exclusively require superficial ablation or processing of the material. This does not suppose any problem when the processed material is opaque to the laser radiation at its wavelength, whereas for a transparent material it constitutes a true challenge due to the need of precisely controlling the position where the laser energy is delivered to secure that absorption effectively takes place at the processed material surface, without modifying the bulk material. Development of strategies that make possible this control is crucial in these circumstances.

Recently the use of femtosecond lasers has gained attention as a result of the recognition to Gérard Mourou and Donna Strickland with the award of the Nobel Prize in Physics 2018 "for their method of generating high-intensity, ultra-short optical pulses". According to the awarding motivations, the innumerable areas of application of ultrashort laser pulses have not yet been completely explored, but their possibilities for accessing the microworld are considered highly valuable. Following this spirit, this thesis intends to shed some light on some of these applications with the study of microprocessing of advanced materials through irradiation with ultrashort laser pulses.

The general objective of this thesis consisted in proposing and implementing feasible solutions to the challenges involved in the precise microprocessing of materials with ultrashort laser pulses for diverse advanced application. To that end,

attention was put in laser ablation of transparent polymers with the aim of achieving spatial resolutions that transcend sharpness limitations due to light diffraction, not forgetting the reduction of the heat affected zone thanks to the deterministic nature of nonlinear absorption mechanisms associated to the interaction of ultrashort laser pulses with transparent materials. At the same time, this task completely relies on the solution of the issue of precise focusing of a laser beam on the surface of transparent materials, another main goal pursued in this work. Additionally, some applications of the proposed focusing method to solve the demanding task of radiation focusing in superficial laser processing for functionalization of materials of interest form the final aim of the accomplished research. The fields of the investigated applications include diverse topics like biodegradation processes for biomedical appliances, pharmaceutical consumables quality control and microelectronics printing.

This thesis is constituted of a compilation of the most relevant results that have been obtained during the development of the doctorate studies in the frame of the PhD program in Nanosciences at the Departament de Física Aplicada of the Universitat de Barcelona. It is structured in four main chapters following the next organization scheme:

Introduction and objectives: This introductory chapter contains a description of the most significant microprocessing techniques, with special attention to laser based methods. Because of their key role in this thesis, the interaction between laser radiation and matter is shortly reviewed. The commented physical phenomena motivate the use of femtosecond lasers for the precise processing of transparent materials, where the focus is put on the superficial laser ablation of these materials, the challenges that entails and its applications. The objectives pursued in this work close this first chapter.

Experimental: A description of the experimental setups implementing femtosecond laser systems, methods and materials applied during the trials constituting the developed research is presented in this chapter. In the different sections that form this chapter, the features of the used laser sources together with the corresponding laser direct-write setups are described. Next, some remarks on Gaussian beams and their focusing are included. These lay the foundations for the presentation of the z-scan focusing technique. To close this chapter, a few comments and background

about the employed materials are delivered.

Z-scan focusing method: The results obtained by putting to work the z-scan focusing technique introduced in the previous chapter are presented here. The general topic is the development and characterization of the z-scan focusing technique as a method to address the issue of securing surface ablation of transparent material with femtosecond laser pulses. Its successful implementation in surface ablation of the transparent polymer polymethyl methacrylate (PMMA) with high spatial resolution is reported and given as an example of the possibilities of the proposed strategy for a precise focusing of laser beams onto transparent materials.

The contents of this chapter include studies on transmittance measurements at different focusing distances between the laser beam waist and the processed material surface through single laser pulse surface ablation and laser surface scanning for channel microprocessing, the beam waist position determination thanks to the transmittance measurements and analysis of the produced surface ablation, studies on reflectance measurements at different focusing distances, and the comparison between transmittance and reflectance results.

Applications in laser microprocessing of materials: the implementation of the developed z-scan focusing technique was put to use in laser microprocessing of materials with applications in diverse fields. Owing to the different studied applications, the chapter is divided in four sections, one for each topic. The various processed materials are briefly introduced, with some background supporting their study.

The investigated applications include the irradiation with femtosecond laser pulses of biodegradable polymers for profound hole ablation in polylactic acid (PLA) and study of its influence in biodegradability of polylactic-co-glycolic acid, the laser perforation for leakage studies on medical use polypropylene bags, and the laser fabrication of microfluidic guides for conductive line printing.

Conclusions: The last chapter sums up the most relevant results and main achievements that have been obtained during the development of this thesis in the form of closing remarks.

Resum

La manufacturació digital ha iniciat una autèntica revolució que està transformant els processos de fabricació industrial, començant per les primeres etapes de recerca i desenvolupament i arribant a tots els passos de producció, comercialització i màrqueting. Tot això gràcies a les possibilitats de les innovacions associades als processos digitals. Entre aquestes, destaquen l'adaptació i implementació de les demandes del mercat i la personalització cada cop més reclamada pels consumidors per tal que els bens produïts i els serveis proporcionats satisfacin les seves necessitats. El motiu d'aquesta revolució és que la producció digital ofereix l'opció extremadament convenient de realitzar canvis de disseny a través de la modificació de prototips virtuals mitjançant sistemes informatitzats. Aquesta possibilitat òbviament contrasta amb l'estratègia tradicional consistent en alterar un prototip físic fabricat prèviament, essent aquesta la més comuna de les estratègies aplicades als processos de fabricació anteriors a la implementació de tècniques digitals. El resultat d'aquests avenços tecnològics ens porta a processos de producció més ràpids, eficients i precisos, especialment necessaris ja que al mateix temps, les possibilitats que ofereix la manufacturació digital incrementen la complexitat dels processos relacionats amb la producció de béns i serveis, que cada vegada satisfan els seus propòsits més exitosament i convenient.

Un dels requisits de les noves tècniques digitals que científics i enginyers han d'abordar constantment és la miniaturització, que constitueix una estratègia bàsica en àrees tan destacades i diverses com l'electrònica, els camps relacionats amb estudis biomèdics com els productes farmacèutics i sensors químics i biològics i el desenvolupament de materials funcionals com a exemple. Els làsers són una eina versàtil que pot fer front a requisits com la flexibilitat, la velocitat i la compatibilitat amb el processament de grans extensions de materials amb una alta precisió. Des de la seva invenció per Theodore H. Mainman al 1960, els làsers s'han utilitzat en un imparable nombre creixent d'aplicacions. Per aquest motiu, es poden trobar en àrees tan diverses com la producció industrial, la medicina, les telecomunicacions i

les ciències naturals. Els principals avantatges de la llum làser provenen de la seva alta direccionalitat (col·limació) i la seva característica monocromacitat. La combinació d'aquestes propietats fan possible la generació d'intensitats extremes que poden ser enfocades a l'interior d'un volum minúscul, fet que fomenta la utilització dels làsers com a una eina ideal pel processament precís de qualsevol tipus de material a escala tant micromètrica com nanomètrica.

La microfabricació mitjançant l'ablació a través de la irradiació directa amb làser és la tècnica de microprocessament més clara ja que només consisteix en la irradiació d'un material enfocant-hi un feix làser. Amb les condicions adequades, la intensa energia del làser absorbida produeix una alteració d'una petita porció del material, deixant una àrea modificada al punt irradiat. En moltes ocasions, l'objectiu principal del microprocessament és aconseguir la màxima resolució espacial possible. En aquests sentit, la transferència de calor de l'energia làser absorbida cap al material és sovint un inconvenient per aquest objectiu. Aquesta situació es pot evitar mitjançant l'ús d'impulsos làser ultracurts. La seva duració extremadament curta entrega tota l'energia de l'impuls làser al material en un període de temps més curt que el temps de relaxació tèrmica de la xarxa cristal·lina. Aquest fet permet assolir una dràstica reducció de la dissipació tèrmica no desitjada més enllà de la regió irradiada. Per altra banda, diverses aplicacions requereixen la realització exclusiva de modificacions o ablació superficial del material. Això no esdevé cap problema quan el material processat és opac per la radiació del làser en la seva longitud d'ona, però en un material transparent constitueix un veritable repte degut a la necessitat de controlar de forma precisa la posició en la que l'energia del làser és enfocada per assegurar que l'absorció es realitza efectivament a la superfície del material processat, sense modificar-ne el seu interior. El desenvolupament d'estratègies que facin possible aquest control és crucial en aquestes circumstàncies.

Recentment l'ús de làsers d'impulsos ultracurts ha rebut atenció degut al reconeixement a Gérard Mourou i Donna Strickland amb el guardó del Premi Nobel de Física de l'any 2018 "pel seu mètode per generar impulsos òptics ultracurts d'alta intensitat". D'acord amb les motivacions per a l'entrega del premi, les innumerables àrees d'aplicació dels impulsos làser ultracurts encara no han estat explorades completament, però les seves possibilitats per accedir al món micromètric són considerades d'elevat interès. Seguint aquest esperit, aquesta tesi pretén aportar una

mica de llum amb l'estudi d'algunes d'aquestes aplicacions emmarcades en el microprocessament de materials avançats mitjançant la irradiació amb impulsos làser ultracurts.

L'objectiu general d'aquesta tesi doncs consisteix en proposar i implementar solucions viables als reptes relacionats amb microprocessament precís de materials amb impulsos làser ultracurts per a diverses aplicacions avançades. Amb aquest intenció, es va posar l'atenció en l'ablació amb làser de polímers transparents amb la idea d'obtenir resolucions espacials que transcendeixin les limitacions de definició associades a la difracció de la llum, en combinació amb la reducció de la zona tèrmicament afectada gràcies a la naturalesa determinista dels mecanismes d'absorció no lineals associats a les interaccions dels impulsos làser ultracurts amb materials transparents. Al mateix temps, aquesta tasca és totalment dependent de la solució al problema de l'enfocament precís d'un feix làser a la superfície d'un material transparent, considerat un altre objectiu d'aquest projecte. Addicionalment, algunes aplicacions d'aquest mètode per enfocar proposat per resoldre l'exigent tasca de l'enfocament de la radiació en el tractament làser superficial per la funcionalització de materials d'interès constitueixen l'aspiració final de la recerca realitzada. Els camps de les aplicacions investigades inclouen temes tan diversos com els processos de biodegradació per a productes biomèdics i farmacèutics amb els corresponents controls de qualitat i la impressió de components microelectrònics.

Aquesta tesi està constituïda per una compilació dels resultats més rellevants que s'han obtingut durant el desenvolupament dels estudis de doctorat en el marc del programa de doctorat en Nanociències del Departament de Física Aplicada de la Universitat de Barcelona. Aquest document està estructurat en quatre capítols principals que segueixen la següent organització:

Introducció i objectius: Aquest capítol introductori conté una descripció de les tècniques de microfabricació més significatives, parant especial atenció en els mètodes basats en l'ús de làsers. Pel seu paper clau en aquesta tesi, se'n fa una petita presentació sobre la interacció entre la radiació làser i la matèria. Els fenòmens físics comentats ens porten a fer servir els làsers d'impulsos ultracurts per al processament precís de materials transparents, on el focus es posa en l'ablació superficial amb làser d'aquests materials, els reptes que suposa i les seves aplicacions. Els objectius que es volen assolir en aquest treball clouen el primer capítol.

Experimental: Una descripció dels muntatges experimentals que empren sistemes de làser de duració ultracurta, dels mètodes i dels materials aplicats durant les proves que constitueixen el cos de la recerca es presenten en aquest capítol. En les diferents seccions que formen aquest capítol, les característiques de les fonts làser utilitzades juntament amb els muntatges d'irradiació directa amb làser hi són descrits. Posteriorment, s'inclouen unes observacions sobre feixos gaussians i com enfocar-los. Aquesta informació porta a la presentació de la tècnica d'enfocament per z-scan. Per tancar aquest capítol, s'aporten uns alguns comentaris i context sobre els materials que s'han emprat.

El mètode d'enfocament z-scan: Els resultats obtinguts mitjançant la utilització de la tècnica d'enfocament per z-scan introduïda en el capítol anterior es present aquí. El tema general is el desenvolupament i caracterització de la tècnica d'enfocament per z-scan com a mètode per adreçar el problema d'assegurar l'ablació superficial de materials transparents amb impulsosos làser de femtosegons. Es fa una ressenya de la implementació exitosa per ablació superficial del polímer transparent conegut com a metacrilat de polimetil (PMMA) amb una elevada resolució espacial i es dona com a exemple de les possibilitats de l'estratègia proposada per l'enfocament precís de feixos làser dins de materials transparents.

Els continguts d'aquest capítol inclouen estudis sobre mesuraments de la transmitància en diferents distancies d'enfocament entre la cintura del feix làser i la superfície del material processat a traves de l'ablació de la superfície amb un únic impuls làser i l'escaneig de la superfície mitjançant làser per la microfabricació de canals, la decisió de la posició de la cintura del feix làser gràcies als mesuraments de transmitància i l'anàlisi de l'ablació produïda a la superfície, estudis sobre mesuraments de reflectància en diferents distancies d'enfocament, i la comparació dels resultats entre transmitància i reflectància.

Aplicacions en el microprocessament de materials amb làser: La implementació de la tècnica desenvolupada d'enfocament per z-scan s'ha emprat en el microprocessament de materials per làser amb aplicacions en diversos camps. Degut a les diferents aplicacions estudiades, aquest capítol es troba dividit en quatre seccions, una per cada àmbit. Els diversos materials processats són breument introduïts, amb una lleugera contextualització que en motiva l'estudi.

Les aplicacions investigades inclouen la irradiació amb impulsos làser ultracurts de polímers biodegradables per a la fabricació de forats profunds en àcid polílàctic (PLA) i l'estudi de la seva influència en la biodegradabilitat de l'àcid polílàctic-co-glicòlic (PLGA), la perforació làser per estudis de fuites en bosses de polipropilè d'ús mèdic i la fabricació làser de guies de microfluídica per a la impressió de línies conductores.

Conclusions: L'últim capítol resumeix els resultats més rellevants i els principals assoliments que s'han obtingut durant el desenvolupament d'aquesta tesi.

1 Introduction and objectives

The first chapter of this doctoral thesis begins with a general outlook of the most relevant and used up-to-date strategies for material microprocessing. Among them, special attention is put into laser based techniques such as laser direct-write micromachining (the principal procedure studied in this thesis) and laser-induced forward transfer (LIFT). The chapter is divided in three sections. The first one contains an introduction to the most relevant techniques for the microscale processing of materials. The second one is focused on laser direct-write microprocessing, the physical processes involved, with a special detail in the modification of transparent materials using ultrashort laser pulses, and some of the best known of the multiple applications of femtosecond lasers as an advanced tool for material microprocessing. Finally, the last part includes the motivation for the fulfillment of the work together with the principal pursued objectives.

1.1. Microfabrication techniques

In the recent decades, device and consumables manufacturing is evolving towards the reduction in size and, as a direct result, resources and energy consumption required in the production processes of the multiple components with the principal goal of fabricating sustainable, efficient and compact products with improved functionalities. These qualities have a high demand and become crucial under circumstances where access to goods and resources is limited, like is the case for any activity taking place in outer space. Space exploration is gaining again interest owing to the development of space tourism and the multiple projects related to bringing the man to Mars and possible utilization of space resources. Another growing discipline that depends on the detailed qualities for device manufacturing is the so called Internet of things, which has huge potential to revolutionize the use and interaction with virtually all the goods and devices involved in everyday life thanks to their extended connectivity to the Internet.

A direct repercussion of these requirements is the mutation that manufacturing techniques are experimenting in order to adjust to the new demands on improved spatial resolutions that miniaturization entails. Representative cases of this situation appear in manifold fields of interest in scientific and industrial research like electronics [1], chemistry [2, 3], medicine [4] and biology [5] to name a few. All of them can be found in the multidisciplinary area of nanoscience and nanotechnology, which include all the research focused on the understanding and use of processes happening and affecting matter at the nanoscale dimension range.

Microfabrication techniques can be classified in two main groups according to the strategy implemented to obtain the miniaturized patters: mask-based and direct-write. The first group includes techniques that use a mask or a mold to reproduce the desired pattern in the processed material samples. Photolithography [6], micro-moulding [7], micro-contact printing [8, 9] and hot-embossing [10, 11] are the most relevant techniques employing this approach. All of them require a previously fabricated mask or master that is usually obtained by scanning beam lithography methods [12].

Hard molding for nanoimprint lithography, usually referred as hot embossing when the processed material is heated before imprinting [11], is a precise fabrication method for 3D structuring of a substrate employing a prefabricated mold to imprint a desired pattern through pressure application. As a contact process, it entails a series of challenges that must be overcome for its successful usage. In order to avoid direct contact of the processed substrate with the imprinting mold and to ensure a uniform distribution of the applied pressure, a release layer can be introduced in-between. It can also be used as a solution for controlling possible defects occurring during the release of the mold.

A common use of nanoimprint lithography is the patterning of a polymer glass substrate above its crystal transition temperature T_g (see Figure 1.1). After the pressure application, the polymer hardens when cooled down and the mold is removed, leaving the patterned release layer. This layer can be used as the final nanostructured substrate or as an etch-resistant layer for a subsequent etching step for translation of the imprinted pattern to the polymer substrate below.

This microprocessing technique has shown the possibility of producing patterns
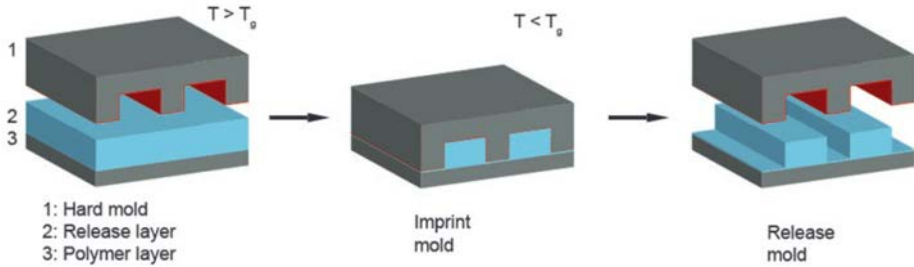
Figure 1.1: Schematic diagram of the processing steps involved in the hot embossing micro-processing technique, also known as hard molding for nanoimprint lithography. Reproduced with permission from [13].

with extremely small dimensions down to 10 nm [14] with limited requirements of the needed experimental setup. Other advantages are the ability of processing large areas due to the possibility of using large patterned molds [15], and high throughput by use of roll-to-roll processes. In contrast, its use limited to polymeric materials, the necessity of prefabricated templates for imprinting obtained by complex scanning beam lithographic techniques requiring specialized instrumentation and processes, and the obligation of producing new molds every time that changes in the design of the imprinted patterns must be adjusted imply that these technique is limited to some applications, excluding fast prototyping and flexible adaption.

Oppositely, direct write techniques do not demand the previous fabrication of any mask since the sample patterning takes places directly. This approach needs fewer fabrication steps and hence constitutes a simpler and faster option when the high throughput of identically processed samples achievable by mask based methods is not strictly required [16, 17]. Besides, direct write techniques become specially of interest when the manufacturing processes require a fast transition from the design phase to the final manufactured product, what makes them particularly suitable for rapid prototyping. This group of techniques includes ink-jet printing [18], laser induced forward transfer (LIFT) [19], laser micromachining [20], and more elaborated strategies such as two photon polymerization [21] and Focused Ion Beam (FIB) [22].

Among them, ink-jet printing is the most widespread direct-write technique. It consists in the deposition of liquid droplets onto a substrate by liquid ejection

through a nozzle. The generation of the droplets has its origin in the creation of high pressure pulses in the liquid, which leads to the formation of a jet. Its disruption produces the ejection of a droplet that can be deposited with control on a receptor substrate. There are two general mechanisms for the generation of the droplets: continuous ink-jet printing (CIJ) and drop-on-demand (DOD) ink-jet printing. Both approaches are represented in Figure 1.2. Typical droplet diameters obtained with these techniques can reach 50 to 70 μm. Moreover, they give the possibility of printing complex functional materials with high spatial resolution, with line width values down to 14 to 25 μm [23].
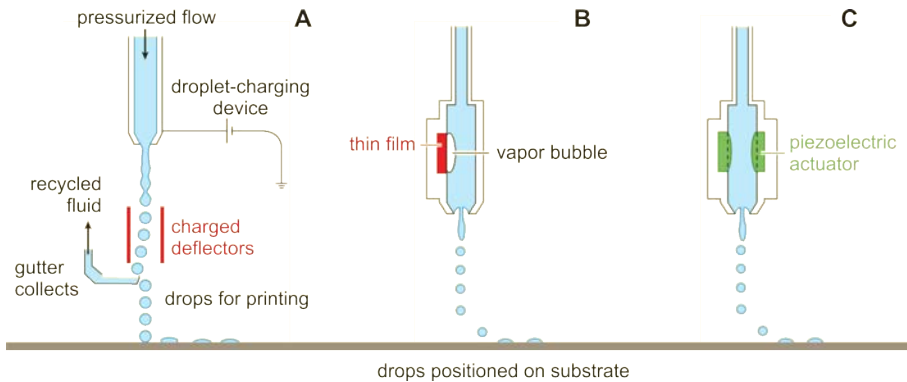
Figure 1.2: Sketch depicting the principles of operation of ink-jet printing according to different mechanisms: (A) Continuous ink-jet printing (CIJ) and Drop-on-demand (DOD) ink-jet printing generated by (B) a thermally generated pulse or (C) a piezoelectric actuator. Figure adapted from [18] © IOP Publishing. Reproduced with permission. All rights reserved.

In spite of the widespread use of ink-jet printing as an additive microprocessing technique owing to its simplicity and achievable high spatial resolutions of the printed patterns, important drawbacks might come across according to the compatibility of the printed liquids with this technique. The parameter window for printable liquid viscosities is found in the range between 1 and 50 mPa·s [24]. For this reason, working with liquids showing viscosity values outside this range requires an additional adjustment of the ink properties or the modification of the printing head [24, 25]. Furthermore, nozzle clogging issues can also become seriously detrimental in the case of complex rheology liquid printing, when the inks rapidly dry and block the head output, or in situations where the size of the par-

ticles suspended in the ink is only an order of magnitude smaller than the nozzle diameter or larger [26].

Most of these issues can be solved by changing the employed microprocessing technique in these complex cases to another additive method using lasers to assist the material transfer from a donor to the desired acceptor substrate where the transferred material can be printed in the wanted pattern. This technique is known as the Laser Induced Forward Transfer (LIFT) technique. Its principle of operation is based on the transfer of material from a donor substrate coated with the material to be transferred onto a receiving substrate, usually referred as acceptor or receptor, as shown in Figure 1.3. Laser radiation is sent to the material coating passing through the transparent donor substrate. When the radiation reaches the material coating, its energy is absorbed at the coating, producing the ejection of a part of the coating that is transferred onto a receptor substrate conveniently placed close to the donor substrate. According to the laser radiation focusing conditions and the experimental parameters related to laser radiation, the amount of transferred material that is ejected from the donor can be controlled. This control gives the dimensions of the transferred pixels. Finally, successive pixel deposition results in the fabrication of the desired pattern on top of the receptor substrate.

In the case of LIFT of materials in the solid phase, 3D structures can be produced by successive stacking of the pixels (or voxels, the usual name given to the single transferred units in 3D manufacturing), as shown in multiples examples detailed in [27]. In addition, the LIFT of solid films has proved successful in the printing of metals [28–31], semiconductors [32] and dielectrics [33–35] by putting into use laser pulses of different durations and a wide range of available laser wavelengths in the optical spectrum, from ultraviolet to infrared. However, in spite of the appealing versatility of the LIFT solid material printing, some disadvantages can be encountered during the implementation of this technique. These are mainly alterations in the quality of the transferred materials and the additional need of processes for the preparation of the material thin films coating the donor substrate. With respect to that, the transfer process initiated through laser radiation absorption can induce phase transitions of the transferred material, seriously modifying the original properties of the solid material. This drawback becomes a serious issue for the deposition of many complex materials with sensible properties. An alternative to overcome this impediment is the LIFT of materials in a liquid film coating
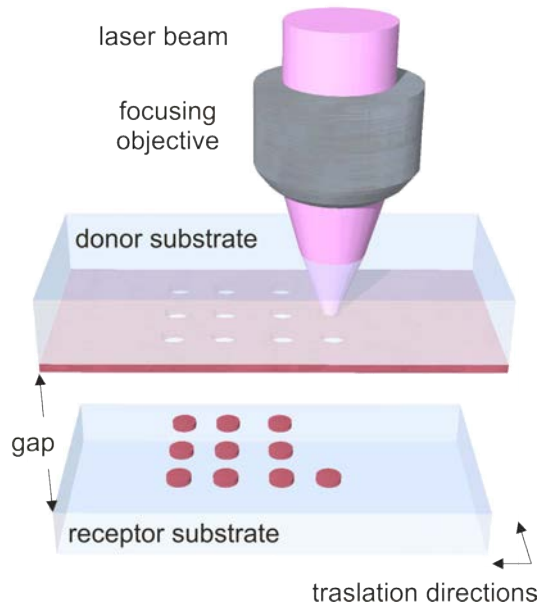
Figure 1.3: Schematic diagram of the principle of operation of the LIFT technique.

the donor substrate.

In this strategy, the layer coating the donor substrate is an ink film constituted by the material of interest in either a suspension or as a solution. The material transfer takes place in the following way: the laser energy is absorbed by the film coating the donor, and under adequate conditions this absorption produces the ejection of a liquid jet that can reach the receptor substrate and deposit a certain amount of the liquid film onto it. The result is the formation of a droplet on the receptor substrate. Successive droplet deposition produces the desired pattern onto the receptor substrate. As a final step, the drying of the liquid content of the printed droplets consolidates the adhesion of the transferred material onto the receptor substrate.

LIFT of liquids requires that laser radiation is directly absorbed by the liquid donor film. This is not the case for liquid or solid materials that are transparent to the used laser radiation. In this situation, an intermediate sacrificial layer that absorbs the incident laser radiation can be added to the donor substrate to induce the ejection of the material [36–42]. In addition, the use of this additional layer

provides a more gentle transfer of the material of interest, since laser radiation is exclusively absorbed at the sacrificial layer, whose role is exclusively the ejection of the material, and only the small fraction of the liquid donor film in contact with the radiation absorption point might suffer some reduced damage. Thanks to this, different materials could be printed with LIFT using liquids without detrimental modifications of their functional properties. As an example, various studies have reported the successful transfer of biological molecules [43–47], materials for tissue engineering [48, 49], and the transfer of thermally, mechanically and electrically sensitive materials [40, 50–53].

The possibility to organize the printed droplets (pixels after drying) into a functional structure becomes of high interest for the fabrication of electronic components and interconnects in microelectronic devices [54–56]. With this purpose, most of the fabrication methods are based on the printing of overlapping droplets at different separation distances using conductive materials in form of nanoparticle suspensions, with the aim of creating 2D patterns [57–60]. Nevertheless, achieving high finishing quality in the printing of continuous lines constitutes a remarkable technical challenge due to multiple effects. Defects such as splashing and scalloping can notably decrease the quality of the printed lines. Additionally, instabilities originated during the printing of lines usually lead to the appearance of bulges, which compromise not only the line appearance, but also the functionality of the printed features [60–63].

Ion beam lithography, also named Focused Ion Beam (FIB) technique, is a scanning beam lithography fabrication process using heavy ions (usually Ga^+ ions around 30 keV) to ablate material from the processed surface or to alter the chemical properties of the processed surface (see Figure 1.4). Owing to the interest of this part in direct-write techniques, the first option will be commented.

When the focused ions impinge onto the processed substrate, their collision produces the milling of the substrate or its sputtering. Ion implantation is also another possibility depending on the used material. Features with sizes of 10 nm have been obtained with a beam having a spot size of 8 nm on a thin film of PMMA [64]. For a further increased spatial resolution, a resist layer can be used for a more precise action of the already small focused ion beams through filtering of the ion beam edges, leaving only the central peak intensity. After processing, the resist layer
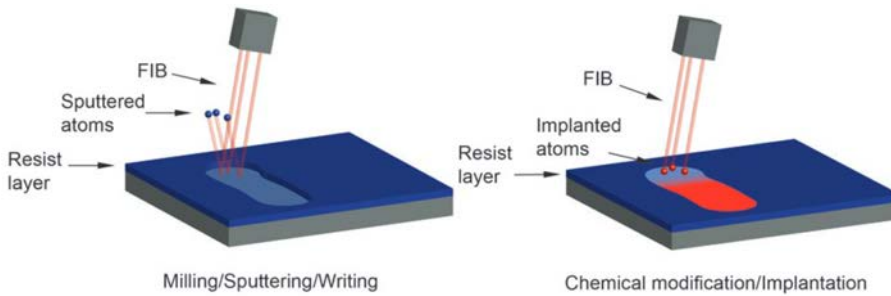
Figure 1.4: Schematic diagram of the principles of operation of ion beam lithography, a scanning beam lithography microprocessing technique also known as focused ion beam technique. Reproduced with permission from [13]).

must be etched.

The high spatial resolutions of the produced features by ion beam lithography are the main advantage of this technique for selective ablation of virtually any kind of material. However, its precision entails very slow processing speeds that commonly restrict its use to specific applications requiring extremely precise processing along very small regions. In addition, the necessity vacuum conditions further extends the duration of the fabrication process.

To conclude this section dedicated to microprocessing techniques, the principal approach employed in this thesis will be introduced. Laser microprocessing is another direct-write technique that does not require the use of any masks since the desired patterns are produced directly through scanning of a laser beam along the processed material. The precise energy deposition possible with focused ultrashort laser pulses makes possible the accurate processing of materials through this method. Furthermore, the intrinsic characteristics of laser light makes possible the modification of any kind of material, providing an unbeatable versatility for this technique. Owing to the main importance of this technique in the work presented in this thesis, the next section will contain relevant information about laser microprocessing, including physical processes responsible for the interaction between laser light and matter, the laser energy absorption mechanisms, and the results and challenges that this technique entails.

1.2. Laser microprocessing

The invention of lasers lead to a myriad of variegated applications that extend from everyday consumer goods and services like telecommunications (optical fiber), music players and printers to more specialized uses in industrial processing of materials, precise measurements, and medical and biological applications to name a few [65]. Some of these applications are based on the precise modification achievable in a large variety of materials through interaction with laser light, owing to the high intensities that lasers can originate through the attainable focusing of their almost monochromatic and directional radiation in unprecedented small volumes. This modification can be achieved with a simple operation principle: irradiation of the material to be processed by sufficiently energetic laser light induces that a tiny portion of material in the irradiated area is either modified or directly vaporized.

1.2.1. Interaction between laser radiation and matter

Laser radiation absorption by materials can happen through linear and non-linear mechanisms, depending on the material, the laser wavelength and intensity. In the case of materials that are not transparent to light of the same wavelength as the laser, laser radiation absorption commonly takes place through linear processes. Under these circumstances, electrons in the material directly absorb the laser energy according to the material absorption at the light wavelength of the laser. Absorption of the photons that constitute the laser radiation by electrons produces the promotion of electrons from a lower energy band to a higher energy band (interband absorption), or from a low energy state to a higher energy one energy inside the same energy band (intraband absorption). For the case of metals, radiation of almost any wavelength value in the visible range can be absorbed promoting intraband electronic transitions. In the case of semiconductor materials, absorption can only succeed when the incident laser radiation photons posses enough energy to overcome the energy band gap and produce the excitation of electrons from the valence band to the conduction band. Dielectric materials show a similar behavior for radiation absorption, but with larger energy band gaps. For this reason, the only laser wavelengths that can be effectively absorbed by wide band gap dielectrics following linear electronic transitions are ultraviolet lasers. Photons in these wavelengths have sufficient energy to overcome the band gap. As an alternative, CO_2 lasers, which have wavelengths around 10 μm in the far infrared, can be

employed. However, in this case absorption proceeds through radiation coupling
to phonons instead of electron promotion [66].

A suitable option to induce absorption in transparent dielectric materials is the
use of focused ultra short laser pulses, in view of their capacity to enable non-
linear absorption mechanisms like multiphoton absorption and quantum tunnelling
together with avalanche ionization. Multiphoton absorption consists in the promo-
tion of an electron in a single and simultaneous absorption event of more than one
photon so that the total absorbed energy (sum of the simultaneously absorbed sin-
gle photon energies) results higher than the energy band gap. In an unlike manner,
quantum tunnelling happens when the incident electric field of the radiation alters
the Coulomb potential well so that electrons jump to the conduction band through
tunnelling across the potential barrier (Figure 1.5). These fundamental absorption
mechanisms just account for the generation of the seed electrons necessary for the
beginning of optical breakdown, which will eventually occur through the gener-
ated free-carrier absorption followed by avalanche ionization.
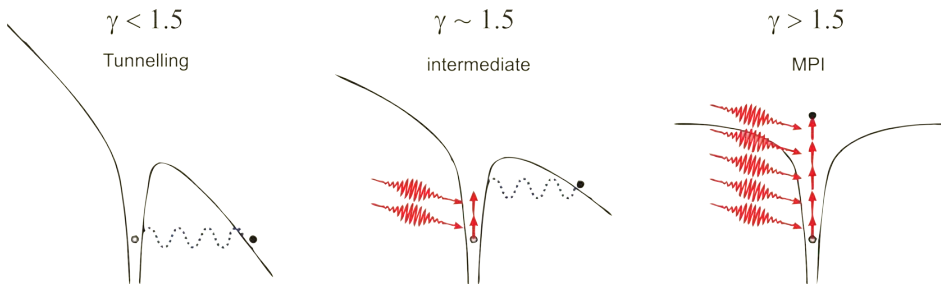
Figure 1.5: Schematic diagram of photoionization according to different values of the
Keldysh parameter. Image taken from [67] © IOP Publishing. Reproduced with permis-
sion. All rights reserved.

For the identification of the predominant fundamental absorption process, the
transition point between multiphoton ionization and tunneling ionization is indi-
cated by the Keldysh parameter γ, defined in the following way:

$$\gamma = \frac{\omega}{e} \sqrt{\frac{m_e c n \epsilon_0 E_g}{I}}, \tag{1.1}$$

where ω is the laser light frequency, I is the laser intensity at the focus, m_e is

the effective electron mass, e is the fundamental electron charge, c is the speed of light, n is the refractive index of the irradiated material, ϵ_0 is the permittivity of free space, and E_g is the energy of the material band gap. If $\gamma < 1.5$ the predominant absorption mechanism is quantum tunnelling, while if $\gamma > 1.5$ multiphoton absorption dominates. For $\gamma \sim 1.5$, electrons are promoted to the conduction band through a combination of both processes, as it can be observed in Figure 1.5 [67].

After the initial nonlinear radiation absorption and consequent material ionization, and once that enough seed electrons have been promoted into the conduction band, optical breakdown follows through absorption of the remaining photons in the laser radiation by the newly generated free electrons in the conduction band (free-carrier absorption), ensued by avalanche ionization (Figure 1.6). During this process, seed electrons absorb the energy of incident photons, progressing at the same time to higher energy states inside the conduction band. The excess energy of these electrons is then transferred to other electrons still in the valence band, which are impact-ionized to the conduction band, resulting in an even higher population of electrons in the conduction band. The process repeats itself as long as the electromagnetic field of the incident laser radiation is present, leading to the commented avalanche effect.
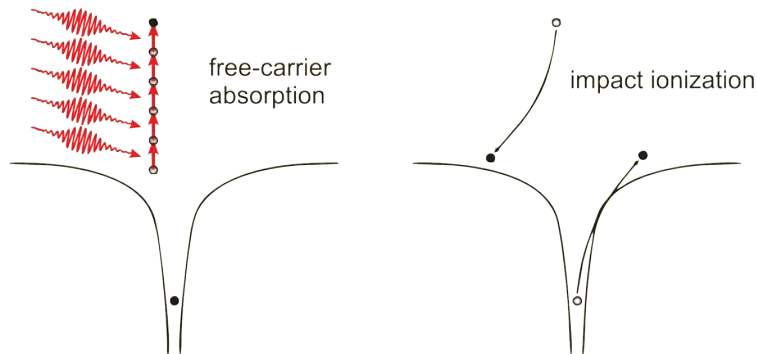
Figure 1.6: Schematic diagram of processes leading to avalanche ionization. Image taken from [67] © IOP Publishing. Reproduced with permission. All rights reserved.

1.2.2. Laser radiation absorption in transparent materials

Laser radiation absorption mechanisms described above can cause permanent damage in transparent materials with visible and near-infrared photons thanks to ultrashort laser pulses. In this situation, the absorbed intensity per unit length (dI/dz) depends non-linearly on the optical intensity (I) of the incident laser radiation. Different numbers of photons (n) must be simultaneously absorbed by multiphoton absorption at different wavelengths to successfully excite the electrons in the irradiated material (Figure 1.7).
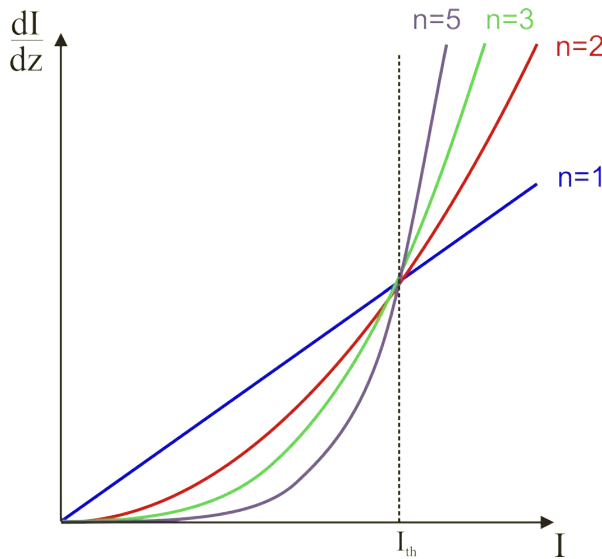
Figure 1.7: Schematic plot of the absorption per length unit (dI/dz) according to the incident intensity (I) for different number of simultaneously absorbed photons n. The dotted line refers to the behavior in a hypothetical process with $n \to \infty$ that would show a defined intensity threshold I_{th} for absorption [68]. Reprinted by permission from Springer Nature.

When only one photon ($n = 1$) is enough to overcome the material band gap, laser energy is linearly absorbed by the material and hence a well defined radiation absorption threshold can not be determined, although it is possible to determine a damage threshold. In non-linear absorption, however, the absorbed intensity per unit length has an exponential relationship with intensity ($dI/dz = \sigma_n I^n$), where the exponent n corresponds to the number of photons required to overcome the material band gap and induce absorption through promotion of electrons from the

valence band to the conduction band, thus satisfying $n\hbar\omega \geq E_g$. As it can be observed in Figure 1.7, this behavior of non-linear processes shows absorption lower than the linear case at low intensities, while at higher intensities the absorption is considerably higher and significantly increases with the number of simultaneously absorbed photons n. When the number of photons $n \to \infty$, the curves tend to a situation where a well threshold for absorption (I_{th}) can be defined. This behavior produces a sharp confinement of the absorption and the modifications produced during radiation absorption in material processing by ultrashort laser pulses. In comparison, these effects extend to larger regions of the processed materials when radiation absorption takes place through linear processes, as it is sketchily depicted in Figure 1.8.
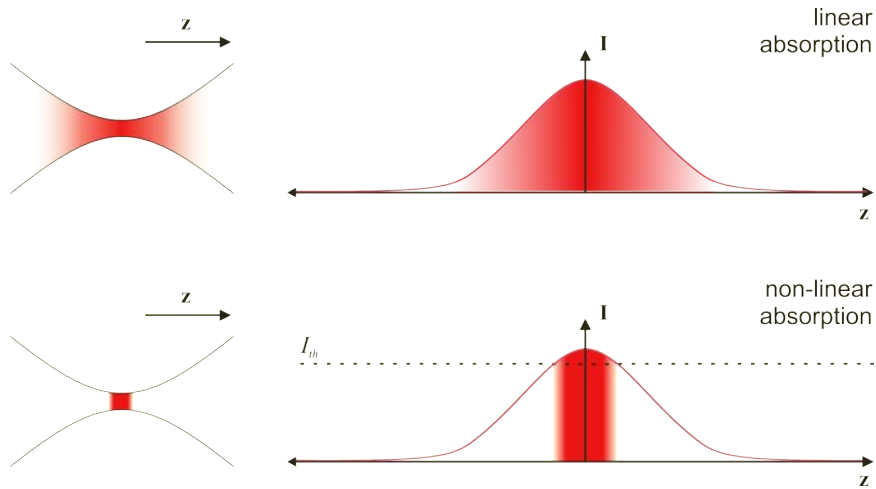
Figure 1.8: Absorption and damage confinement along the incident intensity profile of a focused laser beam due to the presence of an intensity threshold for non-linear absorption in comparison with complete absorption along the profile in linear absorption. Image adapted from [68]. Reprinted by permission from Springer Nature.

Another observed phenomenon when intense ultrashort laser pulses propagate inside transparent materials is self-focusing. Owing to the nonlinear nature of the transparent materials under these conditions of intense radiation, the material local refractive index n depends on the laser intensity I following the relation $n = n_0 + n_2 I$, where n_0 is the linear refractive index and n_2 is the second order nonlinear refractive index. According to this, intensity variations in the laser pulse

spatial distribution lead to a spatial refractive index gradient. Since n_2 takes positives in most materials, the fundamental transverse gaussian mode that describes the output of most lasers beams gives a higher refractive index at the center of the beam compared to the outskirts. Consequently, the refractive index gradient acts as a lens and focuses the beam. As the intensity in the laser pulse is increased, self-focusing becomes stronger until, at some critical intensity, a filament is formed.

At the same time and as the laser beam self-focuses, the peak intensity increases which, in turn, causes more self-focusing to occur. Eventually, the beam is prevented from self-focusing indefinitely by the commented nonlinear absorption mechanisms like multiphoton ionization, which come to play an important role when the laser intensity becomes very high. When this happens, the material is ionized by the high local optical field and an electron plasma is produced. This lowers the refractive index thanks to the negative refractive index contribution of the electron gas, defocusing the propagating light beam and cancelling the positive refractive index change produced by the intensity dependent index. Accordingly, either further self-focusing is prevented or propagation proceeds in a series of repeated focusing and defocusing steps [69].

With respect to the nonlinear absorption of intense laser radiation reached in ultrashort laser pulses, as soon as a material is irradiated with a high enough intensity pulse, the generated electron density in the conduction band dramatically increases. This further generates absorption through avalanche ionization involving free-carrier absorption followed by impact ionization, leading to the creation of an electron plasma in that band. If more energy is absorbed, the electronic plasma reaches a critical density where the material absorbs very efficiently the rest of the laser radiation through free carrier absorption. The result of this process is a very hot electron plasma that evolves in a time much shorter than usual recombination times for most materials through cooling by phonon emission, diffusion out of the irradiated volume or recombination with the corresponding ions [70, 71]. Only when the laser pulse radiation is over, the energy absorbed by the electron plasma can be transferred to the material lattice. This shock-like energy transfer to the material on a time scale much faster than thermal diffusion times is the responsible for permanent damage in the material, leading to ablation of material on its surface or permanent structural change in the bulk. The heat affected zone, ultimately responsible for the definition and resolution of the areas processed by laser,

is therefore drastically reduced when using ultrashort laser pulses. These features put forward ultrashort laser pulses as an ideal tool for the processing of transparent materials with exceptionally high spatial resolutions and definition (Figure 1.9).
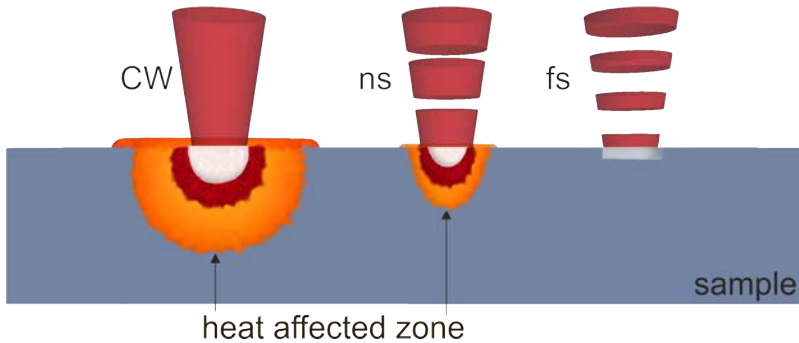
Figure 1.9: Sketch of laser ablation at the surface of a material through continuous wave radiation (CW), nanosecond and femtosecond pulsed laser irradiation.

1.2.3. Laser microprocessing of transparent materials and its applications

Owing to the advantages offered by ultrashort laser pulses thanks to the promoted nonlinear radiation absorption mechanisms, they can be used for processing transparent materials with high spatial resolution. Furthermore, the extremely reduced thermal dissipation and energy deposition in small volumes make them an ideal tool for the processing of sensitive materials such as polymers [72, 73] and biological samples [74], without compromising the stability and functionality of the material outside the irradiated zone.

One of the most widespread applications of ultrashort laser processing of transparent materials consists in the confined alteration of the refractive index in the material bulk. This process takes place when ultrashort laser pulses are tightly focused, reaching high intensities that promote non-linear energy absorption only in the focal volume, increasing the local temperature and producing the rapid melting and re-solidification of the irradiated material. In this way, an optical waveguide can be fabricated when the laser beam is scanned along the material. As a consequence, this technique offers the possibility of creating any desired 3D structure in

the bulk with manifold uses [75] like the production of optical waveguides [76], data storage devices [77, 78], and integrated microfluidic channels when the material in the irradiated zone is completely vaporized and the debris removed by wet chemical etching [79] or by water flowing into the created microchannel in 3D drilling from the rear surface of glass in contact with water [80–82]. Another possible microprocessing approach in this field consists in the precise laser irradiation of a photostructurable glass-ceramic followed by thermal processing and chemical etching [83–86]. In addition, bulk processing of transparent materials with ultrashort laser pulses can benefit from the possibility of tailoring the laser beam energy distribution. This feature makes possible the modification of the cross-sectional shape of the produced patterns [87], a useful peculiarity that is difficult to achieve with common microprocessing techniques like lithography.

In contraposition to bulk processing, other applications require the functionalization of the surface of transparent samples. The most established applications in this field are surface microfluidic channels for lab-on-a-chip devices [88, 89], miniaturized biological sensors [90], bioimplants and tissue engineering [91, 92] and microlenses [93].

Surface ablation of transparent materials, which is reported in these applications, needs a high control on the position where the laser energy is focused and hence absorbed by the material. Slight variations of the laser beam focus position close to the surface can lead to absorption in the bulk or no absorption at all. For this reason, this challenging requirement demands the development and implementation of strategies for controlling the focusing of the laser beam to guarantee the surface ablation of transparent materials with high spatial resolution. Studied approaches include diverse strategies. Trial and error experiments are based on the visualization of the produced superficial ablation, identifying the thinnest fabricated feature as the position corresponding to the laser beam focus laying at the material surface [94]. This strategy, despite being straightforward, relies on the ability of the researcher for detecting the smallest produced feature, what results inaccurate for precise surface ablation. In addition, the visualization system depth of focus, illumination and resolution are other factors that make this technique unsuitable for achieving a superficial processing with high spatial resolution and repeatability.

Another proposed approach uses active [95] or passive [96] confocal positioning for keeping the laser beam focus at the processed sample surface. Good accuracy on the focusing and precise superficial processing of the samples is secured by this technique. However, either its complex and costly experimental implementation and/or the time consuming involved processes for keeping track at any moment of the focus position might be detrimental for fast manufacturing at high laser scanning processing speeds or for prototyping and trials, since the complexity of the experimental setup might hinder the possibilities of research on new materials requiring different experimental processes. Moreover, active confocal positioning can be implemented merely along one direction in the XY plane (perpendicular to the laser beam propagation direction). On the other hand, passive confocal positioning needs a trial and error process to find the position of the surface on the target sample, with the consequent time consumption associated to this strategy. To that end, devising strategies for the precise and errorless positioning of the laser beam waist with regard to the processed sample surface to secure surface ablation persists as a real hurdle in the microstructuring of transparent materials with ultrashort pulsed lasers.

1.3.   Motivation of the work and objectives

The experimental work carried out during this thesis was based on the research lines being investigated by the research group where the thesis has been developed through the awarded research projects and collaboration projects with industrial companies. In accordance to them, the general objective consisting in proposing and implementing feasible solutions to the challenges involved in the precise microprocessing of materials with ultrashort laser pulses was set out.

More specifically, the following main objectives were proposed:

- Design and assembly of an automatized and fast laser direct-write experimental equipment including a femtosecond laser for microprocessing of different kinds of materials.

- Exploration of a focusing technique for securing laser ablation of transparent materials and solving the issue of tightly focusing laser pulses at the surface of transparent materials and not inside the bulk or outside the material.

- Study of the precise surface ablation of transparent polymers using femtosecond laser pulses with the aim of achieving spatial resolutions that surpass limitations due to light diffraction thanks to the deterministic nature of nonlinear absorption mechanisms.

- Extension of the obtained results for the laser beam focus position control to applications of interest employing femtosecond laser pulses for precise processing of materials with varied functionalities, so that the proposed focusing strategies help in achieving their microstructuring.

2 Experimental

The contents of this chapter include a general description of the experimental set-ups, methods and materials implemented during the development of the experimental research that constitutes this thesis work. The chapter is divided into five sections. The first one presents the characteristics of the used laser sources. The second section consists of a description of the laser direct-write setups. The third section covers some considerations about issues related with Gaussian beams. The fourth section describes the z-scan process. Finally, some relevant comments on the materials processed by laser in this thesis are introduced in the last section.

2.1. Laser sources

2.1.1. Amplitude Systemes femtosecond laser

The mainly used laser source was fabricated by the company Amplitude Systemes. This model in particular has the name s-Pulse. Its active medium was a crystal of potassium, yttrium and tungsten doped with ytterbium, Yb:KYW. The output nominal laser wavelength was 1027 nm and the nominal pulse duration was 450 fs. This laser can work at repetition rates up to 10 kHz. A scheme of this system is presented in Figure 2.1.

The pulsed output beam is generated along four different steps: first, a low intensity femtosecond pulse is generated in a mode-locked laser oscillator, producing pulses with energies between 10 and 20 nJ (L1). Then, this pulse is stretched in (L2) to be subsequently amplified in (L3). Finally, the beam is compressed in (L4) leading to the high energy femtosecond laser pulse with an output energy up to 100 μJ. Directly after the laser output window, the measured beam intensity distribution corresponds to a Gaussian beam with a nominal quality factor M^2 of 1.4[1],

---

[1]Described later in this section.
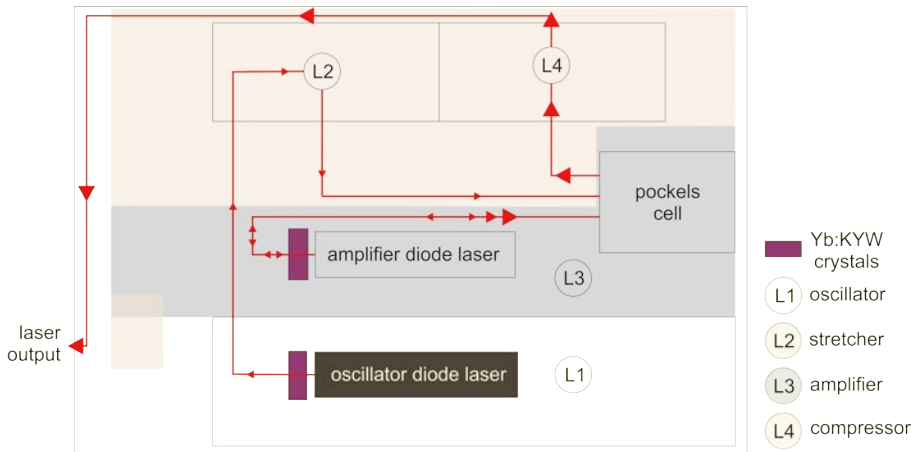
Figure 2.1: Scheme showing the different elements inside the Amplitude Systemes femtosecond laser.

and 5 mm diameter measured at $1/e^2$ of the Gaussian peak value, as it can be observed in the intensity profile shown in Figure 2.2.
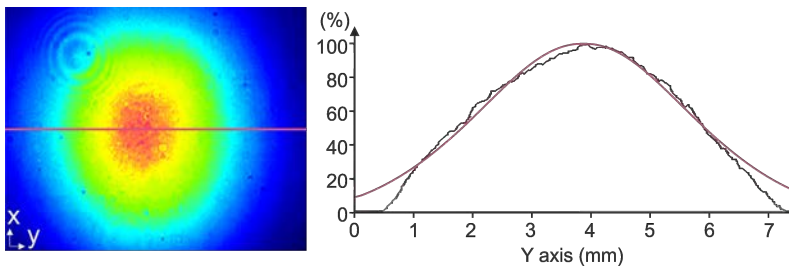
Figure 2.2: Beam intensity distribution at the output of the Amplitude femtosecond laser. The profile corresponds to a cross-section of the beam intensity along the Y axis at the position indicated by the line on the image.

2.1.2. Coherent femtosecond laser

Another femtosecond laser source was used for the experiments carried out during the research stay at Keio University. The manufacturer of this laser was the company Coherent and the model was named Libra. The active medium was a crystal of Ti:Sapphire with output laser wavelength of 800 nm and nominal pulse duration

of 80 fs. The laser was operated in an external trigger mode, which provided the desired number of pulses at a maximum repetition rate of 10 kHz.

The generation process of the femtosecond laser pulses is very similar to the previously described for the Amplitude femtosecond laser. However, in this case the laser pulses were available in two additional different wavelengths apart from the fundamental 800 nm thanks to the presence of second and third harmonic generation crystals. These crystals could be accessed by the fundamental wavelength laser beam after removing a conveniently placed mirror that directed the incident beam to the laser output window. After the removal of this mirror, the laser beam was directed to the first second harmonic generation crystal, which doubled the frequency of the incident radiation and therefore reduced the wavelength of the laser beam to 400 nm. This generated beam was then directed to a secondary output window, what made easier the alignment of the setup corresponding to the optical path for the 400 nm laser beam.

The case of the third available value for the laser wavelength showed a slightly higher experimental complexity. By adjusting some optical elements for the fundamental beam and also after the first second harmonic generation, this beam with 400 nm wavelength was mixed with the rest of the fundamental 800 nm beam that is not used for second harmonic generation onto another second harmonic generation crystal. The result of this process is a laser beam at 266 nm wavelength by means of sum frequency generation of both waves. This beam is then directed to the same secondary output window as for the 400 nm beam. Therefore, both 400 nm and 266 nm laser beams shared the same optical path. This meant that all optical elements guiding the beam should be substituted and realigned each time that the laser wavelength had to be changed.

For this laser, the measured beam intensity distribution after the laser output window corresponded to a Gaussian beam with a nominal quality factor M^2 of 1.3, and 6 mm diameter at $1/e^2$ of the Gaussian peak value. The femtosecond pulse output energy reached a value up to 4 mJ at the fundamental wavelength of 800 nm.

2.2.   **Laser direct-write setups**

All the following elements were almost completely installed during the progress of the experiments presented in this thesis. The setups were optimized and integrated to allow the control of the different translation stages through computers via Lab-View programs, which were developed and refined throughout the experiments.

The experimental setups described in the following two sections were mounted on an optical bench (Melles Griot, 250 cm long, 125 cm wide) that comprised a triple-plate construction, with internal dampers and four air-suspended legs that formed the support system. It provided a steady, rigid and almost vibration-free working surface. The upper plate of the table was equipped with M6 mounting holes to enable a rapid and tight fixation of the different elements. Some additional information on the rest of experimental aspects such as sample preparation and specific experimental parameters can be found in the published papers.

2.2.1.   **Z-scan setup**

The microfabrication experiments on PMMA and PLA were all performed using the setup composed of the elements illustrated in Figure 2.3. The Amplitude femtosecond laser beam (see subsection 2.1.1) passed through a set of two polarizers (P1 and P2), which ensured a fixed polarization direction of the pulses, and a half-wave plate ($\lambda/2$) that allowed adjusting the laser pulse energy. Then, a first beam splitter Bs1 (60T/40R) divided the laser beam in two paths: the transmitted beam allowed the measurement of the laser energy with an energy detector[2] (D1), and the reflected beam was directed towards a mirror (M) that reflected infrared radiation (1027 nm) and transmitted visible light to have in situ visualization of the ongoing process by a CCD camera (JAI Protec 07013400) placed coaxially to the laser beam. A microscope objective (Mitutoyo M Plan Apo 50× and 0.55 NA for PMMA experiments, Thorlabs LMH-5×-1064 and 0.13 NA for PLA tests) focused the radiation onto the samples. The transmitted radiation through the samples was collected at an energy detector (D3) placed directly after the sample. In some experiments, the energy reflected by the sample was measured by a second energy detector (D2, PD10-PJ-C from Ophir Optronics) that captured the reflected

---

[2]Depending on the energy range, various energy detectors were implemented: PD10-SH from 1 nJ to 10 μJ, PD10-V2 from 2 nJ to 20 μJ and PE10-C from 1 μJ up to 10 mJ, all from Ophir Optronics.

radiation from a second beam splitter Bs2 (90T/10R) collected with a lens (L). Reflectance and transmittance measurements were performed simultaneously with a multi-channel laser power/energy meter (Pulsar 4, from Ophir Optronics).
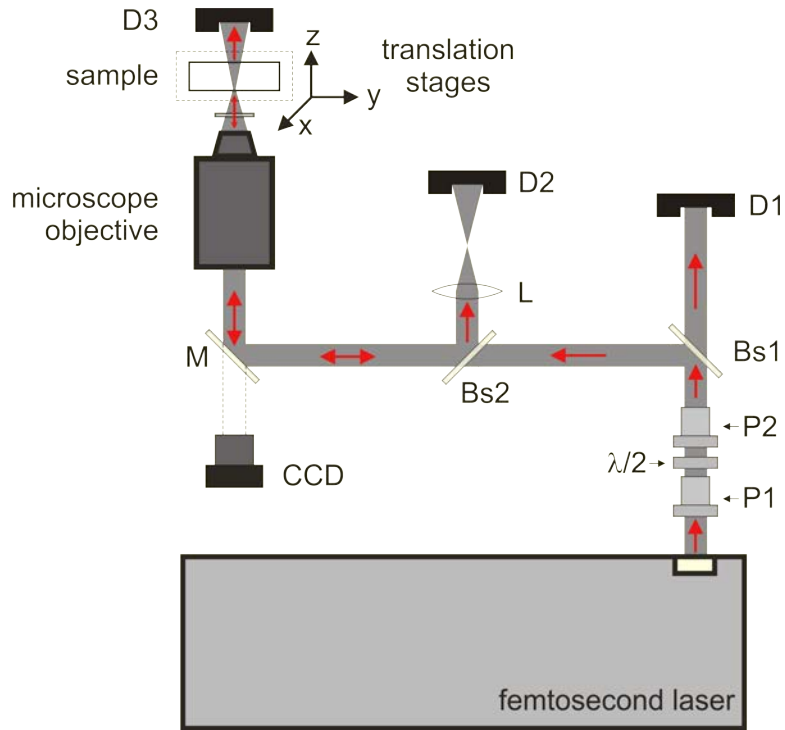
Figure 2.3: Sketch of the laser ablation system. P: polarizers. $\lambda/2$: half-wave plate. Bs: beam splitters. M: mirror. D: energy detectors. Red arrows show the light propagation direction at each section of the laser beam optical path.

Motorized XYZ translation stages supplied by A.COLOMA Microscopios y Aparatos Ópticos, and controlled by a computer (controller Prior Scientific Systems, Pro ScanTM III) allowed the translation of the sample with respect to the laser beam. The travel range of the XY step motors was 100 mm with minimum incremental steps of 0.01 μm, and for the Z step motor the range was 40 mm with minimum incremental steps of 0.1 μm. The maximum translation speed was 1 mm/s in the XY axis and 2.5 mm/s in the Z axis. Besides, the translation stage was outfitted with a sample holder that allowed the modification of the tilting level of the sample with respect to the laser beam axis by means of two integrated micro-screws, one

for each sample plane direction.

2.2.2. Hybrid setup

The experiments carried out on the rest of materials described on the corresponding section below were all performed using the setup formed by the elements illustrated in Figure 2.4. It was named hybrid setup since it was used to perform experiments on laser ablation, and just by properly placing a donor-receptor system, it was used as a LIFT printing system as well.
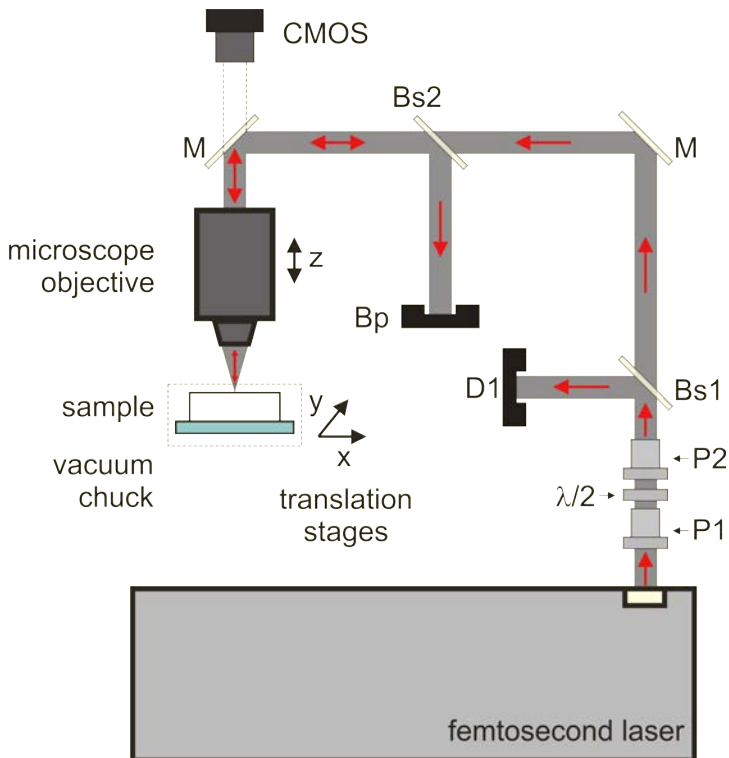
Figure 2.4: Sketch of the LIFT hybrid printing system. P: polarizers. $\lambda/2$: half-wave plate. Bs: beam splitters. M: mirrors. D: energy detectors. Bp: beam profiler. Red arrows show the light propagation direction at each section of the laser beam optical path.

In this setup, the output laser radiation from the Amplitude laser (see subsection 2.1.1) passed through a set of two polarizers (P1 and P2) and a half-wave plate ($\lambda/2$). Then, a first beam splitter (Bs1, 60T/40R) divided the laser beam in

two paths: the reflected beam allowed the measurement of the laser energy by an energy detector (D1), and the transmitted beam was directed through mirrors (M) towards another mirror that reflected infrared light (1027 nm) and transmitted visible light to have an in situ visualization of the ongoing process by a CMOS camera (Thorlabs DCC1645C) placed coaxially to the laser beam. Specifications of the different microscope objectives used to focus the laser pulses onto the samples are presented in Table 2.1. In some experiments, the beam reflected by the sample was visualized and analyzed at a beam profiler (Bp, BEAMSTAR-V-PCI from Ophir Optronics) that captured the reflected radiation from a second beam splitter Bs2 (90T/10R).

Table 2.1: Specifications of the microscope objectives used in the different experiments carried out in the hybrid setup shown in Figure 2.4, where M is the Magnification and NA is the Numerical Aperture.

Item	M	NA	Processed materials
Mitutoyo M Plan Apo	50×	0.55	Conductive silver nanoparticle inks
Thorlabs LMH-20×-1064	20×	0.40	Polypropylene bags
Thorlabs LMH-10×-1064	10×	0.25	Polypropylene bags
Thorlabs LMH-5×-1064	5×	0.13	Polypropylene bags

In this setup, computer-controlled XYZ translation stages from Physik Instrumente incorporated three stages propelled by DC motors (M-414 High-Load Precision Stage) that allowed the translation of the sample in the XY plane. In order to change the focusing of the energy, the position of the microscope objective was controlled independently from the XY stages by means of a Z axis stage. The travel range of all the stages was 100 mm with minimum incremental steps of 0.5 μm and a maximum translation speed of 100 mm/s. In order to ensure the steadiness of the sample, a vacuum chuck coupled to a low vacuum system was placed on the XY translation stages.

2.2.3. Three-wavelength microfabrication setup

As commented during the Coherent femtosecond laser description (see subsection 2.1.2), this setup shown in Figure 2.5 could be used in two different configurations: one for a laser beam at 800 nm and another one for the laser beams at 400 nm

and 266 nm. The 800 nm beam exited the laser through the main output window and was directed by two mirrors to an iris diaphragm, which allowed an easier alignment of the system. The 400 nm and 266 nm beams exited the laser through the secondary output window and followed an optical path that was parallel to the 800 nm beam. Two mirrors directed the beam to another iris diaphragm, which satisfied the same objective as mentioned before.
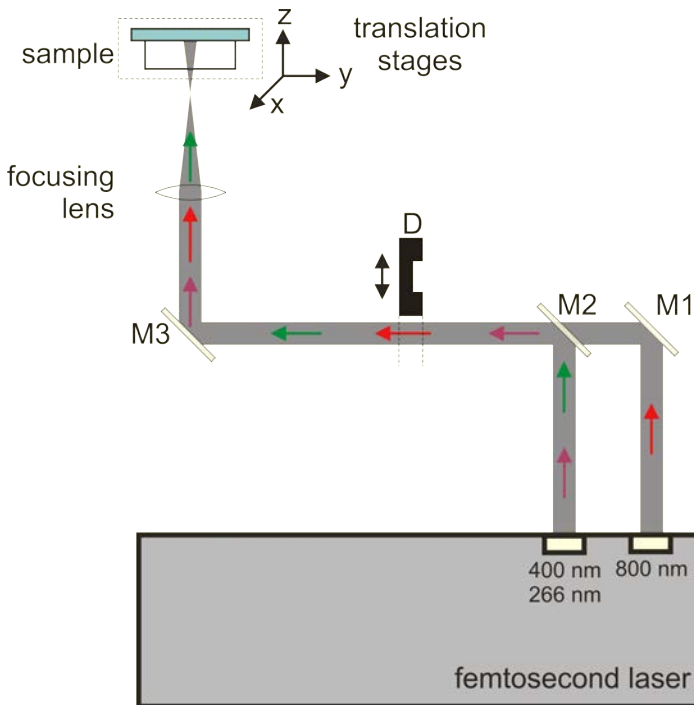
Figure 2.5: Simplified sketch of the three-wavelength laser microfabrication setup. M: mirrors. M1 was kept fixed. M2 was added when the 400 nm and 266 nm laser beams were used. M3 was realigned for each wavelength used. D: movable power detector. Colored arrows show the light propagation direction at each section of the different wavelength laser beam optical paths.

After these diaphragms, the beams were directed by two mirrors into a plano-convex lens (200 mm focal length), which was used to focus the beam onto the sample at normal incidence. The position of these two last mirrors had to be carefully adjusted every time that the setup configuration was changed in order to ensure that the beam properly entered the focusing lens. Once the beam was

focused by the focal lens, the sample surface was placed after the beam waist at a certain distance in order to obtain a laser spot on the surface with a diameter around 100 µm and at the same time to avoid focusing inside the material bulk through self-focusing effects. These would have led to detrimental modifications and filamentation inside the material that were outside the scope of the planned biodegradation studies on the surface of biodegradable polymers.

In this setup, PLGA polymer samples were attached to a remote-controlled XY translation stage that allowed micrometric displacements. Since there was no need for a constant change of the sample surface position in the Z axis (laser beam direction) in these trials, this position was adjusted previous to the experiments by means of a micrometric screw. The use of a CCD camera beam profiler at the same calculated position for the sample surface permitted adjusting the distance between the focal lens and the translation stages in order to obtain the desired beam spot size onto the sample surface.

2.3. Gaussian beam theory

One of the principal laser beam magnitudes that determines the light-material interaction in materials laser processing is the pulse energy per unit area, known as fluence. The fluence distribution for a Gaussian beam that is propagating in the z direction in cylindrical coordinates is the following:

$$F(r, z) = \frac{2E}{\pi \omega^2(z)} \exp\left(-2\frac{r^2}{\omega^2(z)}\right). \tag{2.1}$$

where $F(r, z)$ is the laser fluence, E is the pulse energy, $\omega(z)$ is the laser beam radius at a given z position and r is the radial coordinate. The peak fluence F_p is given by

$$F_p = \frac{2E}{\pi \omega^2(z)}. \tag{2.2}$$

Since the beam preserves the Gaussian distribution after passing through the various optical elements, when the laser beam ablates a material with an ablation threshold fluence F_{th}, the radius r_0 of the ablation crater can be determined from

equation 2.1 (Figure 2.6):
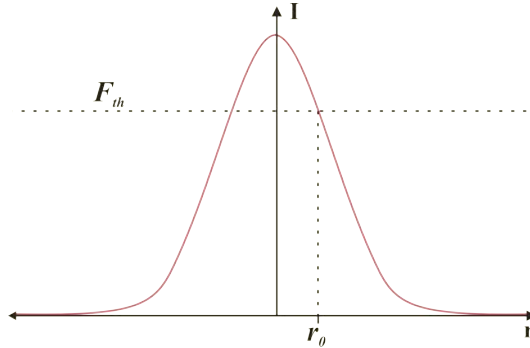
Figure 2.6: When a material is irradiated with a laser pulse intensity that overcomes a threshold fluence F_{th}, it will ideally produce a crater on the material with radius r_0.

$$r_0^2 = \frac{\omega^2(z)}{2} \ln \left(\frac{F_p}{F_{th}} \right).$$ (2.3)

Through this expression, the beam radius $\omega(z)$ and threshold fluence F_{th} of the irradiated material can be found from measurements of the spots produced on the surface of the sample at the corresponding incident pulse energies. As an example, Figure 2.7 shows the result of an ablation experiment performed on polymethyl methacrylate. During the experiments done in the z-scan setup (see subsection 2.2.1) and at the surface of PMMA samples, the sample was irradiated with different incident energies at different positions on the XY plane but at the same z position, producing craters whose radii were measured.

For a fundamental transverse gaussian mode TEM_{00} beam, the radius of the beam changes along the propagation direction according to

$$\omega(z) = \omega_0 \left[1 + \left(\frac{\lambda z}{\pi \omega_0^2} \right)^2 \right]^{1/2},$$ (2.4)

where λ is the laser wavelength and z is the distance that the beam has propagated from the beam waist position. At the beam waist, the beam has its most narrow
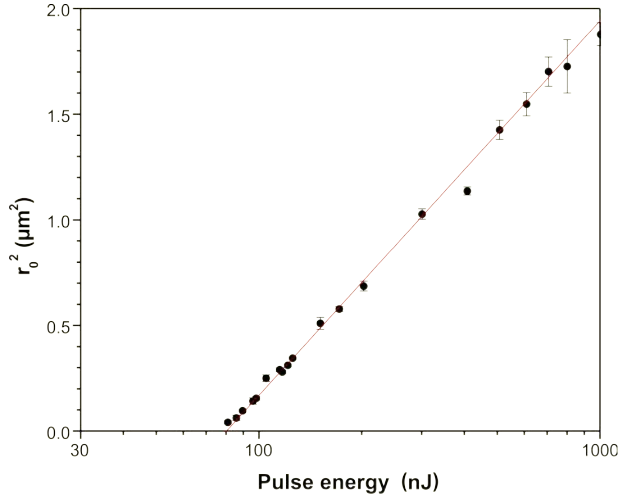
Figure 2.7: Plot of the craters radius squared vs the pulse energy. The intercept of the fitted line with the x axis corresponds to the energy threshold for ablation.

point and the wavefront is flat. At this location, the laser beam has its smallest radius: ω_0.
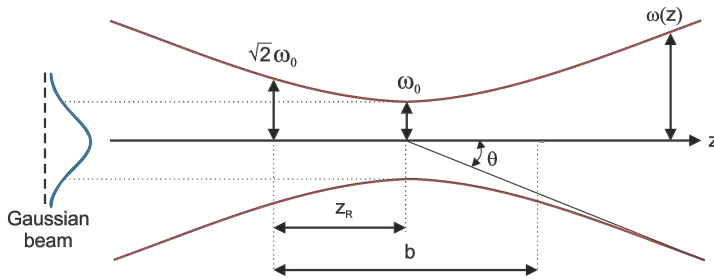
Figure 2.8: Gaussian beam parameters associated with angular divergence [97].

The axial range along which the beam can be considered to be collimated is known as the confocal parameter b (Figure 2.8), and corresponds to two times the Rayleigh length z_R (equation 2.5). It is also referred to as the depth of focus when focusing a Gaussian beam.

$$z_R = \frac{\pi \omega_0^2}{\lambda} \tag{2.5}$$

For distances much longer than the Rayleigh length, the radius increases linearly with the propagation distance z:

$$\omega(z) \cong \frac{\lambda z}{\pi \omega_0},$$ (2.6)

and from here, the divergence of a Gaussian beam is given by

$$\theta = \frac{\lambda}{\pi \omega_0}.$$ (2.7)

Most real beams, however, do not correspond exactly to a perfect Gaussian beam; therefore, an additional parameter which describes how similar the real beam is to the ideal one is introduced. It is known as the quality factor M^2, which is a positive number greater than or equal to 1 [97]. The values for the the real divergence Θ_r and the real laser beam waist W_{0r} are then modified by a factor M^2 as follows:

$$\Theta_r W_{0r} = \frac{M^2 \lambda}{\pi}.$$ (2.8)

2.4.   The z-scan focusing process

The focused laser beam profile evolution as a function of z presented in the previous section about Gaussian beams clearly evidences that the interaction between the focused femtosecond laser pulses and an irradiated transparent material strongly depends on the position of the laser beam waist with respect to the material. In order to study this dependency, the z-scan method becomes a useful tool to obtain valuable information about this interaction for the material region close to its surface. This information can be used as well for developing a procedure to correctly focus the laser beam onto transparent materials.

This method consists in simultaneously measuring the incident and the transmitted or reflected energy at different distance values (focusing distances or z positions) between the sample surface and the laser beam waist. The objective is to measure the amount of transmitted or reflected energy with respect to the incident energy at each z position and then identify which is the most adequate position to work on the surface of the material. In the experiments described in this chapter, the laser beam was focused by the Mitutoyo M Plan Apo 50× magnification and

0.55 NA microscope objective. These tight focusing conditions with a small size of the beam waist together with the laser incident energies available lead to peak intensities higher than 1 TW/cm^2, where non-linear absorption processes were expected [67].

The first step to perform a z-scan is to place the material well outside from the laser beam waist. For the studied PMMA samples and the objective used, a distance around 30 μm from the laser beam waist position was enough. This step is possible thanks to the images from the CCD camera. At this point, the laser focus is far enough of the material sample and, if the material is transparent to the laser wavelength, there should not be energy absorption. Every time that a laser pulse is fired, the positioning system moves the sample in the z axis direction by decreasing the distance between the material surface and the laser beam waist. At the same time, the sample is moved in the xy plane in order to fire the next laser pulse with a horizontal separation to avoid pulse cumulative effects. Both incident and transmitted or reflected energies are recorded for every pulse and, after data analysis, the values for transmittance or reflectance and absorbance are obtained. Since the used energies are well below the critical energy to produce the self-focusing effect in air (a few mJ), non-linear effects are negligible before the beam enters inside the samples [96, 98].

The transmittance curve variation in each z position along 30 μm starting from a certain point close to the to the surface is shown in Figure 2.9. In this plot, it is possible to identify 3 stages. The first stage corresponds to a region where the transmittance value presents its maximum (91 %) since the surface of the sample is getting closer to the laser focus but the energy intensity is not high enough to be absorbed. As the sample gets closer to the beam waist (up in Figure 2.9(a)), a decrease in the transmittance values is registered because the fluence at the surface increases until a point where it is high enough to promote energy absorption. During the second stage, the transmittance decreases in each step (middle in Figure 2.9(a)) as the sample approaches the beam waist, where the intensity reaches its maximum so that the energy absorption increases significantly. At a certain point, the transmittance reaches its minimum and energy absorption becomes maximal (down in Figure 2.9(a)). Beyond this point, the transmittance in all the subsequent positions keeps at a constant value around 58 %, indicating that the sample surface overpassed the beam waist position and the focus is already inside the ma-
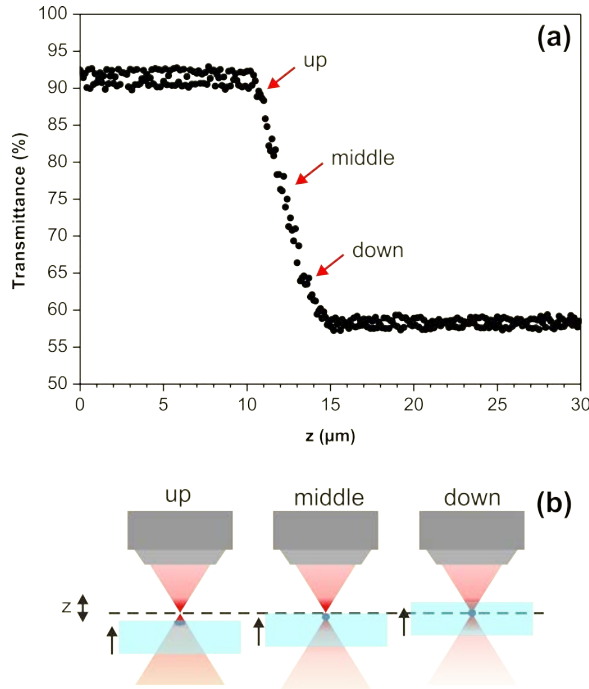
Figure 2.9: (a) Typical transmittance curve obtained at 200 nJ incident energy on a PMMA sample. Three positions are chosen to characterize the z-scan: up, middle and down, where laser ablation experiments at different energies were performed. (b) Scheme of the focusing conditions in the three selected positions for the laser beam waist close to the sample surface.

terial. The transmittance drop only occurs in a range of positions in the proximity of the laser beam waist, as it was verified in the results exposed in the subsection 3.1.2 of the chapter 3.

It has to be pointed out that the z-scan should be performed when the material sample is placed perpendicular to the beam axis, so the xy motion of the sample does not imply an unwanted modification of the surface position with respect to the beam waist. For this reason, a procedure called 'scan' is used in order to achieve that perpendicularity before each z-scan experiment. Scans are made in the xy plane along a total distance of 2 mm in steps of 5 μm. It is essentially a scan of the sample in the xy direction without variations in the z position.

Three scans made at an incident energy value of 200 nJ are shown in Figure
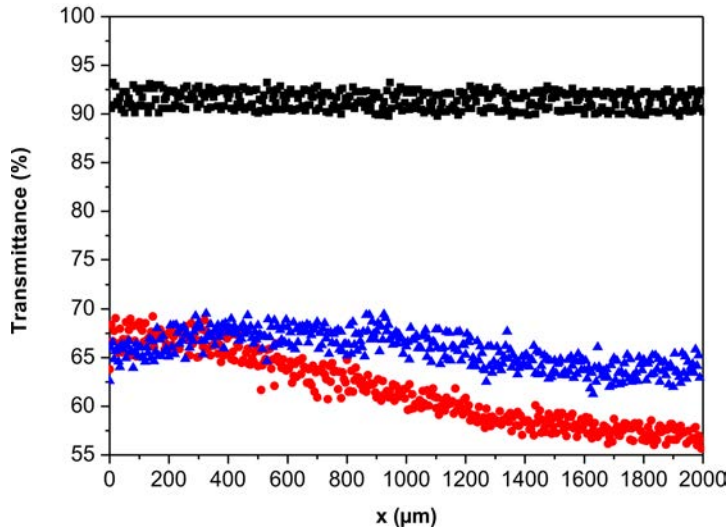
Figure 2.10: Scans on PMMA with the laser focus at different positions on a length of 2000 μm along the x axis, (**squares**) out of the sample, (**dots**) within a tilted sample, and (**triangles**) within a sample after tilt correction.

2.10. The first one (squares) was made with the sample in a position where the beam waist is completely outside the material. Consequently, the transmittance curve shows a horizontal trend at its maximum value because there is no energy absorption. This gives an estimation of the uncertainty in the transmittance measurements. In the second scan (circles), the sample was placed in a position where the transmittance value initially corresponds to the point middle on Figure 2.9(a). At this position, the performed scan reveals a variation in the transmittance along the horizontal direction, indicating that the sample was tilted. Then, the sample holder tilt was adjusted by using two micrometric screws each for x and y axis until the performed scan follows a trend with a ±5 % variation in the transmittance along the scan similar to the third one presented in Figure 2.10 (triangles). At this point, it is assumed that the tilt of the sample is adequate to perform the experiments.

2.5.   **Laser-processed materials**

The results of the experiments presented in this work have been performed on different material substrates, what shows the versatility of lasers as a processing and manufacturing tool. Some relevant data about these materials and the methods implemented to process and study them is given in this section.

2.5.1.   **Polymethyl methacrylate (PMMA)**

This transparent thermoplastic polymer is frequently used as a substitute of glass. It has good biocompatibility and is being used as material for implants or for dynamic drug release applications [99]. Owing to its high transparency in the visible and infrared spectra (see Figure 2.11), good chemical stability and ease of manufacture, PMMA can also be found as substrate material for microfluidics and lab-on-a-chip devices [72]. Microchannels and optical waveguides can be fabricated by femtosecond lasers with wavelengths in the near infrared, not only onto its surface but also inside the bulk of PMMA [76, 100–102]. Femtosecond lasers can also modify the hydrophobicity of the PMMA surface [103, 104] or enhance its ability for binding proteins on it [105].

Other remarkable properties of PMMA are a tensile strength similar to aluminum, resistance against chemical attack of several compounds, and permeability of oxygen and carbon dioxide. It is often preferred in comparison to other similar polymers because of its moderate properties, easy handling and processing, and low cost.

The used PMMA sheets were acquired to the company Goodfellow and they were carefully prepared in rectangular pieces of 20 mm × 10 mm and thickness of 1.1 mm.

Since the Mitutoyo M Plan Apo 50× objective was used in all the experiments performed on PMMA, the employed method to correctly place the sample surface at the laser beam focus was the z-scan technique. Hence scans and z-scan were executed before all the surface modification and ablation experiments on these polymer samples.
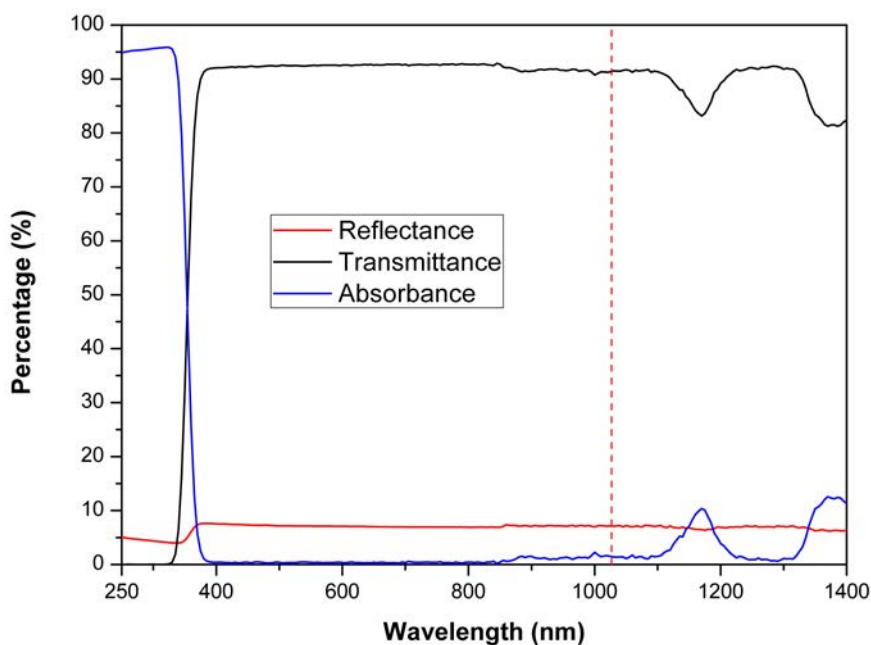
Figure 2.11: Reflectance, transmittance and absorbance of PMMA as a function of the incident light wavelength. A dashed line at 1027 nm helps to find the values for the laser wavelength used in the experiments. At this point, the PMMA sample transmits 91 % of the incident light energy.

2.5.2. Polylactic acid (PLA) and poly(lactic-co-glycolic acid) (PLGA)

PLA is a biodegradable and bioactive rigid thermoplastic polymer with an amorphous or partially crystalline structure that is obtained from renewable resources like corn starch or sugarcane. Its mechanical properties and degradation behavior can be tuned by using different combinations of copolymers and monomers during its synthesis. PLGA is a biocompatible and biodegradable copolymer that biodegrades by random hydrolysis of ester bonds to form lactic and glycolic acids, both present in the human body as by-products of various metabolical pathways. When comparing PLA and PLGA biodegradation properties, previous studies showed that PLA presents a slower degradation rate due to the higher crystallinity and hydrophobicity of PLA [106–108].

These transparent (see Figure 2.12) biodegradable polymers are being widely

investigated in experiments and processes related to biomedical studies like drug delivery [109] and tissue scaffolding [110]. Furthermore, clinical trials have been carried out in applications such as bioabsorbable sutures [111, 112] and bone fixation devices [113, 114].
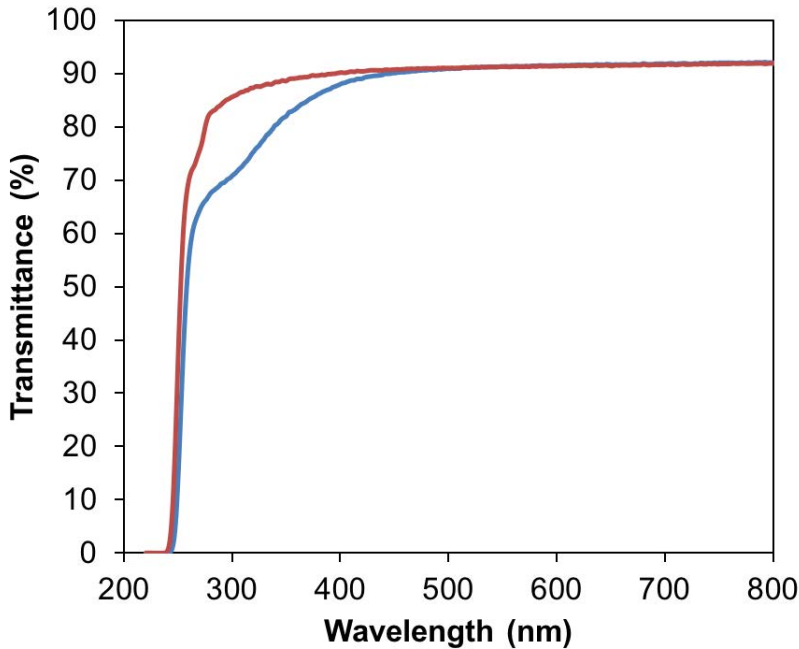
Figure 2.12: PLA (red line) and PLGA (blue line) transmittance spectra measured by spectrophotometry. Experiments on PLGA were done at 800, 400 and 266 nm laser wavelength.

During the experiments on PLA samples, the laser beam was focused on the sample surface by the Thorlabs LMH-5×-1064 0.13 NA objective. Because of this low numerical aperture value, there was no need for a precise focusing technique. In this case, visualization of sample surface defects through the setup camera was enough to focus the laser beam.

For the three-wavelength microfabrication experimental setup where PLGA samples were processed, the desired beam spot size of 100 μm diameter at the sample surface was achieved through imaging of the laser beam by a beam profiler CCD camera, as previously commented in the corresponding laser direct-write setups subsection 2.2.3.

Biodegradation studies on PLGA were carried out by evaluation of the morphological changes of the produced holes and determination of the evolution of their diameters. After laser irradiation, PLGA samples were fully immersed in a 5 mL phosphate-buffered saline (PBS) solution with pH of 7.4 in a vial and kept at 37°C in an incubation oven. Samples were observed with a microscope (MS-100 from Asahikogaku) after an immersion time of 3, 6, 8, 24, 48, 72 and 168 hours.

2.5.3. Polypropylene bags for medical uses

Multilayer film coextruded polypropylene bags have multiple applications as medical consumables. These products must undergo manifold tests and have to follow strict standards and regulations from international organisms compiled in manuals like the European Pharmacopeia. According to quality standards regulations gathered in compendia like the United States Pharmacopeia (USP) and the National Formulary (NF), together in a combination known as USP-NF, 'Microperforations produced by laser irradiation reproduce quite realistically perforations of these coatings that can happen under usual manipulation conditions, therefore the use of lasers for such studies is advised'.

Experiments carried out on polypropylene bags had the purpose of producing holes through the bag surface with controlled dimensions for calibrating leak detection systems. In this case, the laser beam was focused onto the sample through the Thorlabs LMH-20×-1064 microscope objective. Like in the experiments on the metallized sealing coatings, the laser beam was precisely focused onto the bag surface through observation at the beam profiler of the laser light reflected by the surface.

For an optimal hole perforation of the bag surface, it was observed after many tests that the best procedure was displacing the objective along the z direction in order to change the laser beam focus with respect to the fixed sample position while drilling the surface, but starting with the focus at z positions inside the bag and moving it to outer positions in order to promote a better material removal.

In order to avoid any kind of ablation or modification of the sealing coatings or the polypropylene bags during the focusing process and before the microperfora-

tion experiments, the beam light used was not the usual amplified femtosecond laser pulses but the continuous laser light produced at the laser oscillator, without any amplification.

2.5.4. Conductive silver nanoparticles ink for inkjet printing

A commercially available silver nanoparticle ink from Sigma Aldrich® was used in the LIFT experiments presented in section 4.3. Particle size was smaller than 50 nm and the ink solid content was around 30-35 %. Donor films were prepared by blade coating thin layers of ink with a thickness between 20 to 30 μm on glass microscope slides. This relatively large film thickness was optimal for improving the uniformity of the donor film because its fast drying.

The gap between the donor and acceptor substrates (160 μm) was kept constant by using cover slips as spacers. Although it is common that LIFT experiments use a sacrificial absorbing layer, in the presented experiments this was not needed because the silver ink itself directly absorbed the laser radiation at the laser wavelength. The laser beam was focused into the ink film through the Mitutoyo M Plan Apo 50× microscope objective. The correct focusing of the laser beam was checked through observation at the beam profiler of the laser light reflected by the interface between the glass slide holder and the ink donor film.

Printed lines obtained by LIFT transfer of overlapping droplets were dried and laser cured by means of a continuous wave (CW) Nd:YAG laser (Baasel LBI 6000, 1064 nm wavelength, 1.2 W output power and Gaussian intensity profile) operating at a scan speed of 2 mm/s with an irradiance of about 12 kW/cm^2. At the end of the process, the conductivity of the lines was measured and compared with the nominal value for the ink given by the manufacturer.

3 Z-scan focusing method

This chapter compiles all the obtained results corresponding to the development and characterization of the z-scan focusing method together with the results obtained through its implementation in surface ablation and modification of PMMA samples.

The production of small patterns with high resolution at the surface of transparent materials by laser ablation requires the use of high numerical aperture optical systems for tightly focusing laser pulses into microscopic volumes where extreme energy densities are reached. This is a challenging task since slight changes in the position where laser energy is tightly focused can result in totally different outcomes: surface ablation, modification in the bulk material or even no modification of the material at all. For this reason, in the presented results, special attention is put into studying the z-scan focusing technique for its implementation in surface micromachining of transparent samples with spatial resolutions that can overcome the diffraction limit. For all the experiments, samples of polymethyl methacrylate (PMMA) were used. This polymer has high transparency in the visible range and high chemical stability, what makes it a biocompatible material for the fabrication of lab-on-a-chip devices and many biological sensors. In all the experiments shown in this chapter, the laser beam was focused onto the sample through the Mitutoyo M Plan Apo $50\times$ and 0.55 NA microscope objective.

3.1.   Studies on transmittance measurements at different focusing distances

The z-scan method was originally devised as a technique for the measurement of the non-linear refraction index of transparent materials. In this technique, changes in the transmitted energy are detected by placing both an aperture and an energy

detector after the sample [115]. The approach taken in the experiments presented in this chapter has been described beforehand in the corresponding section of the chapter 2, and it follows essentially the same principle as the z-scan technique, but with slightly higher energies and without any aperture between the sample and the energy detector.

Following the description given in chapter 1 about the interaction mechanisms leading to energy absorption of ultrashort laser pulses in transparent materials, some details concerning absorption will be given for a better understanding of the role that it plays in the observed transmittance measurements. Lazare et al. [116] proposed a model to predict the evolution of the absorption for a silk protein during femtosecond laser pulse irradiation through evaluation of the ionization probabilities considering multiphoton ionization, electron impact ionization, and the density of ionizable electrons of the material. Results showed that only a fraction of the energy is absorbed at the material in the first 10 nm from the surface, so great part of the laser pulse energy continues propagating inside. The amount of absorbed energy increases with increasing laser fluence. Taking into account the values corresponding to the peak intensities used in the next explained experiments and the band gap of 3.7 eV for the PMMA samples (calculated from an UV-visible transmittance spectrum), the Keldysh parameter [117] takes values ranging from 1 for the highest energy pulses to 2 for the lowest ones. Thus, the first ionization mechanism occurring in these experiments was probably produced by multiphoton absorption, although some contribution from tunneling ionization cannot be completely disregarded. However, once the critical density for impact ionization is reached, most of the ionized electrons are generated by this mechanism and results should not be highly dependent on the first ionization mechanism probabilities.

3.1.1.   Single laser shot surface ablation

As it has been already commented in section 2.4, z-scans could be adequately performed once the sample surface plane was perpendicular to the laser beam propagation direction (z axis). Z-scans consisted in firing laser pulses over the sample at different focusing distances, producing crater shaped modifications on the surface when the laser beam waist is located close to the surface. For single shot surface ablation, only one laser pulse was fired at each position on the sample

surface. At the same time, the incident pulse energy and the transmitted energy through the sample were measured. Three different positions were identified in the transmittance curve in Figure 2.9: up, middle and down, corresponding to transmittances of 90±2 %, 75±2 % and 65±2 %, respectively for an incident energy of 200 nJ. Afterwards, the sample was located in these three positions by sending pulses at this incident energy value and displacing the sample in the z axis until the transmittance reached the corresponding value for each position. Then, laser pulses were fired at different incident energies from 30 nJ up to 2 µJ, keeping the same focusing distance for each series of energies.

In Figure 3.1, the measured transmittance is plotted as a function of the pulse energy for the up, middle and down positions. Each point in the plot is the average value of three consecutive laser pulses fired onto the sample separated 5 µm or 10 µm depending on the applied incident energy. For the lowest incident energy values, the transmittance curves show a plateau at 90±2 %. This indicates a lack of absorption for these energies below a certain critical value. For pulse energies higher than this critical value, which is different for each examined sample position, the transmittance progressively decreases. This points out a partial pulse energy absorption by the sample. Since an exact energy value for the laser radiation absorption start is difficult to be determined directly from experimental data with precision, this critical energy for absorption by the material sample was determined at the crossing point between the horizontal line corresponding to data points presenting no absorption and the line fitted to the first points in which absorption can be clearly observed. Following this method, the values obtained for the critical energy are 112 nJ, 123 nJ, and 533 nJ for down, middle, and up positions, respectively. Thus, in terms of the energy threshold at which laser radiation starts being absorbed, there is little difference between the down and middle positions, whereas the up position shows a significantly different value.

Atomic Force Microscopy (AFM) reconstruction images of the material surface irradiated areas are shown in Figure 3.2. Different modifications were obtained depending on the focusing distance and the laser pulse energy used. Similarly to the results commented in the transmittance curves of Figure 3.1, the middle and down series show comparable morphologies and evolution. First signs of surface modification for the up position begin at higher pulse energy than for the down and middle positions. For the up series, surface modification begins at pulse en-
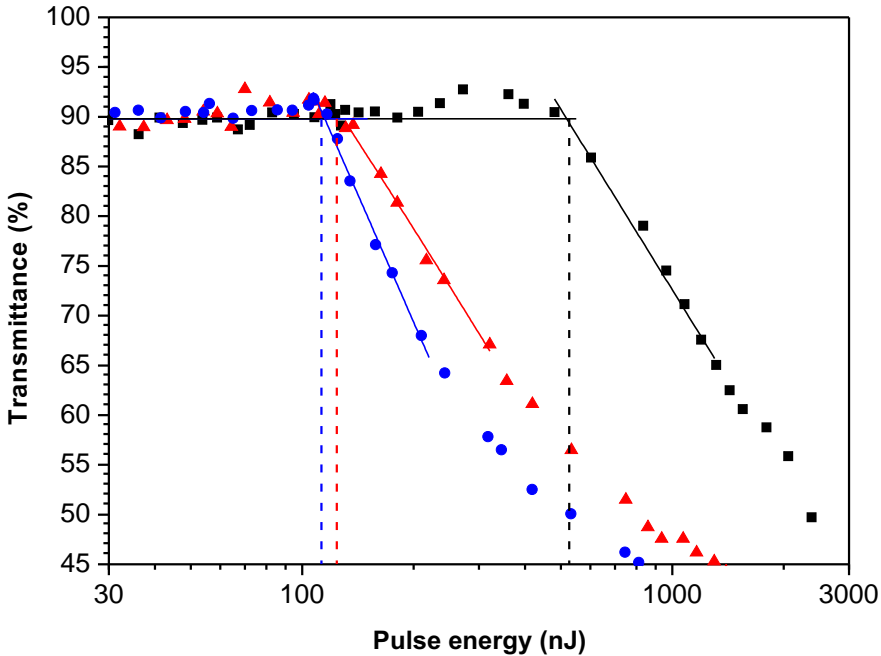
Figure 3.1: Plot of the transmittance vs. incident pulse energy for (**squares**) up, (**triangles**) middle, and (**dots**) down positions. Dashed lines correspond to the intersect value for critical energy determination.

ergies around 150 nJ, while for middle and down series the first signs of surface ablation appear at 110 nJ. Ablated spots at the middle and down positions show a shape in form of circular and ellipsoidal craters surrounded by a small rim, the height of which is one order of magnitude lower than the depth of the crater. In all the cases, crater size increases with pulse energy. On the contrary, craters formed at the up position present an irregular shape. Therefore, this position should be disregarded for high precision ablation.

Despite the similarities between the middle and down series, spots produced at the middle position seem to be slightly smaller than spots obtained with the same incident energy at the down position. Additionally, submicrometric bumps with a height about 20 nm appear when sending pulses of 100 nJ and 105 nJ at the down position. However, these bumps do not appear in the middle series. It has been shown that laser irradiation of PMMA at fluences near the ablation threshold produces bumps at the material surface due to hydrodynamic expansion of the hot

material below the surface [118]. These bumps might appear in the down position because the energy absorption takes place in a position located slightly inside the sample at incident energies close to the energy threshold, while for the middle position the energy would be focused a bit outside from the material surface.
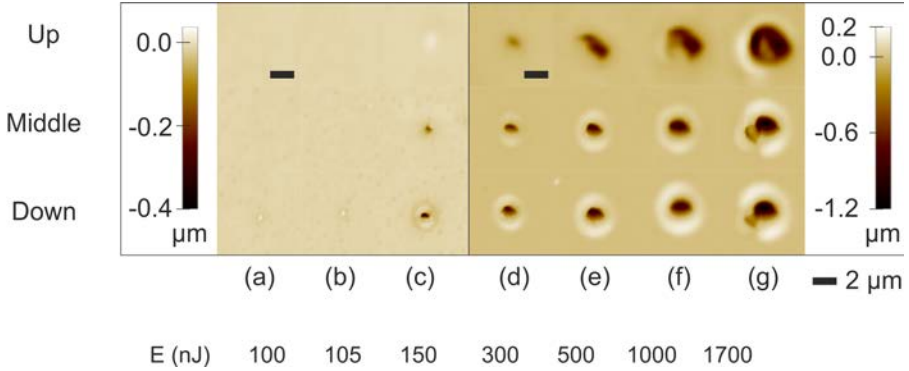
Figure 3.2: AFM images of the PMMA surface after the incidence of a single pulse of (a) 100 nJ, (b) 105 nJ, (c) 150 nJ, (d) 300 nJ, (e) 500 nJ, (f) 1000 nJ, and (g) 1700 nJ at different positions: up, middle and down. The height scale on the left is for (a), (b) and (c), while the height scale on the right corresponds to (d), (e), (f) and (g).

For pulse energies above 1 μJ, some irregularities in the aspect of the craters can be observed. This behavior seems to correspond with changes in the energy distribution of the laser beam. These could be produced by the self-focusing effect in the glass elements of the focusing device [119]. Taking into account that the critical power for glass is 2.5 MW [120] and that the pulse duration is 450 fs, this effect would appear for pulse energies higher than 1.1 μJ.

The radii of the craters were measured at a depth corresponding to a 10 % of the total depth for each crater. Taking into account the Gaussian energy distribution of the laser beam and that the material presents a fluence threshold for ablation (F_{th}), the square of the crater radius (r) should follow a logarithmic trend with the pulse energy (E_p):

$$r^2 = -\frac{\omega^2}{2} \ln \left(\frac{F_{th} \pi \omega^2}{2} \right) + \frac{\omega^2}{2} \ln(E_p), \qquad (3.1)$$

where ω is the laser beam radius at the surface for each studied z position. As it
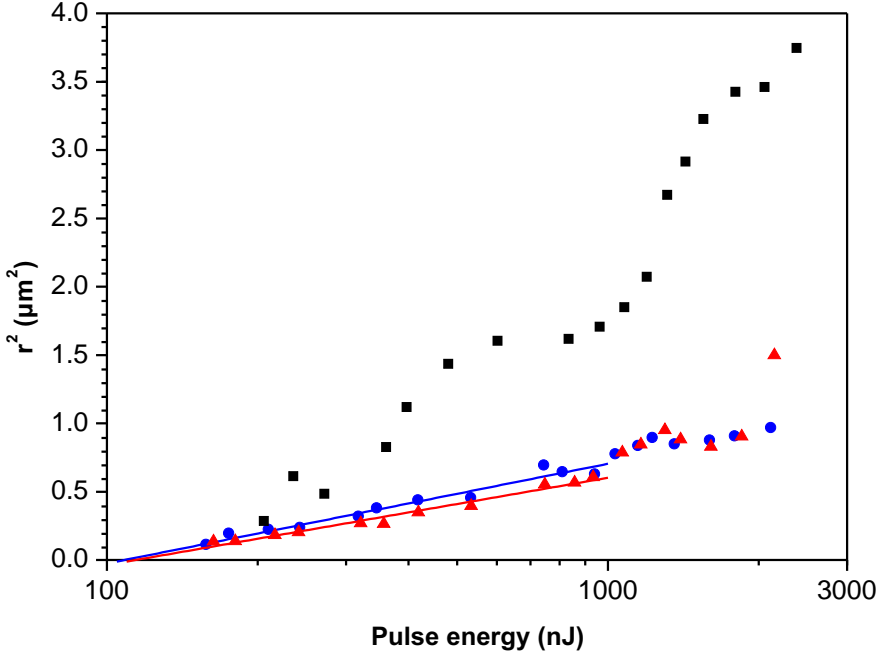
Figure 3.3: Plot of the radius squared of the craters vs. incident pulse energy for (**squares**) up, (**triangles**) middle, and (**dots**) down positions. Solid lines correspond to fits of expression 3.1 for the middle and down series.

can be identified in Figure 3.3, the semi-log plot of the radius squared against the pulse energy follows a linear trend for the down and middle series in the range from 135 nJ to 1 μJ, where self-focusing effects do not interfere in the ablated spots. However, this behavior is not clear for the up series.

From the fitted linear trend, F_{th} and ω for the middle and down positions could be determined from the data of the middle and down series in Figure 3.3 through the expression 3.1. The values found for ω were 0.7±0.1 μm for the middle position, and 0.8±0.1 μm for the down position. The corresponding threshold fluences found were 13±4 J/cm^2 for the middle series and 10±4 J/cm^2 for the down series.

Given that the peak fluence (F_p) of a Gaussian beam follows the expression

$$F_p = \frac{2E_p}{\pi\omega^2},\tag{3.2}$$

the corresponding pulse energy thresholds for the middle and down positions were 101±42 nJ and 104±48 nJ, respectively. These energy threshold values for ablation correspond quite well with the critical energy values for absorption found before from the transmission measurements (Figure 3.1), taking into account the experimental margin of error. On the contrary, according to the results found for the up position, this method used for finding the threshold energy cannot be extended to z positions in the vicinity of the top position.

The next observation that stands out is the confirmation that, for the same incident energies, craters produced at the middle position are similar or slightly smaller than those produced at the down position. Again, craters at the up series are much larger than the ones obtained at the middle or down positions. If the focused beam Rayleigh length z_R for a real beam with a certain M^2 quality factor is considered, the already introduced formula 2.5 changes to

$$z_R = \frac{\pi\omega^2}{M^2\lambda}.$$ (3.3)

Taking the ω value for the down position and $M^2 = 1.4$, the calculated value is $z_R = 1.4$ μm. With that stated, the confocal parameter b (also known as depth of focus), which is twice the Rayleigh length, takes a value of $b = 2.8$ μm. This value gives an idea of the extension (along the propagation axis) of the focal volume of the laser beam, where the middle and down positions can be found. In effect, these two z positions are separated by approximately 1.5 μm as it can be noted in Figure 2.9. However, the up z position lays outside from the focus region, since it can be found at 3.0 μm from the down position[1]. In this case, since the sample is outside the beam waist region defined by the Rayleigh length, the laser beam focus is located in the air. According to results presented in [121], the laser fluence reached in the air at the focus might induce the formation of a small plasma that could lead to electrical breakdown and temperature gradients that can locally modify the refractive index of the air. These conditions can alter the fluence distribution along the propagated laser beam, which can show an irregular profile after the focus. These circumstances could give an explanation of the irregular behavior observed for craters produced at the up position.

---

[1]The down position is taken as a reference to determine the laser beam waist position according to results presented in the following subsection 3.1.2.

These results point that working on conditions where the transmittance is just starting to decrease is not the best choice for achieving precision and control in surface ablation. Additionally, it can be observed that there is a range of around 1.5 µm in which middle and down positions are found, where the sample surface can be placed and very similar features can be obtained with precision and control. Further results in this direction are given in the following subsection 3.1.2.

The ablated volume of the craters was calculated from the AFM measurements. The results are plotted in Figure 3.4a as a function of the incident laser pulse energy. In this plot, the ablated volume follows a linear trend with the pulse energy for energies up to 400-500 nJ, depending on the series. At higher energies, the ablated volume continues increasing but with a higher dispersion of the data. The middle series presents the lowest dispersion in all the range of studied pulse energies. At low pulse energies, the down position shows the best efficiency in material ablation from the point of view of the energy sent onto the sample. On the other hand, if the ablated volume is represented as a function of the absorbed energy during the process (Figure 3.4b), there is not almost any difference between the down and middle series. This shows a direct correlation between the amount of material removed during ablation and the amount of absorbed energy.

All these results show that there is a range between the middle and down positions in the z-scan where the performance of surface ablation does not significantly change, whereas craters formed at the up position present an irregular tendency. Therefore, the up position should be disregarded at first instance for high precision ablation.

Concerning the middle position, the analysis of the data from measurements of the crater sizes concludes at first sight that this position is where the best resolution for ablation on the surface of the sample can be achieved. Thus, it might be concluded that the middle position would correspond to the position where the surface of the sample is closer to the beam waist in comparison to the up and down positions. More complete and reliable results on this topic are presented in the following subsections.

Furthermore, any change in the focusing distance between the sample surface and the laser beam waist can be easily detected and corrected at the middle posi-
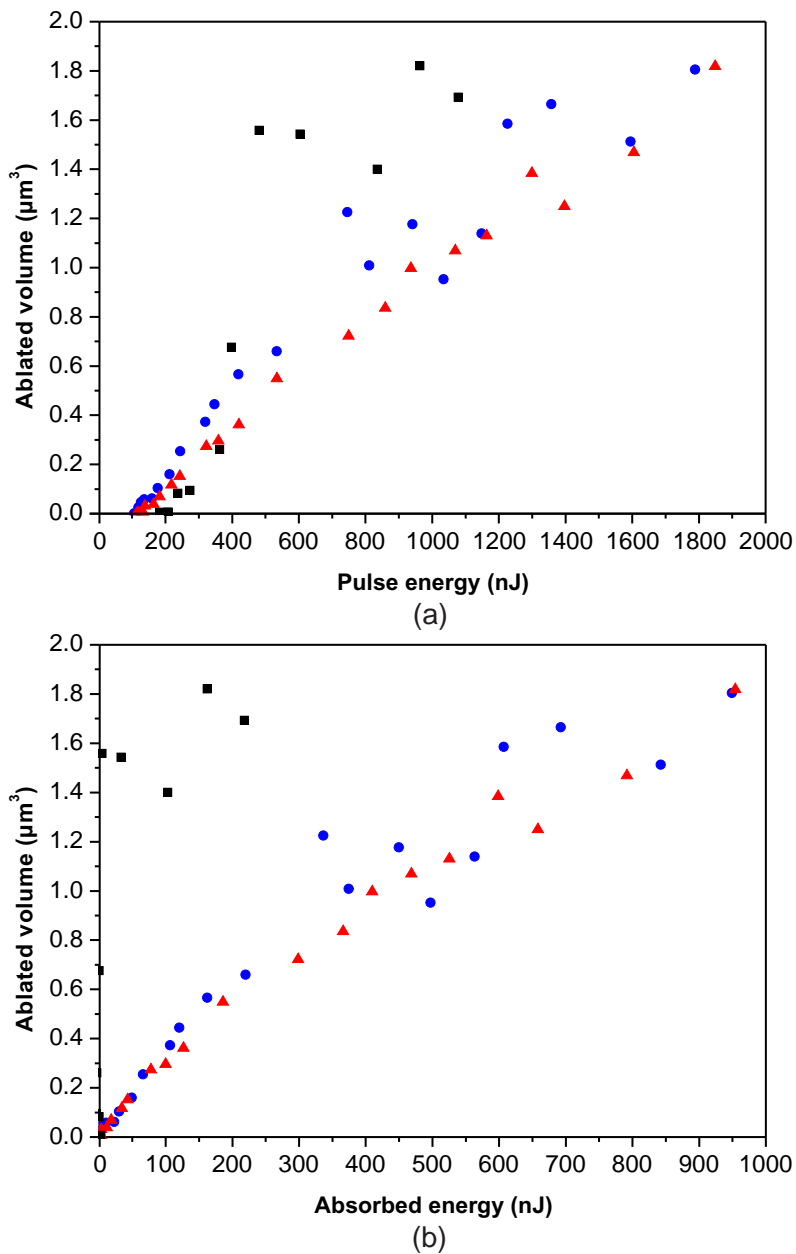
Figure 3.4: Plot of the calculated ablated volume vs. (a) the incident pulse energy, and (b) the absorbed energy for (**squares**) up, (**triangles**) middle, and (**dots**) down positions.

tion by monitoring the transmittance and then correcting the position in-situ during the ablation process. As it can be observed in Figure 2.9, this procedure can be easily implemented at the middle position because the transmittance drop curve at this point shows that a decrease in the measured transmittance is directly related with a displacement of the laser beam waist inwards of the material. Likewise, an increase of the measured transmittance indicates a shift of the laser beam waist outwards.

In the case of the down position, the sizes of the craters are similar to the ones produced in the middle positions, but changes in the transmittance might not be that efficiently detected when the laser beam waist is in the bulk. As it can be observed again in the same Figure 2.9, a displacement of the laser beam waist towards the inside of the material at the down position might not produce any perceptible change in the measured transmittance if its value reaches the bulk plateau transmittance value.

3.1.2. Beam waist position determination

A deeper study on the last given conclusions was needed in order to complete the understanding of the behavior of surface ablation of PMMA for different focusing distances (z positions) between the material surface and the laser beam waist, with a particular interest in the determination of the specific position at which the material surface coincides with the laser beam waist. For this reason, experiments presented below contain further experiments where z-scan experimental data is combined with the characterization and analysis of the corresponding produced spots at the material surface together with a simulation of a more realistic profile of the laser beam waist. The expected dimensions of the laser-produced spots predicted by the results of the simulated beam waist profile gave a good description of the obtained experimental data.

Various z-scans corresponding to diverse incident pulse energy values are shown in Figure 3.5. In this figure, z positions start at -5 μm and end at 6 μm. As commented before, negative values correspond to sample positions where the laser beam waist is outside the sample. This range was chosen according to the change in the transmittance along a complete z-scan of 20 μm. During the first positions,

the value for the transmittance corresponds to the maximum value of 91±5 %. In these positions, the beam waist was far enough from the sample so the fluence at the surface is not high enough to modify the material. As the sample moved towards the beam waist, the fluence at the surface increased and as soon as it exceeded the material fluence threshold, laser pulses started being nonlinearly absorbed by the material. As a consequence, the transmittance decreased during a certain range of z positions. This range begins at different positions depending on the incident pulse energy. For instance, the position where the transmittance begins decreasing for the curve of 87 nJ is z = -1.8 μm, yet for 200 nJ it starts at z = -3.1 μm. This was expected since an energy increase implies a fluence increase at the surface that makes possible obtaining surface modifications at farther positions from the laser beam waist. At the end of the transmittance drop, for all the series of data points there is a position from which the transmittance presents a plateau at a constant value when the laser beam waist is inside the sample bulk. The transmittance value of this plateau decreases as the pulse energy increases. Again, higher incident energies imply a larger volume where the fluence threshold is exceeded and hence energy is absorbed. More absorption means less transmittance, and this is what can be observed in the bulk plateau transmittance values.

A z position range where the focusing distance between the sample surface and the beam waist can be efficiently tracked through transmittance measurements can be estimated from the range in z where the transmittance values start changing from the maximum value and until they arrive at the bulk plateau value, with different values for each incident energy. For 125 nJ this z range goes from z = -2.6 μm to z = 1.4 μm, resulting in a total z range of 4 μm.

According to AFM data, the appearance of most of the surface modifications corresponded to a crater shape (Figure 3.6). In the studied AFM images, it could be observed that as pulse energy increased, the depth of the craters also increased. In addition, it is remarkable that the crater depth and shape are similar in a certain range despite the z position changes for all the studied energies.

Some craters produced during the z-scans made at pulse energies of 87 nJ, 100 nJ, 125 nJ and 200 nJ are shown in Figure 3.7. In general, the craters had a circular shape during the first positions of the z-scans, but after a certain z position the aspect became a bit elliptical. The modifications on the surface are shown from
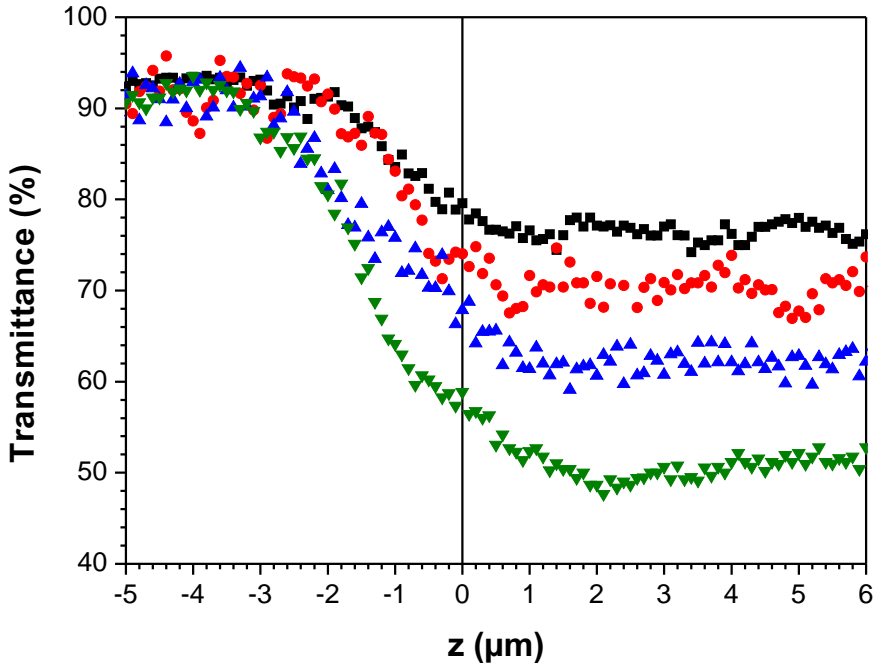
Figure 3.5: Transmittance values for z-scans produced with pulse energies of (**squares**) 87, (**dots**) 100, (**up triangles**) 125, and (**down triangles**) 200 nJ. The position z = 0 μm corresponds to the position of the laser beam waist determined according to results described in the following paragraphs.

left, where the beam waist was far from the sample, to right, where the sample moved towards the beam waist and ended within it. In this way, the first presented image shows the closest position where the laser did not produce any surface modification. After this position, the sample moved towards the beam waist and the fluence at the surface was high enough to produce ablation. Crater size started increasing as z position increased until it reached a range where the size seemed to be more or less constant. After this range, the crater size decreased gradually until the emergence of bump shaped modifications. They showed an appearance in form of bubble shaped structures that protrude over the surface level. The sizes of the bumps decreased as z position continued increasing until there were not any visible modifications or ablation on the sample surface. Bumps were present for all the studied z-scans.

Figure 3.8(a) shows a plot of the measured crater diameter versus the z posi-
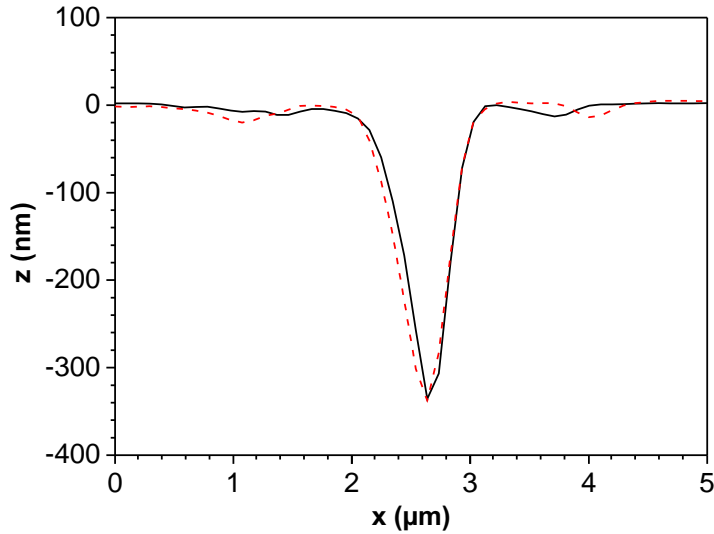
Figure 3.6: AFM profiles of two craters produced in the series done at 125 nJ of incident energy. The corresponding z positions for the profiles are (solid line) z = -1.9 µm and (dashed line) z = 0 µm.

tion. The measurements were obtained from SEM images like the ones in Figure 3.7. Comparing the crater size evolution with the z-scans in Figure 3.8(b), it could be identified for each z-scan that the first and smaller craters were produced just at the positions where transmittance started decreasing. Transmittance at this position almost corresponds to the highest value and virtually no absorption was detected. Right after, transmittance values decreased gradually as the dimensions of the craters increased. Then, there is a range of z positions where crater sizes are more or less the same, while transmittance values continued decreasing. This range ended at positions where the transmittance already reached the bulk plateau. The same trend could be observed in all the studied pulse energies. The average diameter in the flat central zone is 700±20 nm at 87 nJ, 835±25 nm at 100 nJ, 980±30 nm at 125 nJ, and 1.30±0.04 µm at 200 nJ. It is noteworthy that although transmittance values changed significantly, there was not any significant change in the crater sizes for all the z-scan experiments in this central z range. It was at the transmittance bulk plateau range that there was a decrease of the crater size and, finally, bumps appeared until no modification at the surface could be detected when the laser beam waist was well inside the material.
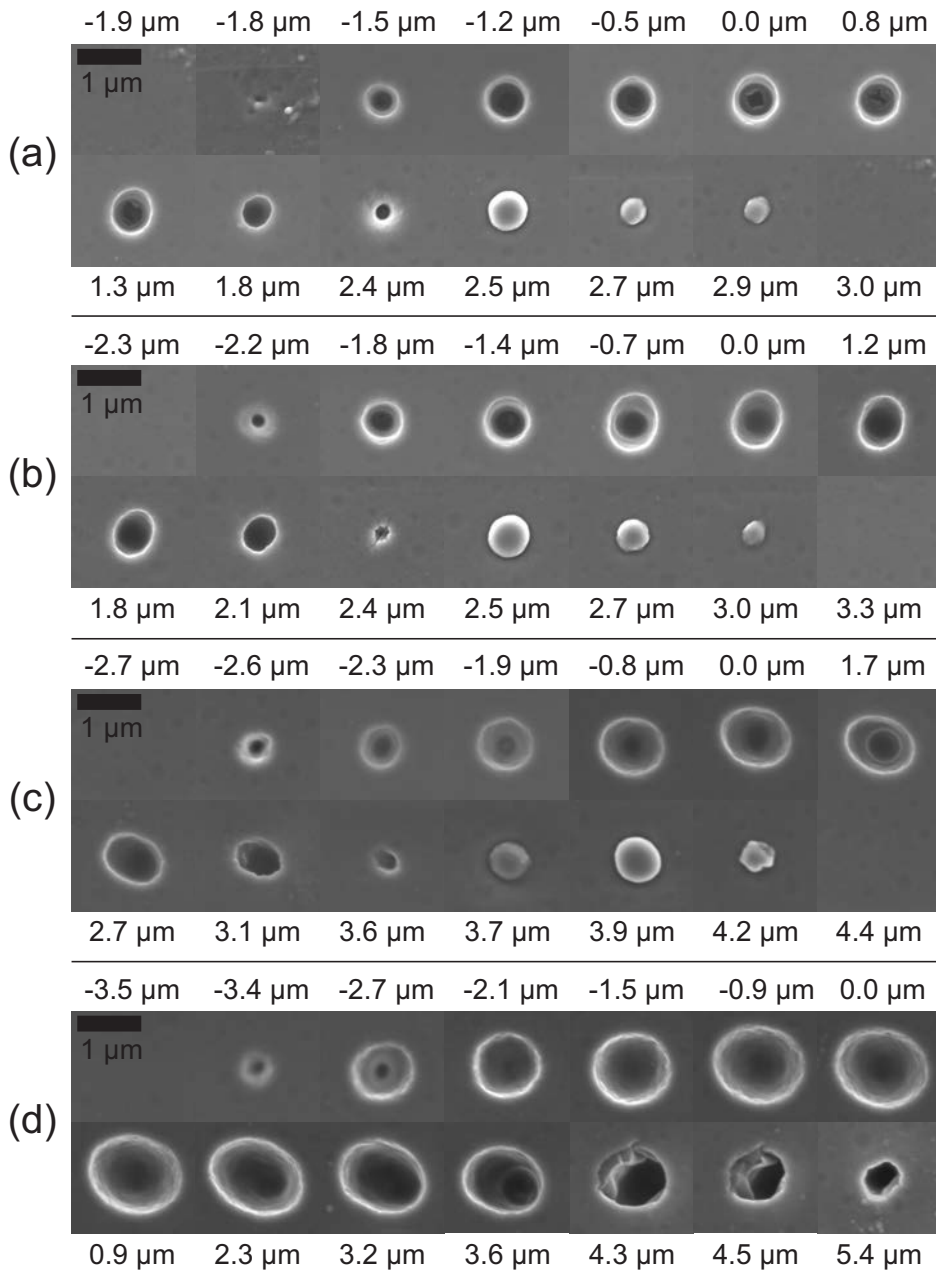
Figure 3.7: SEM images of the produced surface modifications. The corresponding pulse energies in each series are (a) 87, (b) 100, (c) 125 and (d) 200 nJ. The sample z position is indicated next to each image.
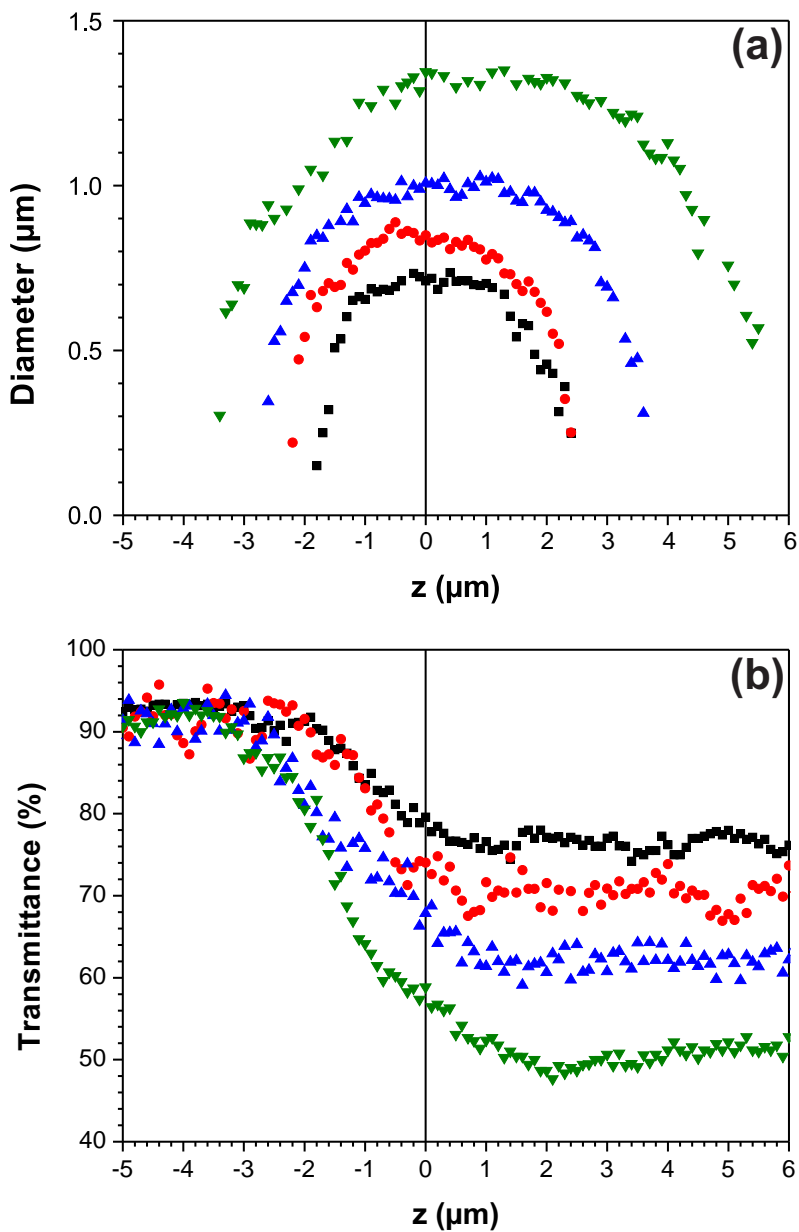
Figure 3.8: (a) Plot of the measured diameters vs. z position. (b) Transmittance values for z-scans produced at different pulse energies shown in Figure 3.5. The series were produced at constant pulse energies of (**squares**) 87, (**dots**) 100, (**up triangles**) 125, and (**down triangles**) 200 nJ.

Based on the results above, the often used method to determine the position of the laser beam waist at the location where the smallest surface modifications are produced is not correct, since the smallest modifications were obtained when the laser beam waist was at a certain distance from the surface, either outside or inside the sample, as it can be seen in Figure 3.8(a). With that in mind, it can be supposed that the position of the laser beam waist is probably located somewhere among the positions where the diameters of the craters are more or less constant. Assuming this hypothesis, the average values of the crater radii squared around the maximum values vs. the laser pulse energy were represented in Figure 3.9 in order to get information about the laser beam waist.
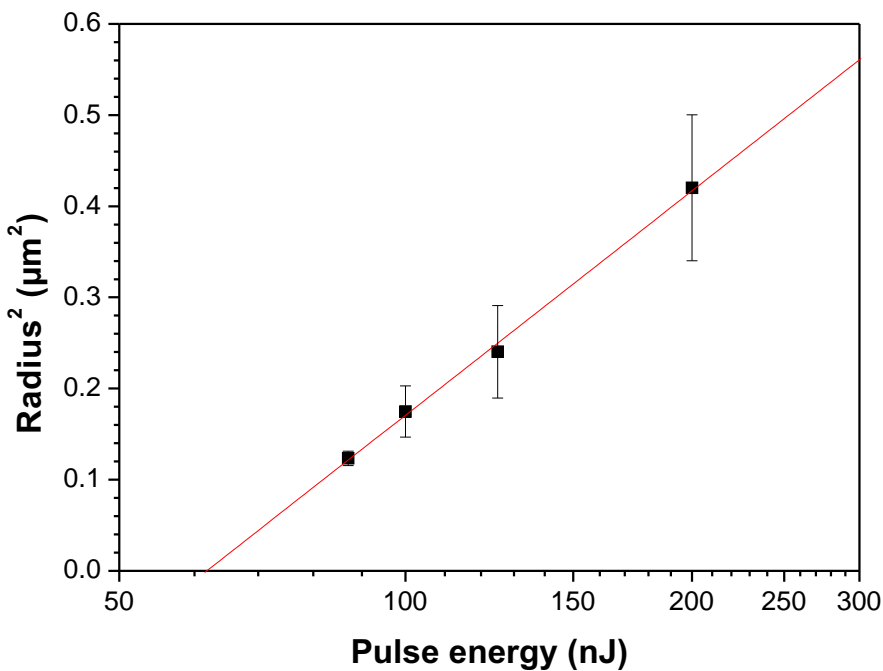
Figure 3.9: Plot of the radius squared versus the incident pulse energy. Error bars correspond to the experimental errors of the crater measurements.

The logarithmic correlation shown in Figure 3.9 suggests that the beam intensity profile is Gaussian at the beam waist, and that PMMA ablation is activated when the fluence on the surface overcomes a certain threshold value (F_{th}) [122, 123]. Therefore, the equation 3.1, which gives the ablated crater radius (r) at a given pulse energy (E_p) in a Gaussian beam, could be used to find the beam radius (ω)

at a certain z position of the beam waist, and the fluence threshold.

The fit gave a value for the threshold fluence of 5.5 ± 2.0 J/cm^2, and a radius at the beam waist of 0.84 ± 0.11 μm. Based on these experimental results, the comparison with the theoretical values for the focusing system gave a beam quality factor M^2 of 1.5, since the theoretical beam waist would have to be 0.55 μm. Following the M^2 model for the propagation of the laser beam, the radius at different z positions is given by equation 3.4:

$$\omega^2(z) = \omega_0^2 \left[1 + \left(\frac{M^2 \lambda z}{\pi \omega_0^2} \right)^2 \right],\tag{3.4}$$

where ω_0 is the radius at the beam waist, λ is the laser wavelength and z = 0 corresponds to the position of the laser beam waist [97]. The profile of the laser beam around the beam waist following this equation is plotted as a dashed line in Figure 3.10 for the z range of the calculated simulation results. When the theoretical values of the beam profile were substituted in equation 3.1 together with the experimental values for the beam waist radii and fluence threshold from the logarithmical fit, in order to calculate the theoretical evolution of the crater radius with z position (Figure 3.11), it resulted that the maximum crater size occurs at the beam waist position and that the craters with minimum size are obtained at the two symmetrical outermost points of the range at which craters should be produced. This outcome was in agreement with experimental results in Figure 3.8(a). However, this z range where craters should be produced was notably shorter than the one observed in the experiments. In addition, simulation results did not show a plateau of constant dimension craters for most of the simulated pulse energies; only a short one for the highest incident energy value of 200 nJ.

Gillen et al. [125] analytically demonstrated that the M^2 model fails to give a realistic description for the propagation of a clipped focused Gaussian beam. Depending on the clipping factor (usually referred to as γ and defined as the ratio between the size of the objective rear aperture and the size of the laser beam waist before entering the objective), the energy distribution around the laser beam waist can change considerably. In this work, the beam configuration corresponded to a low NA focusing configuration (the clipping is being performed on a Gaussian beam converging from $5\sqrt{2}$ μm to 5 μm in a Rayleigh range of 10 mm). For the
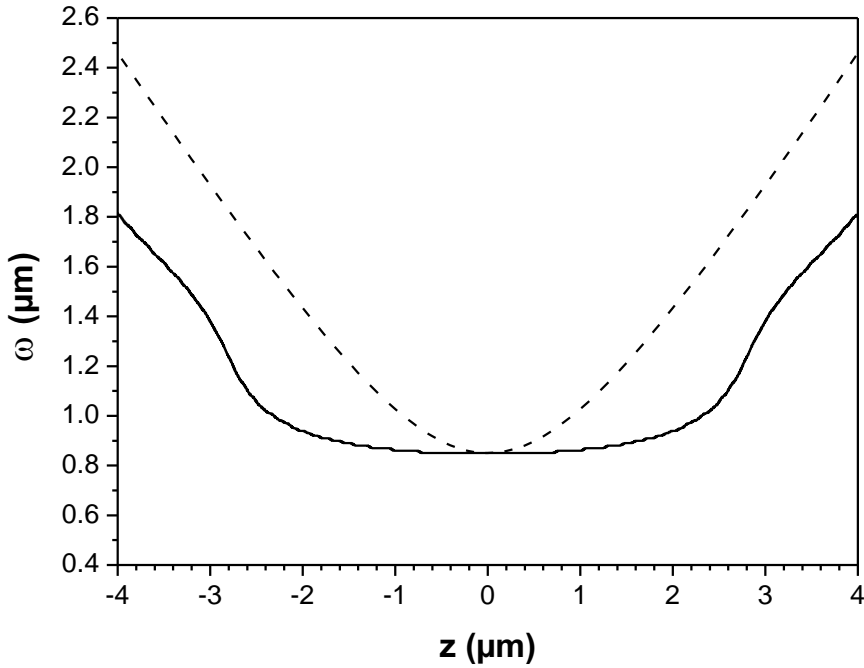
Figure 3.10: Calculated beam profile showing the beam radius evolution along the z axis for positions around the beam waist, which corresponds to z = 0 μm. Calculations were done following two different methods: the dashed line plot was calculated following the M^2 model [97], while the continuous line plot was determined through vector diffraction theory taking into account the clipping factor between the beam diameter and the rear objective aperture [124]. Actually this figure shows almost half of the complete beam profile: the whole laser beam profile would take values at the two plotted extremes z = ±4 μm from ω = 1.8 μm to ω = -1.8 μm.

conditions of the executed experiments, where a 0.55 NA objective was involved, the Richards-Wolf theory was implemented to simulate the propagation of the laser beam in the experimental system and so that a more precise intensity distribution around the beam waist could be found. This electromagnetic theory is the standard rigorous description of the focusing of a near paraxial beam through a high numerical aperture optical system (as in this case) and takes into account relevant experimental magnitudes: the size of the input laser beam, focusing lens data, working distances and specially the clipping factor, which in this experimental setup was γ = 1.2 [124].
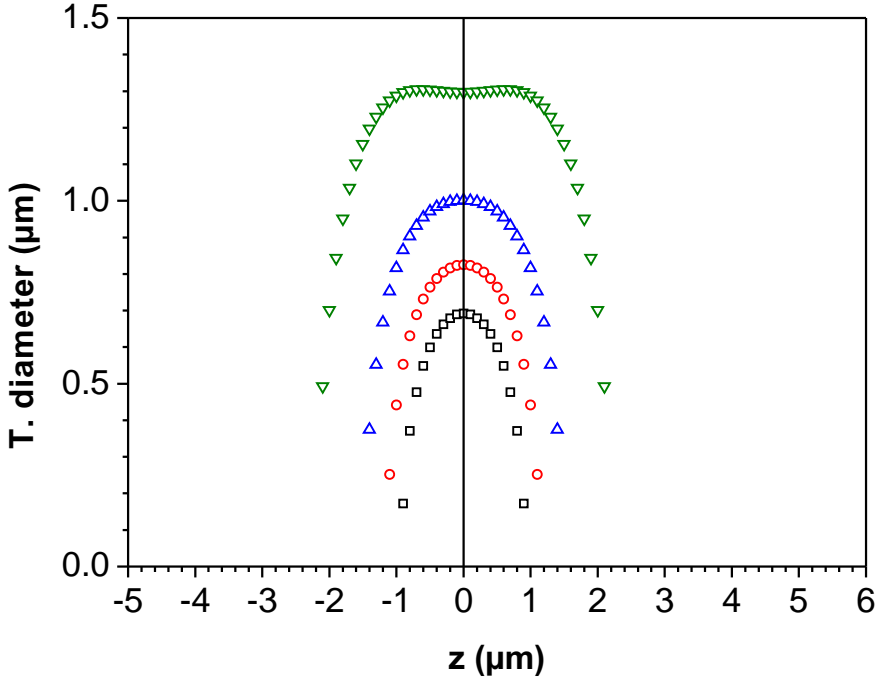
Figure 3.11: Plot of the theoretical diameters vs. z position following the M^2 model. The series were calculated for pulse energies of (**squares**) 87, (**dots**) 100, (**up triangles**) 125, and (**down triangles**) 200 nJ. The position z = 0 μm corresponds to the position of the laser beam waist.

Calculations showed that cross sections of the simulated intensity profiles close to the beam waist are nearly Gaussian. The simulated beam profile is plotted with a continuous line in Figure 3.10. Firstly, it has to be noted that the simulated results agree quite well with the size of the beam waist found experimentally. Besides, it can be observed that in these computed results there is a range of z positions around the beam waist where the beam has similar dimensions. This zone is much flatter and homogeneous than the presented by the M^2 model. According to these results, the simulated clipped beam propagation should present a better match with the experimental results.

Once that the simulated beam propagation gave the evolution of the beam dimensions along the z direction $\omega(z)$ and taking the value of the fluence threshold F_{th} obtained from the linear flit from the plot in Figure 3.9, it is possible to cal-
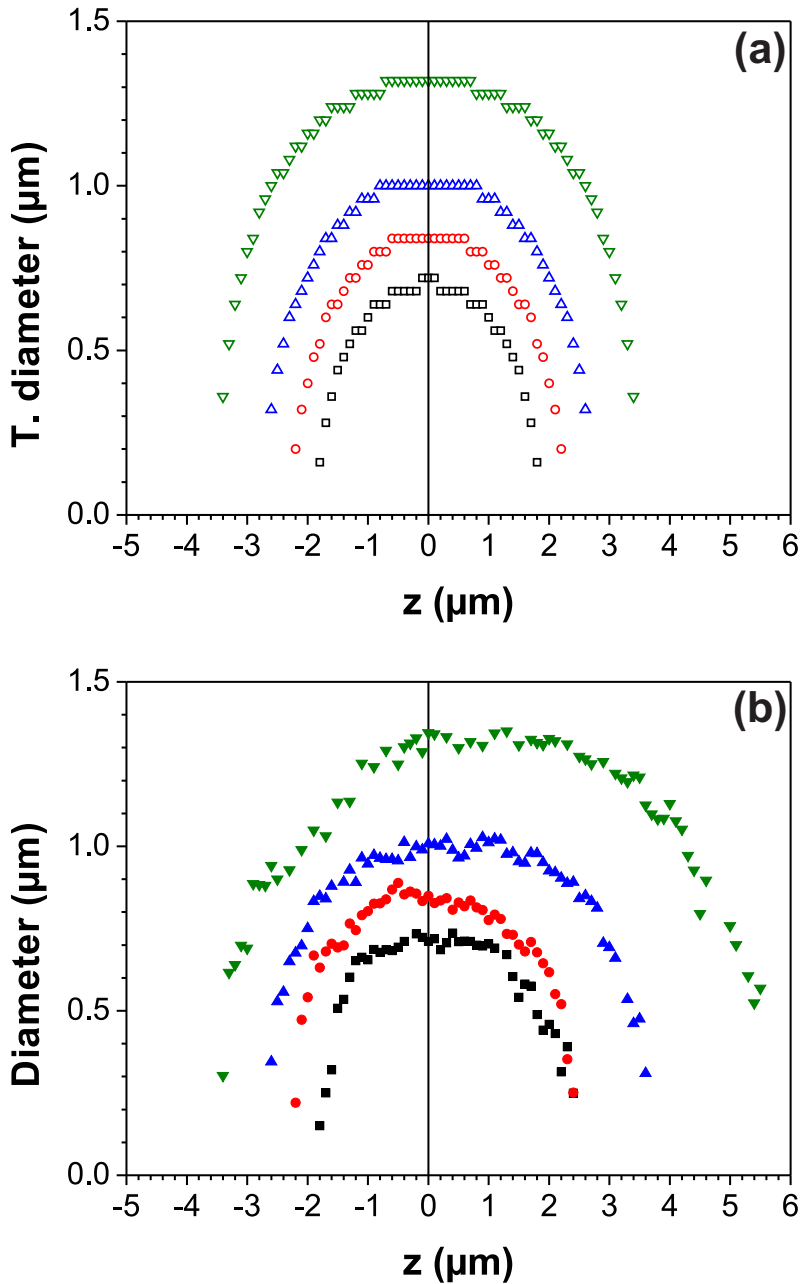
Figure 3.12: (a) Plot of the theoretical diameters vs. z position following vector diffraction theory propagation. (b) Plot of the measured diameters vs. z position. The series were produced with pulse energies of (**squares**) 87, (**dots**) 100, (**up triangles**) 125, and (**down triangles**) 200 nJ.

culate the predicted diameter of the ablated spot (crater) on the material surface, i.e., the diameter of the area on the sample surface where the fluence threshold is exceeded according to the beam size at the z position where the surface is located. These calculated crater diameters are plotted in Figure 3.12(a) for the different z position values. The position $z = 0$ µm corresponds to the position of the laser beam waist. From now on, this position will be used as a reference for all the following plots in this chapter.

Comparing the information plotted in Figure 3.12(a) and (b), it can be seen indeed that theoretical diameters are now in better agreement with the experimental data. In this figure, z position values of the measured diameters in Figure 3.12(b) where set in the following way for each series of constant laser pule energy: the first z position value of the measured diameters was adjusted to be the same as the first z position value in Figure 3.12(a), corresponding to the first z position where fluence exceeds the threshold. Accordingly, the first z position for the series at 87 nJ was adjusted to $z = -1.8$ µm, at 100 nJ it corresponded to $z = -2.2$ µm, $z = -2.6$ µm at 125 nJ, and $z = -3.4$ µm at 200 nJ. The rest of z position values for each series followed after this adjustment of the first z position in Figure 3.12(b). It is remarkable that diameter sizes of the modifications produced along the range of z positions where the laser beam waist is outside the sample agree quite well for all the studied incident energies. Afterwards, there is a region of z positions where the diameters of the craters keep a similar value. This trend can be associated with the flat zone near the beam waist where the beam size is almost constant. On the other hand, the results for positions after $z = 0$ µm in all the series do not agree so accurately with the experimental results. The real diameters were larger and surface modifications were present in a deeper range of z positions.

In order to better compare theoretical and experimental results, multiple results from the z-scan experiment made at 125 nJ were gathered in Figure 3.13. This figure shows three different plots: the transmittance curve of the z-scan, experimental diameter measurements of the produced craters and theoretical diameters calculated from the vector diffraction theory simulation. In this plot it can be seen that the first surface modifications began at positions where the transmittance started decreasing, as can be observed in Figure 3.7c. As the PMMA surface approached the position of the beam waist, the size of the modifications increased and the transmittance decreased gradually. After $z = 0$ µm, it can be seen that experimen-

tal craters had a larger size in comparison with theoretical ones. Besides, the last crater observed on the surface corresponded to the position z = 3.6 µm, while theoretical results indicated the last crater position at z = 2.6 µm.
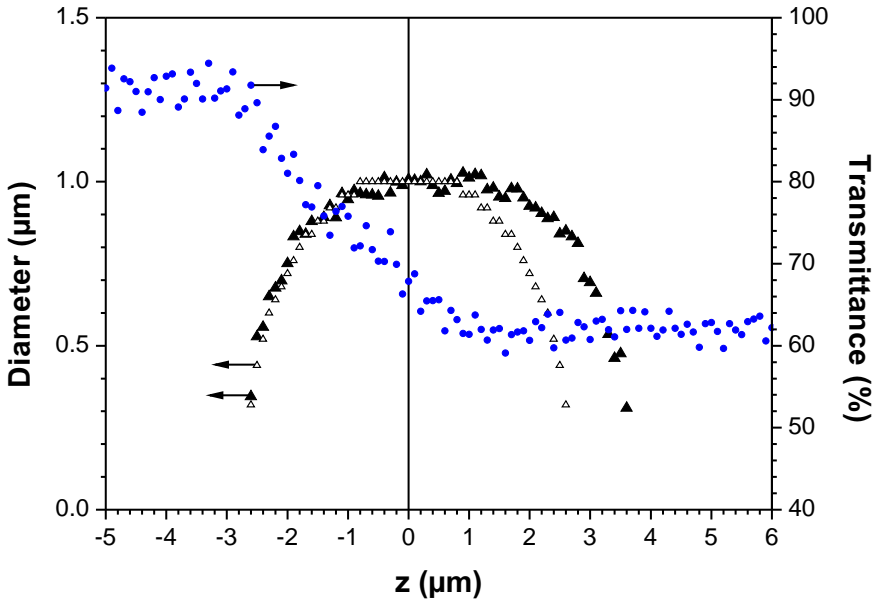
Figure 3.13: Plot of the experimental (**filled triangles**) and theoretical (empty triangles) diameters (left axis), and the corresponding transmittance curve (**dots**, right axis) for a z-scan experiment produced at an incident pulse energy of 125 nJ.

For the positions where the beam waist is outside the sample, the maximum energy density is located outside the sample. Therefore, there is not any significant interaction in the bulk and surface modification only depends on the local laser fluence. In contrast, when the beam waist is located inside the sample, the focalization in the bulk might produce certain modifications inside the material that can induce side-effects on the surface, modifying the expected size given by the fluence threshold. Furthermore, the formation of bumps only when the focalization of the laser beam occurs well inside the material reinforces this hypothesis about the effects that absorption inside the bulk material could have on surface modifications. As a consequence of energy absorption in the bulk, fractures in the polymer might appear together with the creation of gas which could expand inside the material, leading to an increment of the crater sizes beyond the area limited by the fluence

threshold and the formation of bumps when the peak fluence at the surface is well below this threshold [123].

In order to acquire knowledge about the morphology of the inner material below the irradiated areas, the Focused Ion Beam (FIB) technique was used to precisely ablate some of the craters of the z-scan made at 125 nJ for observation of their cross sections. SEM images of the FIB ablated areas are shown in Figure 3.14.

In these images it can be seen that the bulk material below the irradiated spots was affected in some of the z positions. The affected inner material presents a porous structure which elongates along the z axis according to the position of the sample with respect to the beam waist. For the positions shown in Figure 3.14a-b, the produced craters do not present any visible formation underneath. Starting from Figure 3.14c, it can be observed that each crater is followed by the formation of a porous structure with a length that increases as the beam waist moves into the sample (Figure 3.14c-k). This porous structure remains in all the rest of positions and at some point it is not possible to observe the total length anymore because the porosity seems to extend deeper as the beam waist enters the material. In Figure 3.14l-m, the porous structures beneath two bumps are shown. This structure might be produced due to expansion of the material near the surface, and at the same time, this produces the formation of bumps that can be seen in Figure 3.14l'-m' at an intermediate phase of FIB ablation. It is remarkable that neither the diameter nor the depths of the craters seem to have drastic changes for the different z positions as already seen with AFM, even though processes occurring inside the material that produce the porous structure certainly affect the surface. Moreover, the enlargement of the porous structure could be likely produced by self-focusing, since the critical power to produce this effect (in the range of 40 kW) is vastly overcome in these experiments [120].

There are some studies that simulated the behavior of the interaction between femtosecond lasers and different materials [94, 97, 120, 123–128], but a complete explanation of the ablation mechanisms still remains unaccounted. According to molecular dynamic simulations of the ablation of PMMA with a pulsed laser in the femtosecond regime [129], the formation of a crater on the surface of PMMA is a consequence of the presence of surface swelling followed by an expansion of the material underneath the irradiated area. After that, the expulsion of the irradi-
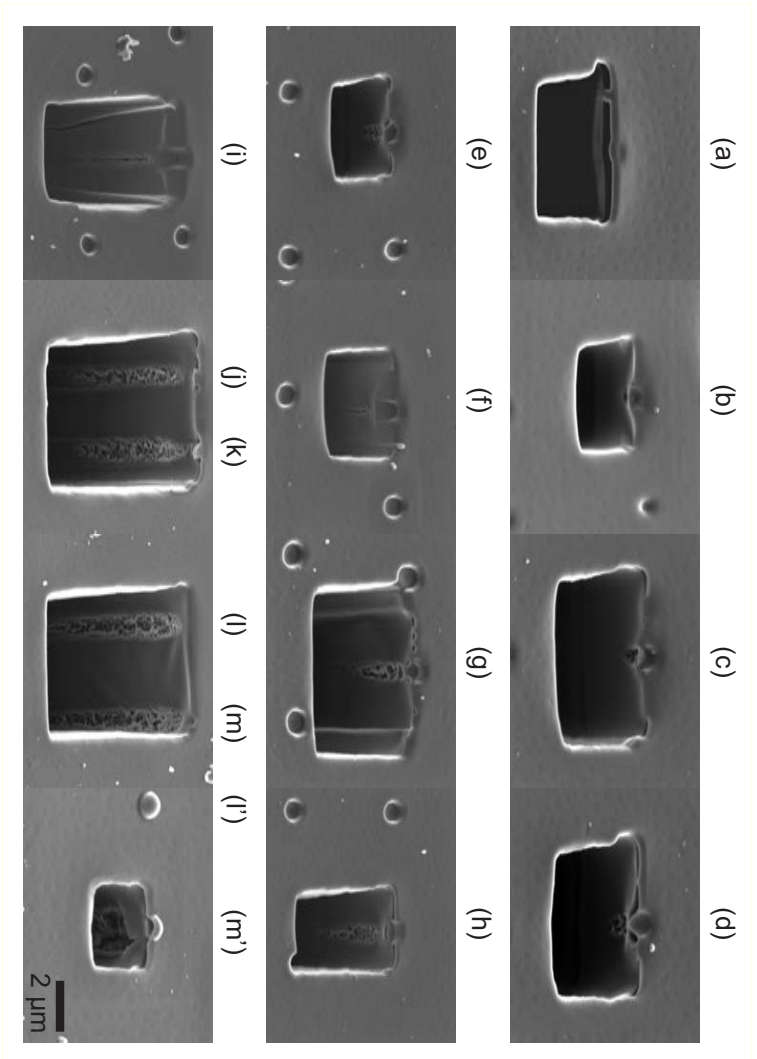
Figure 3.14: SEM images of the craters produced in a z-scan at an incident energy of 125 nJ showing a transverse section done on the material by FIB ablation (tilt: 45°). The z positions at which the craters were produced are (a) -2.6 μm, (b) -2.3 μm, (c) 1.9 μm, (d) -0.8 μm, (e) -0.4 μm, (f) 0 μm, (g) 0.5 μm, (h) 1.7 μm, (i) 2.7 μm, (j) 3.1 μm, (k) 3.2 μm. The images showed in (l) 3.9 μm and (m) 4.0 μm correspond to z positions where the irradiated area showed a bump instead of a crater. In (l') and (m') it can be seen the protuberances on the material surface in an intermediate stage of the FIB ablation process.

ated material produces a crater at the surface of the polymer. The reported porous structure beneath irradiated spots in the simulation [129] can be directly associated with the porous structure of the experimental results observed in Figure 3.14. Since the process of energy absorption depends strongly on the position of the laser beam waist relative to the position of the sample surface, the size and extension of the porous structures increase as the laser beam waist enters into the sample, as it could be clearly observed in Figure 3.14.

In view of these results, it could be concluded that craters made at positions where the transmittance value is the closest to the maximum of $91\pm5\%$ correspond to the z positions where the sample must be placed to produce strictly surface ablation without any modification in the bulk material (Figure 3.14a-b). This position is very critical, since slight changes in the position of the sample with respect to the beam waist could lead to energy absorption in the bulk or no absorption at all. For this reason, when a reliable placement of the laser beam waist on the surface is required, the sample should be placed in an intermediate zone in the transmittance curve. In addition, in this zone the sample position is not so critical since there is a range where the sizes of the modifications do not significantly change. Besides, the position can be controlled with high accuracy through the simultaneous tracking of transmittance values at each z position. However, it is important to keep in mind that the material will be modified not only on the surface but also in the bulk, as shown in Figure 3.14c-m. Finally, in order to produce bump structures, the sample must be placed in positions where the transmittance curve arrives at the bulk plateau. Once more, this position is quite critical, since slight changes of the focusing distance between the sample and the beam waist can lead to undesired crater formation or no bump presence due to an eventual absorption in the bulk, with no perceptible effect on the surface. Additionally, there is not any possible control in the positioning through transmittance values because for these positions they correspond to the bulk plateau with a constant value.

3.1.3. Transmittance measurements during laser surface scanning for channel fabrication

Once it was possible to determine with precision the position of the laser beam waist with respect to the material surface, transmittance measurements simultane-

ous to scanning the laser beam along the surface to produce superficial patterns were studied. Unlike in all the previous experiments where only one laser pulse was fired at each spot of the material surface, in the production of patterns various pulses overlap and accumulate along the marked pattern on the sample. This situation leads to the probable presence of incubation effects, which could modify transmittance measurements registered during the marking process. These effects are associated to the incidence of laser pulses on a region of the material that has been already irradiated and therefore modified [130]. The altered region might contain defect centers and modified chemical properties, leading to a different absorption through the modified material structure and energy bands with a reduced fluence threshold.

The goal of the following presented experiments and results will be describing and analyzing the produced patterns and how transmittance measurements behave during this process in comparison to previously obtained results for single spot ablation.

As a first step to control and ensure the correct positioning of the sample at the different focusing distances where lines were produced, z-scan transmittance measurements were performed previously to the production of lines. In Figure 3.15 it can be seen how the transmittance changes for a single pulse on pristine material for different focusing distances (z positions) between the sample surface and the laser beam waist at the incident energies used in the experiments for both spots and lines fabrication. As previously commented in similar plots, the value $z = 0$ µm corresponds to the case where the sample surface lays at the beam waist position according to the results shown in the previous subsection 3.1.2.

After this first step, the laser beam could be scanned along the surface to produce lines at several focusing distances. Each series of lines was produced at a fixed incident energy and separation between the impinging laser pulses, in other words, at a fixed scan speed. The used incident energies took values in the range from 100 nJ to 300 nJ. Two values for the separation between consecutive laser pulses were explored: 0.2 µm and 0.5 µm, which correspond respectively to 200 µm/s and 500 µm/s scan speeds at a laser repetition rate of 1 kHz. While keeping these parameters fixed, lines at different z positions were produced by scanning the sample surface horizontally along 2 mm in the direction perpendicular to the laser
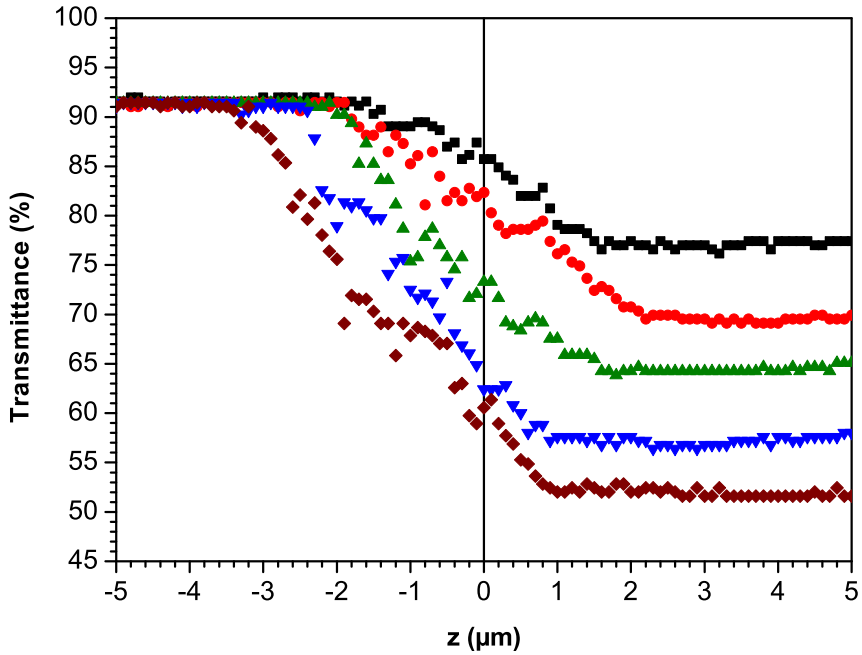
Figure 3.15: Plot of the transmittance vs z position at (**squares**) 100, (**dots**) 130, (**up triangles**) 150, (**down triangles**) 200, and (**diamonds**) 300 nJ of incident energy. The experimental relative error corresponding to all transmittance data is 5 %.

polarization. The range of z position values at which lines were produced was chosen according to the single pulse transmittance drop range for the different incident energy values. This range gets wider for higher incident energy values (Figure 3.15).

Transmittance was measured simultaneously to line ablation for all the series. This made possible to obtain the average transmittance of the laser pulses employed for the fabrication of every line. The obtained series of data are represented in Figure 3.16 for the different conditions used to fabricate the lines. The average transmittance measured during line production (Figure 3.16) followed trends similar to the z-scans obtained with single spots (Figure 3.15). In both cases, the z position range where transmittance decreases widened with increasing incident energy, as well as the transmittance values got lower for increasing incident energies. On the other hand, the transmittance values registered at the same experimental conditions (incident energy and z position) were generally lower in the case of av-
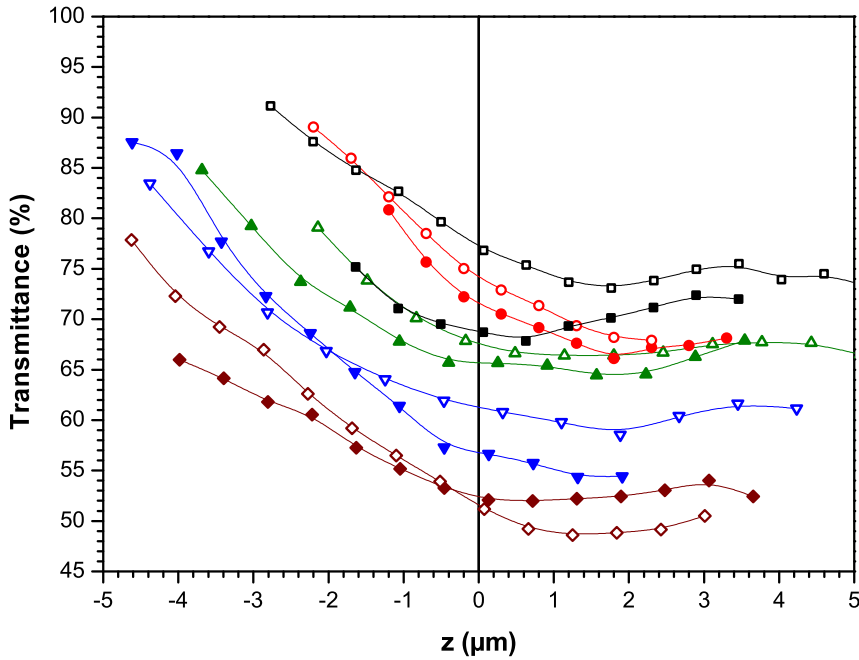
Figure 3.16: Plot of the average transmittance vs z position for (empty symbols) 0.2 μm, and (filled symbols) 0.5 μm of spot separation and for (**squares**) 100, (**dots**) 130, (**up triangles**) 150, (**down triangles**) 200, and (**diamonds**) 300 nJ of incident energy. The average value corresponds to transmittance measurements registered during the fabrication of each line. Lines connecting data points are just a guide to the eye. The experimental relative error corresponding to all transmittance data is 5 %.

erage transmittances measured during line fabrication than in previous single shot z-scans. This comparison also showed that the range in z where the transmittance decreases is clearly wider for line ablation than for single shot ablation. Both, the wider range of the transmittance decrease and the lower transmittance values for lines than for single spots can be associated to accumulative effects due to spot overlap [130].

In Figure 3.17 it can be seen how line ablation at the surface evolves for different focusing distances. This figure shows SEM images of one series of lines produced at 100 nJ of incident energy and 0.2 μm of spot separation between consecutively impinging laser pulses. It can be observed that continuous lines at the surface are obtained for z positions around z = 0 μm. More concretely, at these experimental
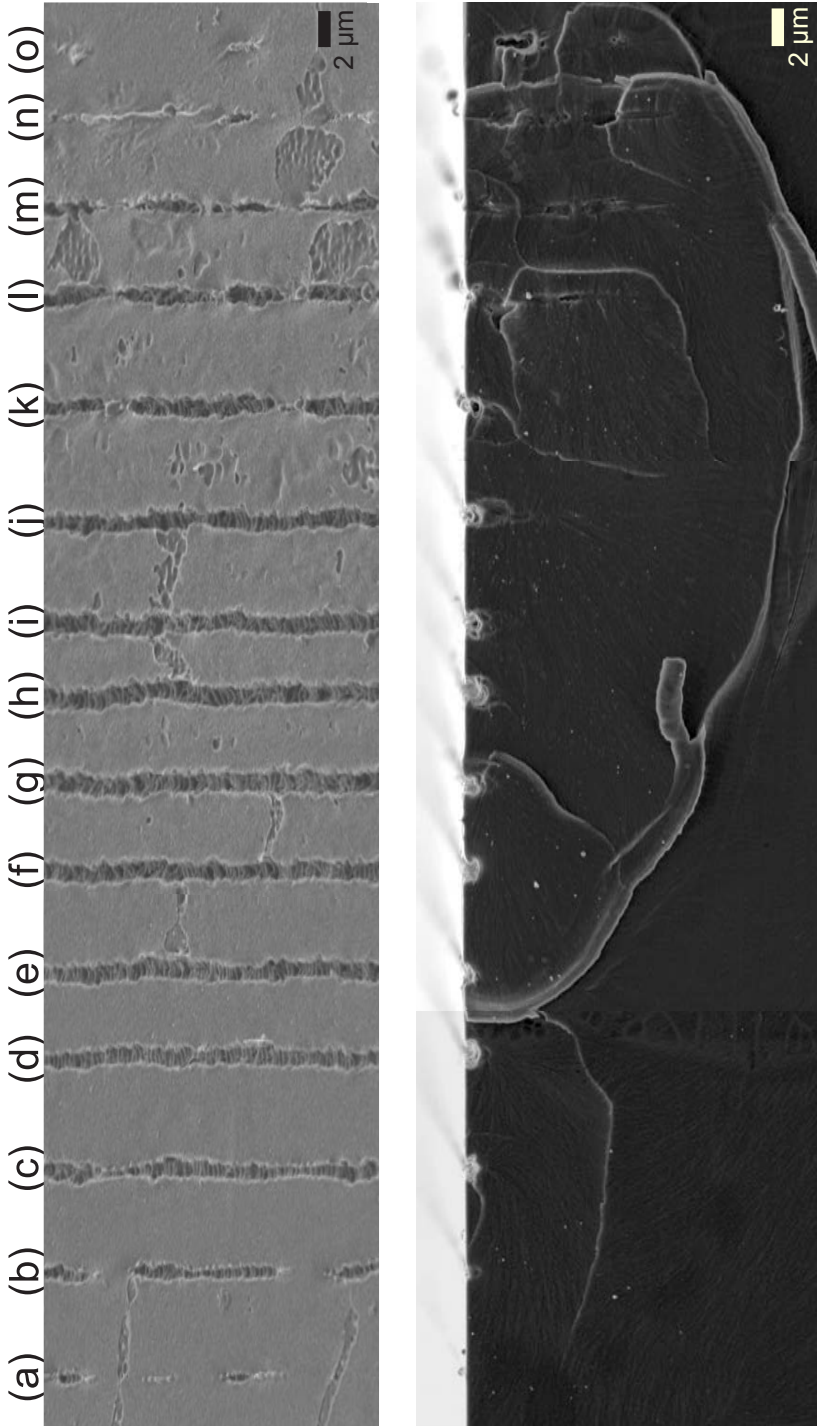
Figure 3.17: (Top) SEM images of the PMMA surface after the incidence of pulses of 100 nJ separated 0.2 μm at (a) -2.8, (b) -2.2, (c) -1.6, (d) -1.1, (e) -0.5, (f) 0.1, (g) 0.6, (h) 1.2, (i) 1.8, (j) 2.3, (k) 2.9, (l) 3.5, (m) 4.0, (n) 4.6, and (o) 5.2 μm for the z position values. For these surface images, the sample had a tilt of 30°. (Bottom) Corresponding SEM images of the PMMA cross section and part of the surface.

conditions continuous lines are observed on the surface from z = -1.6 μm (Figure 3.17c) to z = 2.3 μm (Figure 3.17j). These correspond to z positions in the transmittance decrease range in Figure 3.16. This correspondence was also observed for the other experimental conditions of incident energy and spot separation at which lines were produced.

The morphology of the lines at the sample surface could be inspected as well as its cross section profile. In the surface visualization, it could be observed from left to right how the progressive approach and entrance of the sample surface into the beam waist region affected the obtained lines. At the beginning, the external situation of the beam waist with reference to the sample surface produces that the fluence at the surface is not high enough to reach the ablation threshold along all the scanned distance and the lines are not continuous. For pulses of 100 nJ and 0.2 μm of spot separation, these correspond to z position values of Figure 3.17(a) and (b). Here the position of the sample is very critical and irregularities larger than the surface roughness like small movements of the sample holder and stages, defects, and scratches among other imperfections on the sample surface result in a discontinuity of the lines.

For closer positions of the sample to the beam waist, lines are continuous along all the scanned distance (2 mm), Figure 3.17c-j. At first sight, the width of the lines does not significantly change during these different z positions. Only at the beginning and at the end of this range of z positions, lines look slightly thinner than for the central z positions. Deeper positions of the beam waist with respect to the sample surface make that the pulse energy is mostly concentrated below the surface (range of Figure 3.17k-n). Thus, the fluence at the surface is not high enough to ensure a continuous line ablation at the surface and lines start becoming discontinuous again. Here some swelling of the not superficially ablated part of the line is observed. Finally, when the beam waist is well inside the sample, almost no surface modification is present except in some short segments, where small surface swelling is visible. This corresponds to the case of the z position value of Figure 3.17o. No surface modification would be expected for deeper positions of the beam waist with regard to the sample surface [131].

Another feature that can be examined in the surface images is the roughness of the bottom of the channels (see Figure 3.18). The roughness presents a quasi-

periodic porous structure with some ripple ordering for incident energies up to 150 nJ. The direction of these porous structures is perpendicular to the line direction. This feature was previously observed in similar studies [118] where the ripple direction coincides with the incident linear laser polarization, which is parallel to the sample surface and perpendicular to the scan direction of the lines. For higher energies, the porous structures become more randomly distributed in terms of the profile of the structures, but the orientation of the ripples perpendicular to the line direction is kept. The average periodicity of the ripples seems to be independent of pulse energy and z position, and has a value 350 nm, which is in agreement with results on periodicity of the ripples observable at the bottom of lines produced by laser ablation on PMMA [132]. The origin of these ripples has been previously explained as a consequence of the interference between the incident laser radiation wave and the surface scattered wave, which is considered a particular instance of the results obtained with interference of surface plasmon polaritons with the incident laser radiation [132–134].
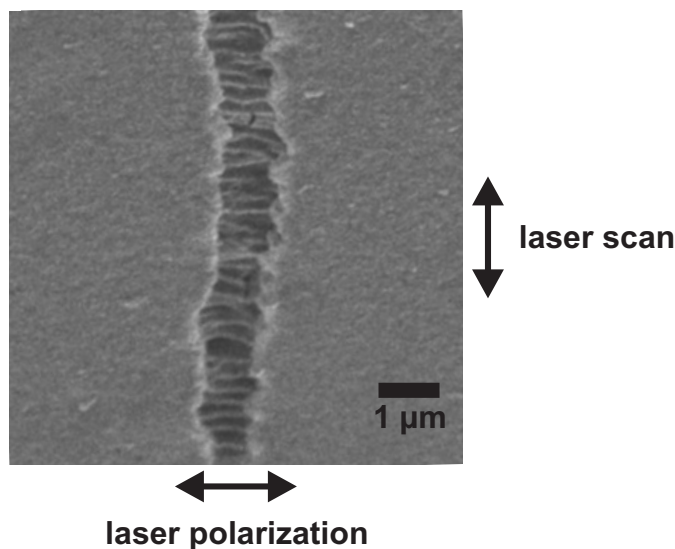
Figure 3.18: Enlarged view of a segment of the channel in Figure 3.17d. Periodic ripples at the bottom of the channel are parallel to the laser light linear polarization and perpendicular to the direction of the channel.

The bottom part of Figure 3.17 corresponds to the cross section of the PMMA

sample and made possible the visualization of the profiles of the lines and the material modifications produced under the surface. In the same way as in the surface images of the top part of Figure 3.17, the effect of the beam waist entering the sample was studied. At an external position of the beam waist with respect to the sample surface (Figure 3.17a), no inner modification is visible. Just some surface swelling in form of bumps can be seen at the surface, forming the previously commented discontinuous line. When the sample approaches to the beam waist, lines are produced at the surface (Figure 3.17b-j). Two groups of lines can be distinguished in this range: from Figure 3.17b to Figure 3.17f and from Figure 3.17g to Figure 3.17j. In the first group, only the profile of the lines can be seen, without any modification under the channels. The profiles of these lines show quite vertical walls and a flat bottom. The profiles of the second group of lines show a narrower width at the surface and a circular profile. The dimensions of the profiles become smaller for higher values of the z position. Furthermore, inner modifications appear in the material under the bottom of the lines. These modifications elongate as the beam waist goes deeper into the sample. For lines produced at deeper positions (Figure 3.17k–n), the sample surface clearly presents swelling in form of a line of successive bumps. At these positions, the inner modifications become considerably more elongated and extend some microns inside the material in the incident beam direction. Lastly, it can be observed that for an inner z position there is not any visible surface modification (Figure 3.17o). Instead of this, a cavity appears under the surface. Material modifications under this cavity can be seen like in the previously described lines. The presence of these inner material modifications are not exclusive of line production since they were also observed in single spot ablation, as seen in Figure 3.14. The presence of a region with modified material under surface ablated areas was already obtained in simulations that study femtosecond laser radiation absorption in PMMA [129], and also observed in studies of craters and lines produced at the surface of PMMA [118]. Thermal expansion of the material with formation of gaseous nanopores at the region where the laser pulse is focused and multiple filamentation inside the material for the case of doped PMMA are two mechanisms that were used to explain the presence of this region with modified material [118, 129].

Very low thermal affectation is observed in the SEM images of the lines. Well-defined contours in the surface image as well as profiles from the cross section, and the observable roughness of the bottom of the channels indicates the absence

of noticeable thermal side effects despite accumulation is present because of the overlapping pulses used to produce continuous lines.

The general behavior of the line production regarding different z position values for the rest of experimental conditions of incident energy and spot separation at which lines were produced is the same as the described above, with some differences in the extension of the z position range for each case. On the other hand, it should be noted that large cracks extending mainly in the horizontal direction along the whole sample in the cross section SEM image (Figure 3.17 Bottom) correspond to fractures of the conductive graphite thin layer that was coating the PMMA sample in order to make possible its analysis with the SEM. Electron accumulation during the imaging process was responsible for the occurrence of these unavoidable cracks.
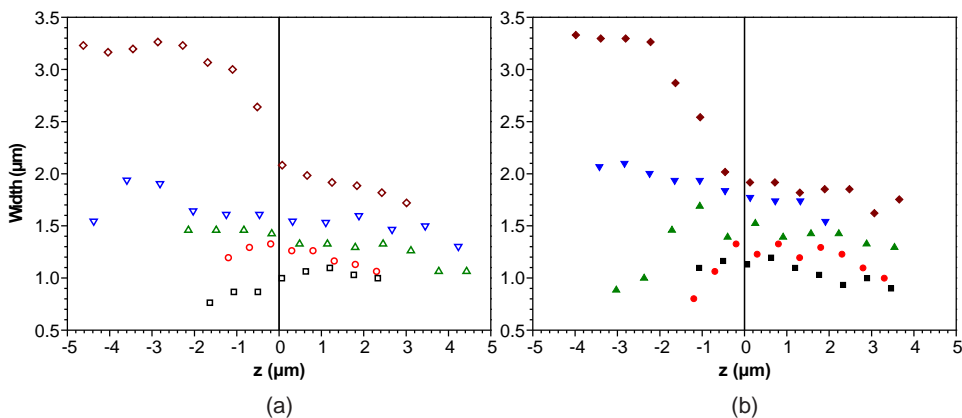
Figure 3.19: Plots of the width measurements of the channels vs z position. The measurements were obtained from SEM images of the sample surface. Colors and shapes of the represented data correspond to [(a), empty symbols] 0.2 μm, and [(b), filled symbols] 0.5 μm of spot separation and (**squares**) 100, (**dots**) 130, (**up triangles**) 150, (**down triangles**) 200, and (**diamonds**) 300 nJ of incident energy. All width and depth measurements have an experimental error of ±0.1 μm.

Measurements done on the SEM images acquired for all the produced lines made possible the study of line width and depth dependence according to the experimental parameters (Figures 3.19 and 3.20). First of all, a general behavior is present in all the cases: the width and depth of the channels have larger values for higher

incident energies. Another general trend for width values (Figure 3.19) is that they do not significantly change at fixed incident energy for different z positions except in the case of 300 nJ, where there is a clear transition between two ranges of z position values. In the first one, which corresponds to the situation where the beam waist is outside the sample, lines about 3.2 µm wide can be obtained. At positions of the second range, the line width is thinner with an average value of 1.8 µm. Apart from this behavior at 300 nJ, the fact that lines show similar widths at fixed energy independently of the z position at which they are fabricated establishes a certain extent in the z position that has a span of 4 µm at 100 nJ and almost 8 µm at 200 nJ for producing lines with similar sizes at the sample surface. Concerning the comparison of the two different values for the separation between spots, lines obtained at 0.2 µm of spot separation are slightly thinner than at 0.5 µm.
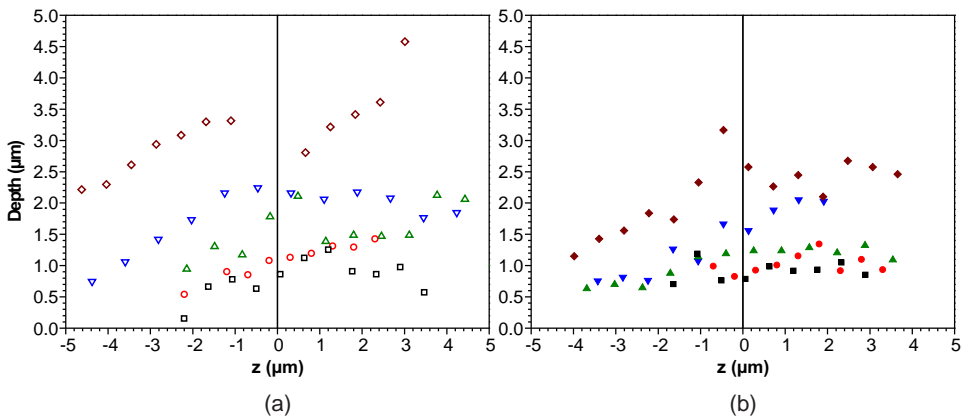
Figure 3.20: Plots of the depth measurements of the channels vs z position. The measurements were obtained from SEM images of the sample cross section. Colors and shapes of the represented data correspond to [(a), empty symbols] 0.2 µm, and [(b), filled symbols] 0.5 µm of spot separation and (**squares**) 100, (**dots**) 130, (**up triangles**) 150, (**down triangles**) 200, and (**diamonds**) 300 nJ of incident energy. All width and depth measurements have an experimental error of ±0.1 µm.

The analysis of the depth data of the lines (Figure 3.20) shows some different behaviors in comparison with the trends of line width. For all the studied incident energies, but especially for 200 nJ and 300 nJ, the depth of the lines tends to increase as the beam waist enters the sample. This satisfies the expected behavior: lines produced when the beam waist is closer to the sample are deeper. However,

this increase of the depth with increasing z position values stabilizes at some point, approximately 1 μm before the beam waist reaches the sample surface (z = -1 μm). This also allows the determination of a certain range of z positions where the depth of the channels shows similar values. Nevertheless this range is not as wide as in the case of the line width because after some point corresponding to higher values of the z position the depth tends to slowly decrease. As an example, this range of lines with similar depths is 4 μm wide at 200 nJ, while lines with similar widths can be obtained in a range of 8 μm at the same incident energy. In the comparison of the two different values for the separation between spots, the lines obtained with a spot separation of 0.2 μm tend to be deeper than in the case of 0.5 μm, particularly for higher incident energies (200 nJ and 300 nJ). The fact that a higher overlap produces deeper channels is in agreement with previous studies [135,136].
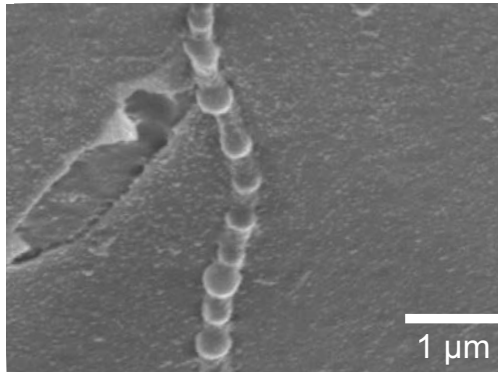
Figure 3.21: SEM image (surface) of a line of bumps obtained at 150 nJ of incident energy, 0.5 μm of spot separation and -3.7 μm for z position.

At some specific experimental conditions, surface swelling in form of bumps with submicrometric dimensions are observed. These conditions correspond to two different cases. In the first case, bumps are observed at low incident energies (up to 150 nJ) and small negative values of z position, this is, when the beam waist is outside the sample. Some of the bumps produced at these conditions had a width of 340±10 nm (Figure 3.21), which is much lower than the laser wavelength value of 1027 nm. No inner modifications, only the presence of bumps is observed. In the second case, bumps also appear at higher incident energies when the beam waist is inside the material but still close to the surface and the internal expansion produces some swelling at the surface in form of bumps. In this case, the expan-

sion is not strong enough to ablate the surface material. This process has been also explained in dynamic simulations corresponding to the thermal processes related to the energy absorption [129]. In agreement with the simulation results, inner modifications are clearly visible under the bumps obtained at these conditions in the second case (Figure 3.17m-n Bottom).

After the analysis of the data of the produced lines, some conclusions on the positioning of the sample to ensure a precise surface modification by line fabrication can be presented. First of all, there is a margin of some microns in the z position around z = 0 μm (beam waist at the material surface) to obtain lines with similar features, particularly for the line width. This range of z positions is the best option for a reliable surface modification with reduced affectation from possible vibrations and position shifts of the setup. Secondly, there are two possibilities for obtaining submicrometric features. These are surface modification in form of bumps (obtained at two different experimental conditions) or the use of low energies close to the ablation threshold to produce lines with the smallest feasible dimensions. This last case presents a smaller variation of width and depth, with width values close to 1 μm and depths around 0.7 μm. Finally, in order to avoid the presence of any kind of inner modifications under the modified surface, recommended positions are when the beam waist is outside the sample surface, shortly before entering it. Hence keeping the sample at a specific z position is essential. This can be achieved by monitoring the sample position through transmittance measurements during line ablation. As a consequence of these results, depending on the preferences for the desired surface modification results, the most suitable position for fabricating lines can be chosen.

3.2. Studies on reflectance measurements at different focusing distances

An improvement to the z-scan focusing method is presented in this section. The incorporation of an additional energy detector in conjunction with an extra beam splitter properly placed in the optical path gave access to measuring the radiation reflected by the sample (see Figure 2.3). In this way, the obtained data from the transmittance measurements is completed by reflectance data. These data were

registered simultaneously to the realization of z-scans, like transmittance data.

Reflectance measurements for each single pulse fired onto pristine material for different z positions are shown in Figure 3.22(a). The plots show a peak for the series of spots produced at 125 nJ and higher incident energies. For z positions where the sample surface is far from the beam waist, a flat tendency of the reflectance was observed as the pulse energy is not absorbed by the PMMA and only the light reflected by the surface (refractive index change) is measured, which for the laser wavelength (1027 nm) corresponds to a reflectance value of 8.6 %. As the sample surface is brought closer to the beam waist, fluence increases and when it overcomes a certain threshold value, absorption of the laser radiation starts taking place. At this point, transmittance starts decreasing and reflectance starts increasing. Reflectance continues increasing as the surface gets closer to the beam waist position until it reaches its maximum value around the position z = 0 μm. Then, the reflectance starts decreasing as the fluence at the surface gets lower and higher fluences are inside the bulk. Finally, when the beam waist is deep inside the bulk, the reflectance recovers the original value.

These observed tendencies for reflectance measurements can be contrasted with transmittance measurements that were simultaneously taken. These values are represented in Figure 3.22(b) in the same way as reflectance measurements were plotted in Figure 3.22(a). As it has been observed and explained in the section 3.1 of this chapter, the transmittance decrease observed as the sample enters the beam waist can be used to monitor the relative position between the sample surface and the beam waist and makes possible to ensure a good position control during the experiments. It also makes possible determining the beam waist position z = 0 μm and therefore correct the z position values for the experimental data. The correction is based on the fact that at z = 0 μm, the corresponding transmittance value is found approximately at an 83 % decrease of the total transmittance difference between the transmittance value where no absorption is detected (91.4 %) and the bulk transmittance value for the corresponding incident energy. This correction makes that the z position of the reflectance peak is found close to the value corresponding to the sample surface laying at the beam waist position. This also means that performing reflectance measurements is a good way to determine the beam waist position at incident energies above a certain threshold for the peak presence, because the detection of a maximum is enough. For this reason, the beam waist po-
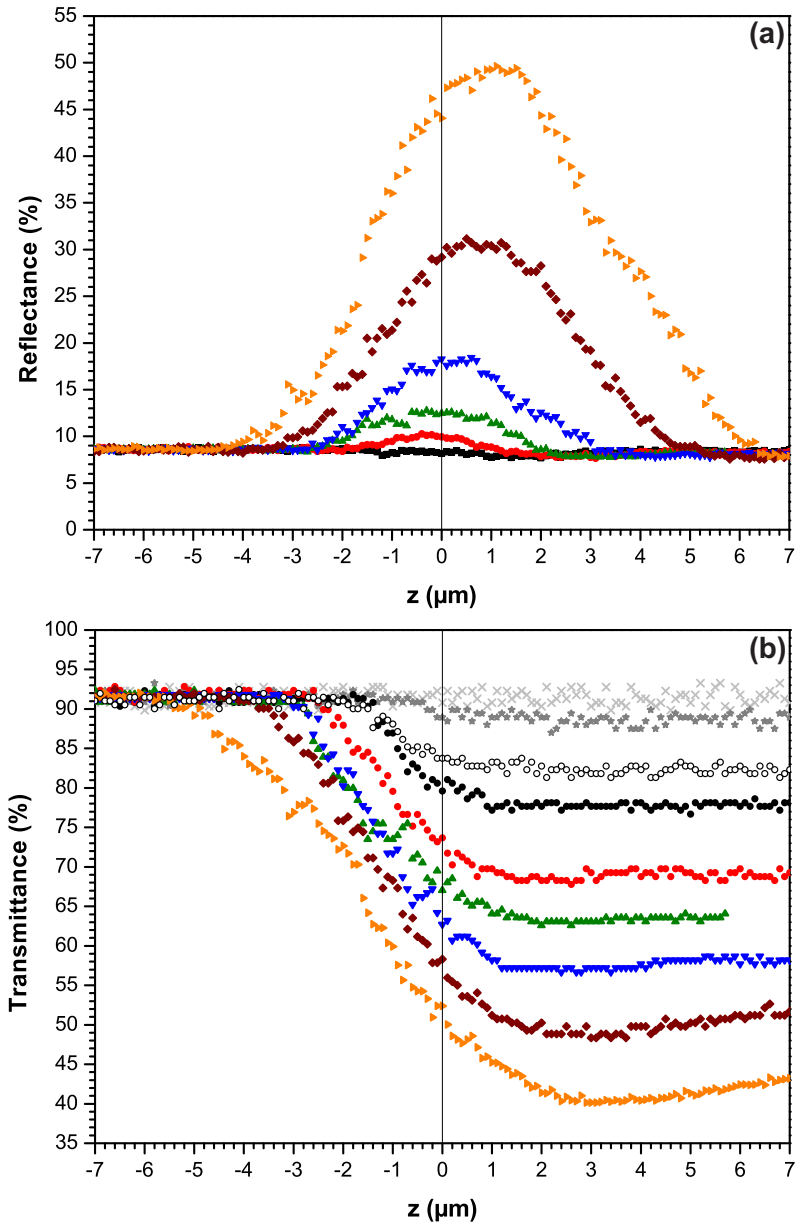
Figure 3.22: (a) Plot of reflectance vs. z position at (**squares**) 100, (**dots**) 125, (**up triangles**) 150, (**down triangles**) 200, (**diamonds**) 300, and (**right triangles**) 500 nJ of incident energy. The experimental error for the reflectance data is ±0.3 %. (b) Plot of transmittance vs. z position at (crosses) 50, (**stars**) 80, (empty circles) 90 nJ, and same incident energies as in (a). Transmittance data have an experimental error of ±3 %.

sition determination by reflectance measurements is much easier than when done by monitoring transmittance data.
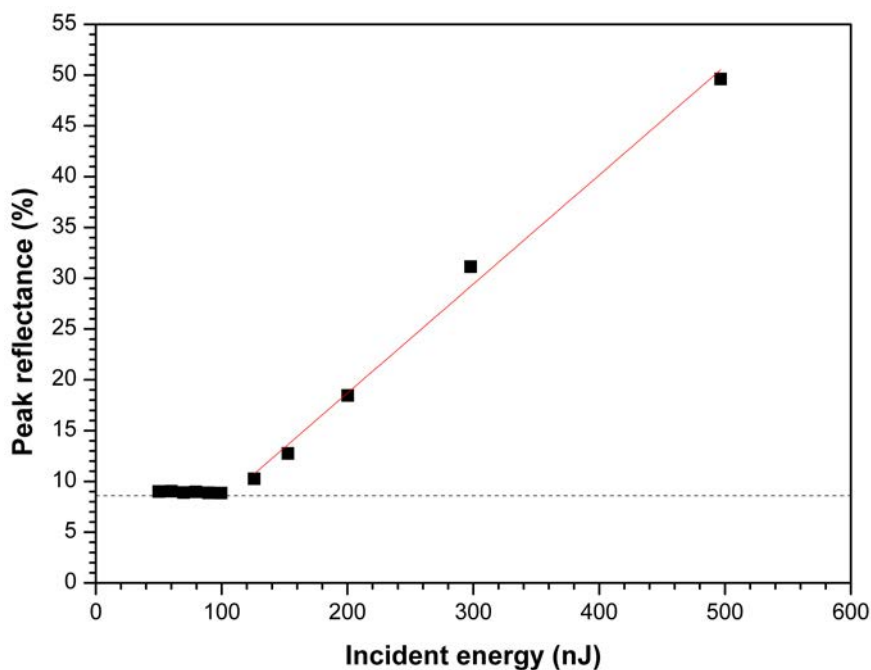
Figure 3.23: Peak reflectance values for the different studied incident energies. The fitted line describes the linear tendency that these values follow in the range of energies between 125 nJ and 500 nJ. The experimental error for the peak reflectance values is ±0.3 %.

The reflectance peak tends to shift slightly for increasing incident energies to z positions where the beam waist is below the sample surface. At the same time, the peak width and height also increase while going to higher incident energy values. This tendency of the peak height can be observed in Figure 3.23. It can be seen that the peak maximum value increases linearly with increasing incident energies. This behavior makes possible to find a threshold energy value that has to be overcome to start observing a peak in the reflectance. This value can be found when the line fitted to the data meets the reflectance value of 8.6 % corresponding to the usual reflectance of the PMMA for light at 1027 nm. This energy value is 106 nJ. Experimental results agree to this value, as no peak could be observed for energies lower than 125 nJ. The presence of this threshold for the observation of a reflectance

peak could be related to the formation of a plasma at the sample surface. In view that ablation is always observed when reflectance is higher than 8.6 %, it can be assumed that an electron-ion gas-like plasma is generated as indicated in previous simulations of the process of PMMA ablation [118, 129]. The increase of the reflectance is directly related to the increase of the plasma density.
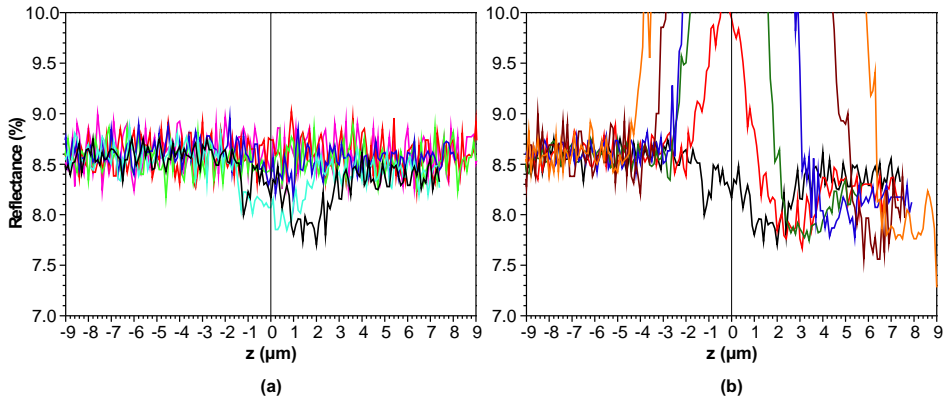
Figure 3.24: Plot of reflectance vs. z position for incident energies of the pulse between (a) 50 and 100 nJ, and (b) 100 and 500 nJ. For lines in (a), the energy values are (**magenta**) 50, (**red**) 60, (**green**) 70, (**blue**) 80, (**cyan**) 90, and (**black**) 100 nJ. For (b), the line colors correspond to the following energies: (**black**) 100, (**red**) 130, (**green**) 150, (**blue**) 200, (**brown**) 300 nJ, and (**orange**) 500 nJ. The lines only link data points (separated by 0.1 μm) to make easier following the data tendency. Experimental error for all reflectance data is ±0.3 %.

A more detailed observation of the reflectance values for 90 and 100 nJ (below the threshold for peak observation) reveals a small reflectance decrease in form of a valley (Figure 3.24a). The position of the valley is found around the beam waist (z = 0 μm) but also slightly shifted to z positions corresponding to the beam waist being below the surface. For energies higher than the peak observation threshold (see Figure 3.24b), the reflectance decrease (valley) is still present following the peak. Nevertheless, the reflectance minimum does not seem to change much for the different studied incident energies. On the other hand, after the peak and the valley, the reflectance value follows again a flat tendency corresponding to the situation when the beam waist is inside the bulk. All these phenomena can be interpreted according to previous studies on some semiconductors like silicon, where the evolution of the reflectance behavior is studied with respect to the ex-

cited electron-hole density at the material surface [137, 138]. According to these papers, the density of the plasma created on the surface by the impinging laser pulse modifies the optical response of the material. This effect can be explained by the Drude model, which is characterized by a decrease of the reflectivity at lower densities and a drastic increase at higher densities.

3.3. Comparison between transmittance and reflectance results

When comparing reflectance and transmittance measurements, it can be observed that they point out the close presence of the sample surface with respect to the beam waist in a similar way (Figure 3.25): the reflectance peak starts at the same position as the transmittance drop begins. However, the end of the reflectance peak is found at higher values for the z position than the end of the transmittance drop. The later end of the reflectance peak can be used to monitor the z positions where spots are still produced but the transmittance has already reached the bulk flat value (red shaded area in Figure 3.25). This figure shows the range of positions where changes in the transmittance and the reflectance measurements are detected. Note that for this incident energy, the transmittance changes are detected in a range of z positions of about 4 μm, while reflectance range is of about 6 μm.

The increase in the accuracy for placing the sample given by reflectance data is more evident when it is desired to perform ablation experiments when the sample is placed in the down part of the transmittance curve (see Figure 2.9). The reflectance measurements allow placing the sample in those positions since changes in the reflectance can still be detected, increasing the range where positioning can be executed in a controlled way (red shaded area).

In addition, Figure 3.26 shows the width of the range where the z position of the surface can be determined by reflectance or transmittance measurements for different incident energy values. The values were obtained by measuring the width of the transmittance drop and the width of the basis of the reflectance peak (shaded ranges in Figure 3.25). The results show that for the studied incident energies, both measurements give comparable margins for the sample surface position determi-
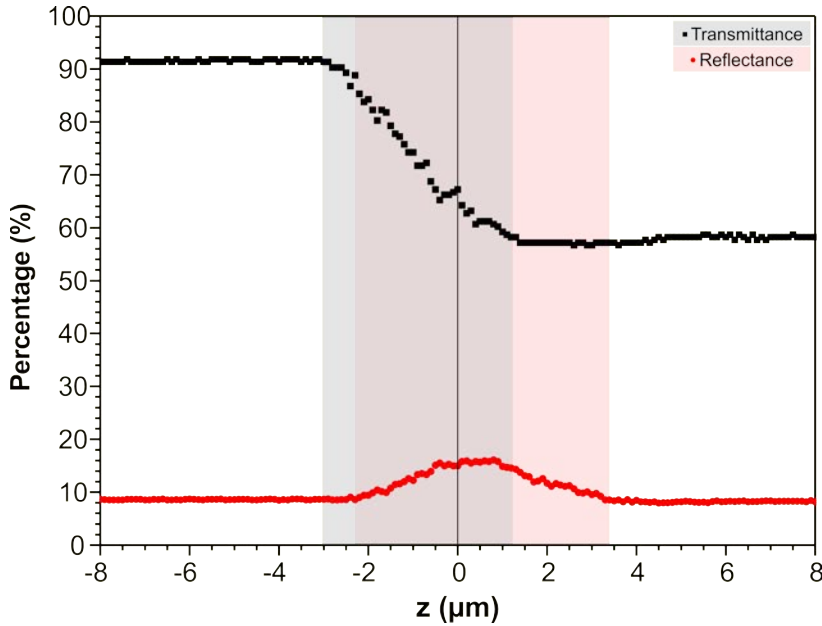
Figure 3.25: Plot of the transmittance and the reflectance of PMMA during a z-scan experiment. The incident laser energy was 200 nJ.

nation and, therefore, can be used similarly as position control methods. Nevertheless, it has to be noted that transmittance measurements can go down to incident energies close to the ablation threshold, while changes in the reflectance can only be detected at higher energies in the used experimental setup.

In this way, both reflectance and transmittance data can be put to work to correct the sample surface alignment with respect to the beam incident direction. Any change in the values would detect a tilt of the sample surface. Transmittance measurements provide an easier way for correcting this tilt considering that the sign of the change of the measured transmittance gives the direction for the correction of the sample tilt: a lower transmittance value indicates that the sample surface is going inside the beam waist. On the contrary, reflectance measurements require more steps for doing this correction because the peak behavior of the data does not give directly the direction needed for the tilt correction (see Figure 3.22): a decrease at the left of the reflectance peak means the sample surface going further from the beam waist while at the right of the peak, it means just the contrary. In this case, additional measurements are necessary for being able to correct the sam-
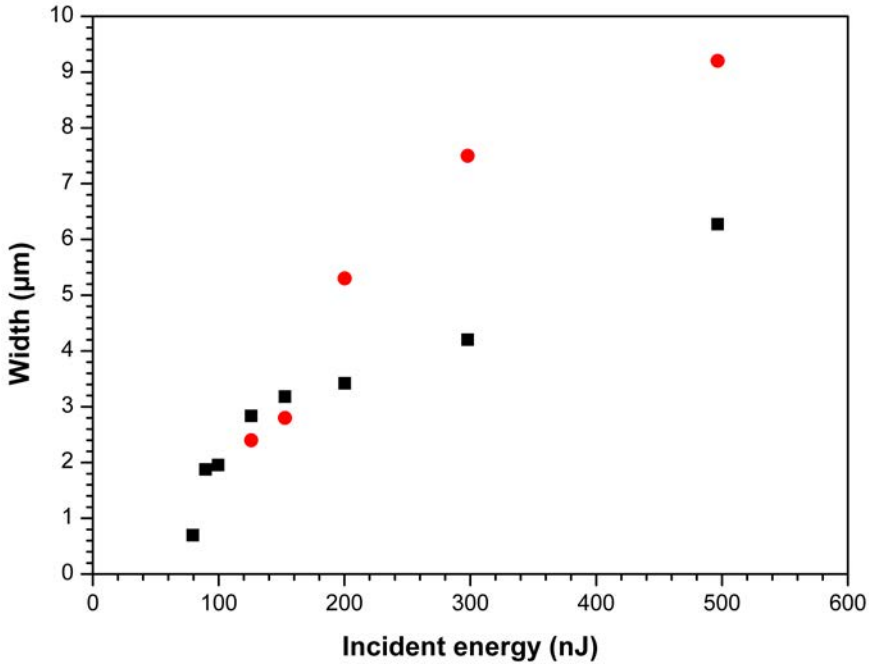
Figure 3.26: Plots of the width of the z position range where the sample surface can be detected by the two presented options: reflectance and transmittance measurements. Width values are plotted vs. the incident energy of the laser pulses. **Squares** correspond to transmittance measurements (width of the range of the transmittance drop, experimental error ±0.2 μm) and **dots** show the width of the reflectance peaks measured at their basis, with an experimental error of ±0.3 μm for all the values.

ple tilt.

In order to evaluate the precision of the positioning method through transmittance measurements, the slope of the transmittance drop in the z-scans was analyzed. This slope was calculated by fitting a line to the experimental data. The tendency that these values follow has been represented in Figure 3.27. For incident energies close to the ablation threshold, the slope rapidly increases until 200 nJ. The higher the value of the transmittance drop slope, the higher the sensitivity to detect a change in the z position. Therefore, the control of the z position with transmittance measurements presents the best precision for incident energies around 200 nJ. For higher energies, the method still has a good performance as a position control procedure since the slope value only decreases a little. If 8.5 %/μm
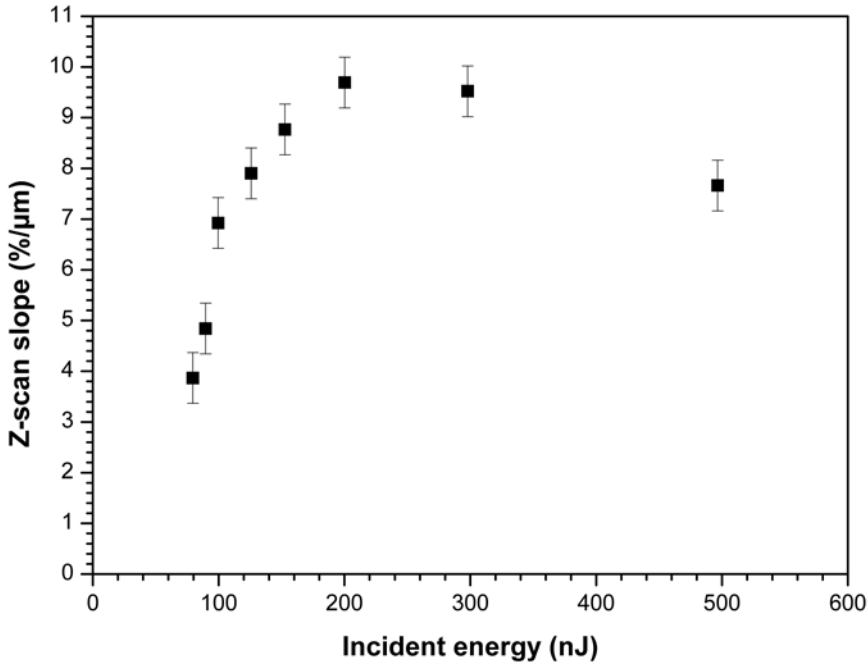
Figure 3.27: Plot of the z-scan slope (transmittance decrease rate) for the different studied values of the incident energy of the pulses. This decrease rate corresponds to the transmittance reduction observed when the sample enters the beam waist region. The experimental error of the plotted slope values is ±0.5 %/μm.

is taken as an average value for the slope at these energies (100 nJ to 500 nJ), the 5 % margin for the surface horizontality in transmittance values commented in the experimental section gives a precision in the determination of the z position of 0.6 μm. This number can be considered a good representative value for the precision of the z-scan method as a position determination procedure.

However, for energies very close to the ablation threshold, which are used to produce very small spots, transmittance measurements cannot ensure such a good position control. In this situation, only a reduced range of z positions where fluence overcomes the ablation threshold is suitable for spot production and the relative position of the sample surface with respect to the beam waist becomes more critical. However, small spots can be produced also at higher energies. Spots shown in Figure 3.28 were obtained at the two first positions where a transmittance decrease is detected. Their dimensions are visibly smaller than the diffraction limit
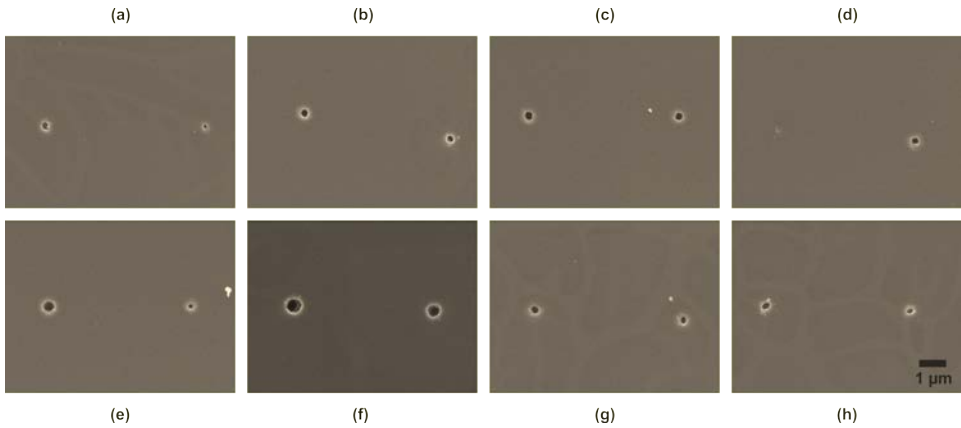
Figure 3.28: SEM images of the first two craters produced each one by one pulse with the same incident energy when the sample is entering the beam waist region and the fluence at the surface overcomes the threshold value. The right crater is the first one, while the left crater is produced when the sample surface is 0.1 μm closer to the beam waist. The images correspond to different incident energy values: (a) 80, (b) 90, (c) 100, (d) 125, (e) 150, (f) 200, (g) 300, and (h) 500 nJ.

of the focused laser beam. There is a change in the z position of 0.1 μm between the two spots visible at each image and the incident energy values at which they were produced go from 80 nJ (just above the ablation threshold) until 500 nJ. The radii of these spots are in the range between 66 nm for the smallest one (obtained at 80 nJ) and 340 nm for the largest one (obtained at 200 nJ). Even with 500 nJ of incident energy, spots with radii below 300 nm were obtained. These dimensions are well below the Airy disk for the focusing objective at the laser wavelength.

The obtained results certainly show that in situ reflectance or transmittance measurements during the surface modification process make possible a high precision position control of the sample surface with respect to the beam waist and, consequently, a good control of the dimensions of the produced surface modifications. Likewise, this optimization of the surface modification procedure contributed to the surface ablation of spots with sizes in the submicrometric domain without being restricted only to incident energies very close to the ablation threshold. Precise surface ablation is also possible with pulse energies clearly higher than the ablation threshold.

4 Applications in laser microprocessing of materials

This chapter collects some of the most relevant results obtained in laser microprocessing of diverse materials with applications in various fields. The chapter is divided in four sections, one for each of the fields corresponding to possible studied applications of the obtained results. Different materials suited for the proposed applications were processed during the studies presented below. Relevant data about them can be found in this chapter together with information already given in chapter 2.

The first three sections of the chapter contain some interesting preliminary results on the studied topics, according to their more moderate position among the scope of the research group. The forth section presents a more detailed study owing to the more relevant connections of the treated topic with the research projects in effect during the period of time this thesis was under development.

4.1. Laser irradiation of biodegradable polymers

The interest on biodegradable polymers is gaining more importance every day because of the ease of disposal of these materials, which makes them a very attractive alternative as a solution to the aggravating problem of the plastic waste management, and their manifold applications in the field of biological and medical studies, where these polymers can be processed and tailored to reproduce and improve biological processes spontaneously happening. The results exposed in this section include femtosecond laser processing of two biodegradable polymers, PLA and PLGA, with different objectives but with a common goal: the improvement of the functionalities of both materials owing to the versatility that laser processing can offer.

4.1.1.   Profound hole ablation in PLA

Polylactic acid (PLA) is a material of interest as an alternative to nondegradable polymers for manifold applications, particularly in the field of disposable medical consumables thanks to its natural biocompatibility. Other fields where PLA is being studied and implemented as a feasible choice include tissue engineering, medical implants, surgical sutures, packages, fibers, and textiles. For instance, sustainable approaches using PLA to reduce plastic waste are becoming a reality [139]. Their goal is addressing the worldwide growing concern around increasing pollution from plastic waste. For these reasons, femtosecond laser ablation in PLA is studied in this part of the thesis as a tool for efficiently processing this material with micrometric precision for future possible applications in the fields of microfluidics and lab-on-a-chip (LOC) devices with a sustainable and environmental-friendly add-on.

Studies on PLA surface ablation by femtosecond laser presented in this subsection were focused into production of holes at the material surface. Experiments consisted in accumulation of laser pulses focused though the $5\times$ microscope objective on the surface of PLA samples at a repetition rate of 1 kHz. Different number of pulses were accumulated at each spot on the material surface at a fixed energy and focusing distance. In order to ensure a good alignment of the sample surface and positioning of the laser beam waist with respect to the sample surface, the z-scan method was implemented. The z position of the sample surface was chosen to be at the laser beam waist for all the experiments in PLA.

Scanning electron microscopy (SEM) images of the produced hole evolution for an increasing number of accumulated laser pulses can be observed in Figure 4.1. This succession of images starts with Figure 4.1a, where the surface modification produced by one single laser pulse can be seen. The ablated spot showed a broken dome-shaped and porous structure, probably originated by an absorption of the laser pulse just below the surfaced followed by an expansion of a generated bubble of the material that bursted and resulted in the remaining shape, similarly to results observed on PMMA surface ablation [129], but with a more violent burst of the dome in the case of PLA. In PMMA, this shape was presented as a result of surface swelling, which was considered a first step in femtosecond laser ablation for laser fluences close to the material laser absorption threshold. Baset et al. also observed the presence of radial ejected patterns surrounding the edges of the ab-

lated spot together with nanodroplets, which indicated that the ablation process took place through a molten phase of the material. Fragments of the ablated material resolidified probably because of rapid cooling during expansion and remained attached around the ablated spot. These ejected material remains were observed in the presented results on PLA in different grades for all the ablated spots, what suggests that ablation was achieved through a melting phase of the material as well.

Figure 4.1b showed the result of surface ablation when two pulses temporally spaced by 1 ms were accumulated onto the same sample spot. It can be clearly seen that in this situation, the previous broken dome-like structure completely disappeared and led to the formation of a porous crater, only by the accumulation of one additional pulse. Following images (Figures 4.1c-f) show a similar crater shape, but getting a little bit larger and significantly deeper as more laser pulses are accumulated. At some point the crater bottom became not visible anymore and thus, it was decided that in order to gain information about the hole walls, the sample should be tilted.

A transition in the hole edges definition and wall roughness can be observed between holes (g) and (h) in Figure 4.1, produced by 400 and 600 laser pulses, respectively. It can be observed how the hole walls started becoming visibly smoother, while the hole size seemed to remain quite stable for the rest of the following holes (Figures 4.1h-j) together with an improving definition of the hole edges. At the same time, rugosity of the hole walls disappeared almost completely when 1000 laser pulses were sent onto a fixed spot (Figure 4.1i). Finally, rugosity of the hole walls virtually faded and outstanding definition of the hole contour was achieved when 10000 laser pulses were accumulated during 10 seconds at the same position on the sample (Figure 4.1j).

After a first inspection of the hole aspect evolution, hole radii were measured on the SEM images, taking the longest semiaxis value for tilted images. The measured values are represented in Figure 4.2 and correspond to black squares data. The trend followed by these data showed a steady increase in the radii from 4.7 μm for one single laser pulse up to a maximum radius reached for 600 accumulated laser pulses. From this value on, hole radii seem to stabilize at value of 7.8 μm for an increasing number of accumulated pulses. This behavior suggested that something
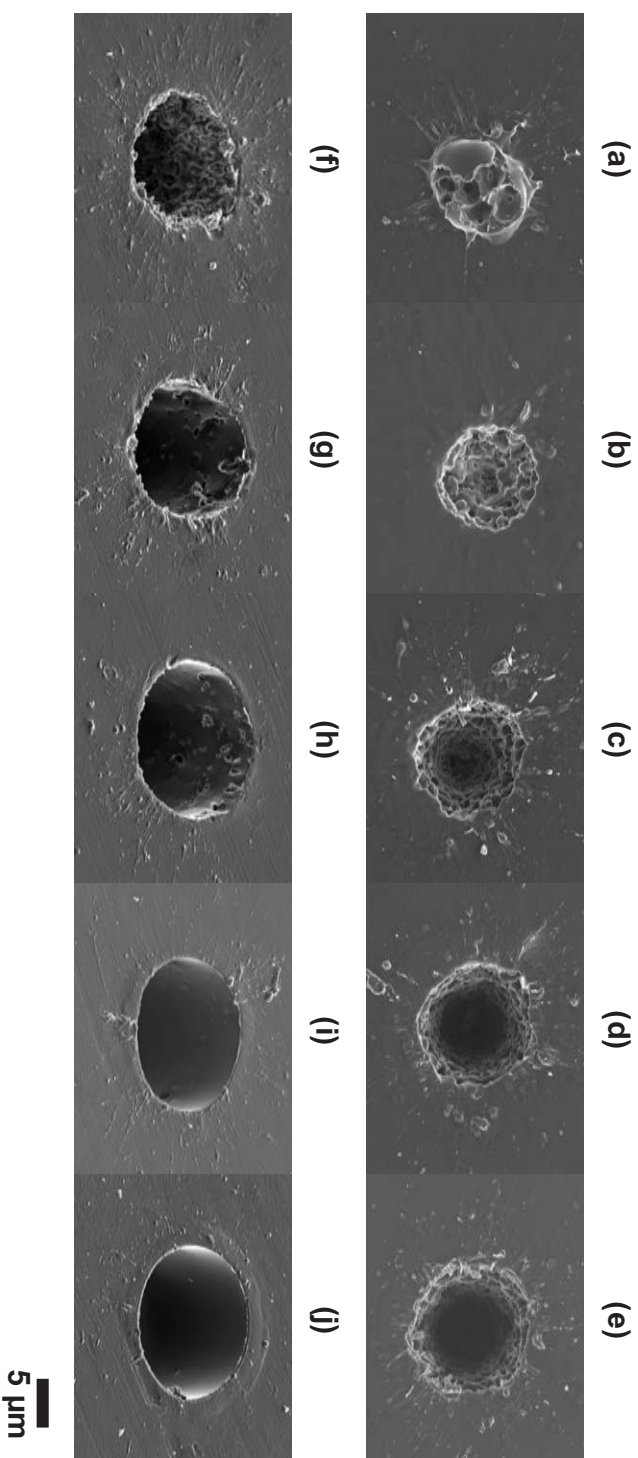
Figure 4.1: SEM images of the PLA surface after the incidence at a fixed spot on the sample of (a) 1, (b) 2, (c) 5, (d) 10, (e) 100, (f) 200, (g) 400, (h) 600, (i) 1000, and (j) 10000 laser pulses of 7.4 μJ. Images (a)-(e) correspond to a top view of the corresponding holes, while images (f)-(j) were taken with a sample tilt of 45°.

was happening when a certain number of accumulated laser pulses was reached. In order to get more information about these conditions, the sample cross section was imaged by optical microscopy. For that, the lateral surface (sample plane perpendicular to the surface where holes were ablated) was meticulously polished in order to get close to the produced holes.
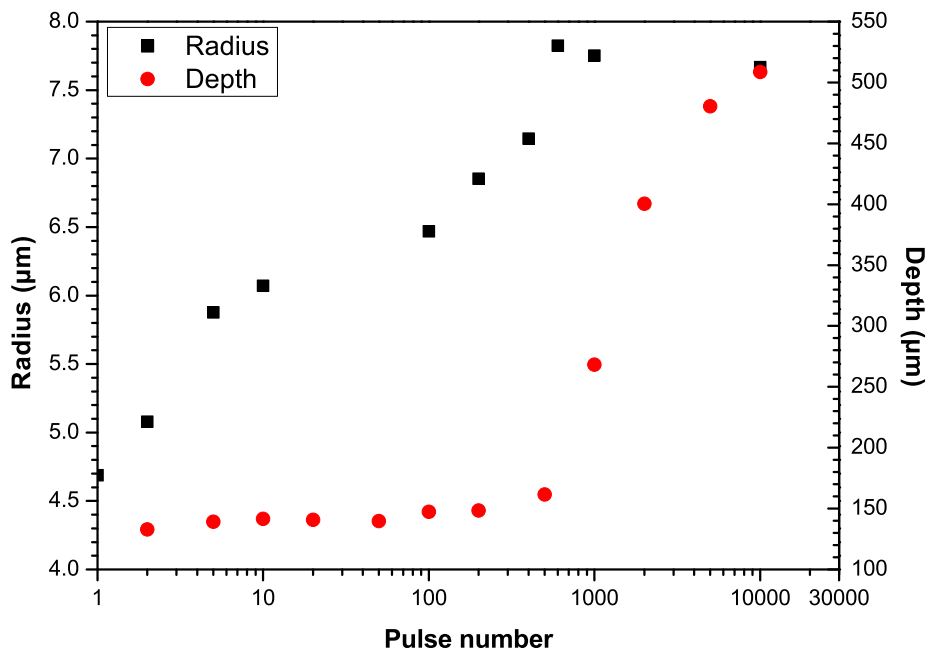
Figure 4.2: Semilogarithmic plot of the measured radii (**black squares**, left vertical axis values) in the SEM images in Figure 4.1 and measured depths (**red dots**, right vertical axis values) in the optical microcopy cross section images in Figure 4.3 according to the accumulated laser pulse number.

The observed cross sections of the holes showed astonishing results. These can be observed in the optical microscopy image of Figure 4.3. The evolution of the hole cross section for an increasing number of accumulated pulses showed a very clear differentiation in two groups. The first one includes holes produced by accumulation of 2 pulses up to 200 pulses (Figure 4.3a-g). These holes show a superficial crater (corresponding to holes observed in Figures 4.1a-g) that rapidly narrows and converts into a thin filament that reaches a constant depth for all these holes produced by increasing numbers of accumulated pulses. It can be also

observed that the superficial crater depth timidly increases. But it is not until a certain number of pulses is reached that the hole depth becomes suddenly larger. This started happening for 500 accumulated laser pulses, which is the initial value for the second group of holes and was observed until the final value of 10000 pulses. This second group is characterized by deep holes that show a constant width with straight walls going downwards from the surface until the tip of the hole is reached. No presence of filaments remained in any case of this group.
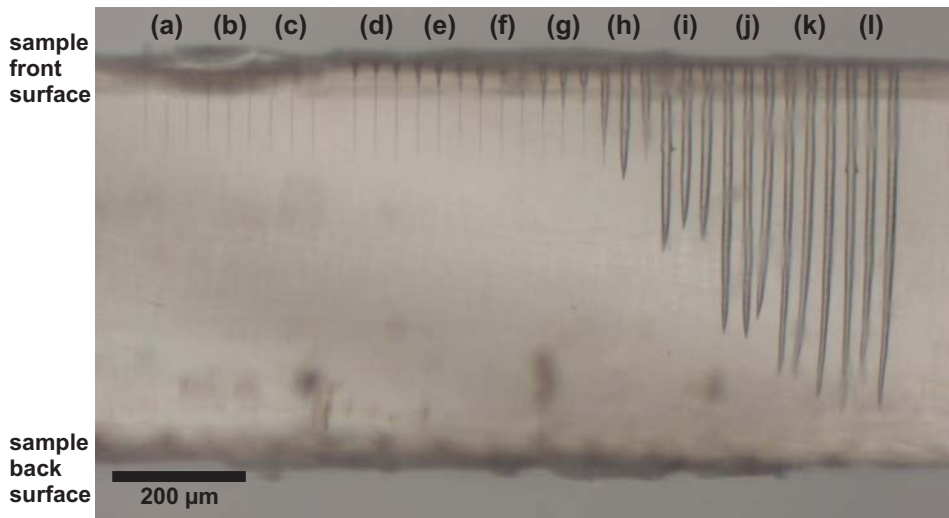
Figure 4.3: Optical microscopy image of the PLA cross section after the incidence at a fixed spot on the sample of (a) 2, (b) 5, (c) 10 (d) 20, (e) 50, (f) 100, (g) 200, (h) 500, (i) 1000, (j) 2000, (k) 5000, and (l) 10000 laser pulses of 7.4 µJ. The holes appear in groups of 3 holes produced with the same incident pulse number.

Depth values of the holes were measured in Figure 4.3 along a vertical line from the sample front surface down to the tip of the observed material modification (either filament end or hole tip). These measured values were plotted in Figure 4.2, where they correspond to red dots. Each data point was calculated as the average value for the three holes produced at the same number of accumulated pulses. Similarly to what could be observed for measured radii, there is a change in the tendency of the values starting from 500 accumulated pulses until the final value of 10000 pulses. This circumstance coincides with the commented transition between 400 and 600 pulses observed in the surface images (Figure 4.1) and

measured radii, and in this case it is signaled by a sudden increase of the depth of the holes. This depth growth shows a steep increase until it relaxes and seems to reach a stable maximum depth value similar to the last value at 10000 pulses. This saturation of the hole depth for a continuously increasing number of accumulated pulses was observed in previous studies dealing with other materials like silicon [140] and chemical vapor deposition (CVD) diamond [141]. It has to be highlighted that holes produced by 10000 pulse accumulation reached depths close to the sample back surface, almost completely going through the total thickness of the sample. If this situation of depth saturation should be overcome for the manufacturing of through-holes that completely perforate the sample, a first strategy would consist in increasing the laser pulse incident energy. On the other hand, a solution that could become handy when laser pulse energy cannot be further increased has been proposed in similar experiments on PMMA in reference [142]. The implementation in the experimental setup of a rough vacuum environment where the sample ablation process took place facilitated the ablated material removal. As a consequence, the maximum depth reached by pulse accumulation gradually increased as the ambient pressure decreased.

Another feature that stood out from the group of fabricated deep holes in Figure 4.3 was the remarkable bent that was present in almost all the holes. The bending showed different degrees of intensity, but the deviation seemed to point at the same direction for all the holes. This characteristic of holes produced by laser percussion drilling have been observed in similar experiments carried out on different materials [141–143]. Because of the bending, hole quality is detrimentally affected. The impact of this effect in the control of the hole production is quite critical and can entail serious problems in the manufacturing of through-holes, especially in the case of microholes arrays, where the uncontrolled exit of the hole through the material back surface becomes seriously problematic.

In the same way as it is explained in paper [142], the hole bending was observed only at the deepest part of the hole, close to its tip. For this reason, this situation might be related to effects that could disturb the laser propagation during the hole formation, leading to anisotropic interactions particularly at the bottom of the holes. At the beginning of the hole ablation, the energy of the laser pulses reaching the transitory hole bottom is enough to propagate along the hole without any significant distortion. A straight profile of the hole walls is achieved in this situa-

tion. However, as laser pulses propagate deeper inside the already produced hole, a longer propagation path inside the hole must be travelled by the incoming laser pulses. This longer path means a larger volume where the incident laser radiation may interact with the ablation debris products. This produces a decrease in the laser energy reaching the hole bottom, which translates into possible disturbances in the propagating radiation becoming not negligible anymore and producing notable alterations of the laser beam. Moreover, a deeper position in the sample also implies a more defocused laser beam, since its beam waist is located close to the sample surface. Consequently and according to results of experiments carried out on PMMA samples of reference [142], hole bending could be ascribed to distortions of the incoming laser pulses due to interaction of the laser radiation with the expanding ablation byproducts and debris.

The same ambient pressure reduction solution commented before and proposed in reference [142] was practical for the elimination of hole bending. Again, the elimination of the bending is attributed to the evacuation of dynamic aerosol which could disturb the laser propagation reaching the end of the hole drilling process. Another proposed strategy consisted in lowering the repetition rate of the laser pulses to let the ablated material and debris evacuate the hole. Intervals between consecutive laser pulses longer than 20 ms were found sufficient to eliminate any sign of bending of the holes. This value gave a reference for the time duration of the processes leading to the bending of the holes, and corresponded to the visualized timescale of the vapor cloud expansion and ablated material ejection during the experiments in the referred paper. Therefore, both processes were suspected to be the main disturbance factors responsible for hole bending. The suppression of the bending effect through these two strategies proved that interaction of the incident laser pulses with the expanding ablation byproducts was the main distortion origin leading to bending.

Further analysis of the optical microscopy images of the sample cross section showed that deeper inside the material, z-scans done previously to hole ablation experiments could be identified when farther cross section focal planes were visualized (Figure 4.4). In this image, the aspect of single laser pulses fired at different focusing distances between the laser beam waist and the sample surface along the z axis can be observed. It is noteworthy that the produced material modification by a single laser pulse has the form of a thin filament which elongates in average along
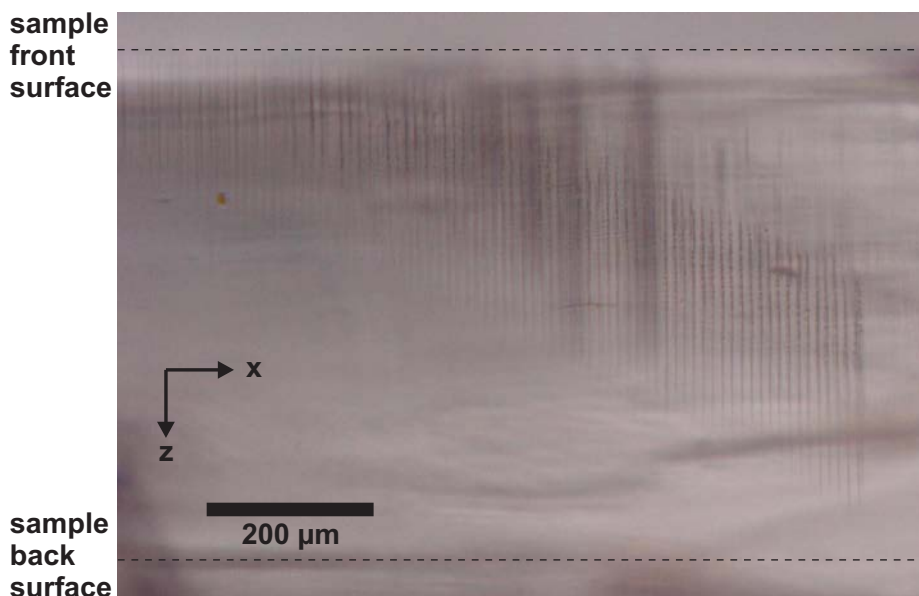
Figure 4.4: Optical microscopy image of the PLA cross section focused at the plane where a z-scan was performed (incidence of a single laser pulse focused at different z distances between the laser beam waist and the sample surface). The calculated Rayleigh length for the 5× 0.13 NA microscopy objective and laser wavelength gave a value of 19.3 μm, which is significantly shorter than the observable filaments produced at each spot for different focusing positions.

approximately 265 μm, a distance much longer than the calculated Rayleigh length for the focusing experimental conditions, corresponding to a value of 19.3 μm, and giving a confocal parameter of almost 40 μm for the beam waist region extension, still shorter than the filament length. Similar filaments observed in other single laser pulse experiments on poly-L-lactide (PLLA) shown in reference [144]) also had an average length of 270 μm. The origin of the filaments was ascribed to self-focusing inside PLLA. This nonlinear optical process could be the reason in PLA accounting for the obtention of deep holes with depths much longer than the beam waist extension. In addition to that, self-focusing occurring during propagation of the laser pulses in the air inside the hole being produced is given as another reason for the increased depth of the holes and their bending according to [143].

These filaments observed in PLA could be compared to previous filaments visible below the obtained craters in PMMA surface ablation presented in subsection 3.1.2.

The porous filament structures in Figure 3.14 might be also present in filamentation in PLA, seen in Figure 4.4 as the granulated morphology that can be identified at the beginning of the filaments (top tip closer to the sample front surface).

In conclusion, laser ablation of PLA through laser pulse accumulation for profound hole production has showed remarkable results consisting in the possibility of obtention of very well defined and smooth holes as well as promising feasibility for complete perforation of the samples thanks to self-focusing of the propagating laser pulses, but keeping in mind possible detrimental effects that might appear and that should be carefully anticipated and overcome for the obtention of satisfactory results.

4.1.2.   Influence of laser irradiation in biodegradability of PLGA

The results presented in this subsection were obtained in experiments carried out during the research stay conducted at Professor Mitsuhiro Terakawa's research group at the Department of Electronics and Electrical Engineering at Keio University, Yokohama, Japan. According to the limited time duration of the research stay, the experiments presented in this subsection show preliminary results on the influence of single pulse laser irradiation at different light wavelengths on biodegradability of polylactic-co-glycolic acid (PLGA).

The interest in controlling the biological degradation of biodegradable polymers is motivated by their manifold authorized clinical uses in biomedical applications like drug delivery and tissue scaffolding. Having the ability of controlling their biodegradation rate makes possible adjusting this process to naturally occurring biological cycles to improve the efficiency and compatibility in the multiple uses of these materials. In addition, PLGA shows a faster biodegradation behavior when compared to other biodegradable polymers like PLA. This feature eases the execution of biodegradation studies, done through immersion of the PLGA samples in a phosphate-buffered saline (PBS) solution.

Previous studies about biodegradation of PLGA have already shown the possibility of altering the degradation evolution of PLGA samples when they are irradiated by laser under some different conditions of laser wavelength and pulse time duration [145, 146]. In continuation with this line of experiments and in order to

get further results and information about this topic, PLGA samples were irradiated with femtosecond laser pulses at three different wavelengths: infrared (800 nm), green (400 nm) and ultraviolet (266 nm). One single laser pulse was fired for each irradiated spot on the PLGA sample. Series of five spots were irradiated for each value of the incident laser pulse fluence. Different values of the laser pulse incident fluence were examined with regard to the maximum fluence supplied by the laser according to the used wavelength. The focusing distance between the focal lens and the sample surface was kept constant for all the experiments and adjusted so that the laser beam size onto the sample had an approximate diameter of 100 μm, with the beam focus located before reaching the sample surface (see Figure 2.5). This slightly defocused spot was used in order to irradiate a certain region of the sample surface and not concentrate the laser light on a tight spot. The main goal in these experiments was not accurate irradiation of the sample surface for precise microprocessing, but irradiation of a certain polymer area for a study of the effect of laser irradiation on the biodegradation behavior of the treated area of the polymer.

The aspect of some selected irradiated spots can be observed in Figure 4.5(i), which contains optical images of the spots just after laser irradiation. Owing to the different absorption fluence thresholds of the material according to laser wavelength and the different incident fluences of the laser pulses, the produced spots show clearly varying dimensions. Their shapes also show noticeable differences that can be attributed to the changing profiles of the laser beam for the different wavelengths, despite the multiple experimental adjustments implemented to minimize these variations. Despite that, the evolution of the degradation at the irradiated spots could be studied.

Figure 4.5(ii) and (iii) show the same irradiated spots on the PLGA surface as in row (i), but after three and seven days of immersion in the PBS solution kept at a constant temperature of 37 °C. In that way, it can be seen how the degradation of the polymer surface developed according to the different irradiation conditions. For the case of Figure 4.5(a) at 25.0 J/cm^2 and 800 nm, after three days the degradation of the irradiated spot seems to have an effect on the dispersion of the light at the spot, suggesting a change of the surface morphology. But it is not until seven days have passed that the degraded area appears significantly larger than the original visible spot, thus implying a gradual increase of the degraded area. The next
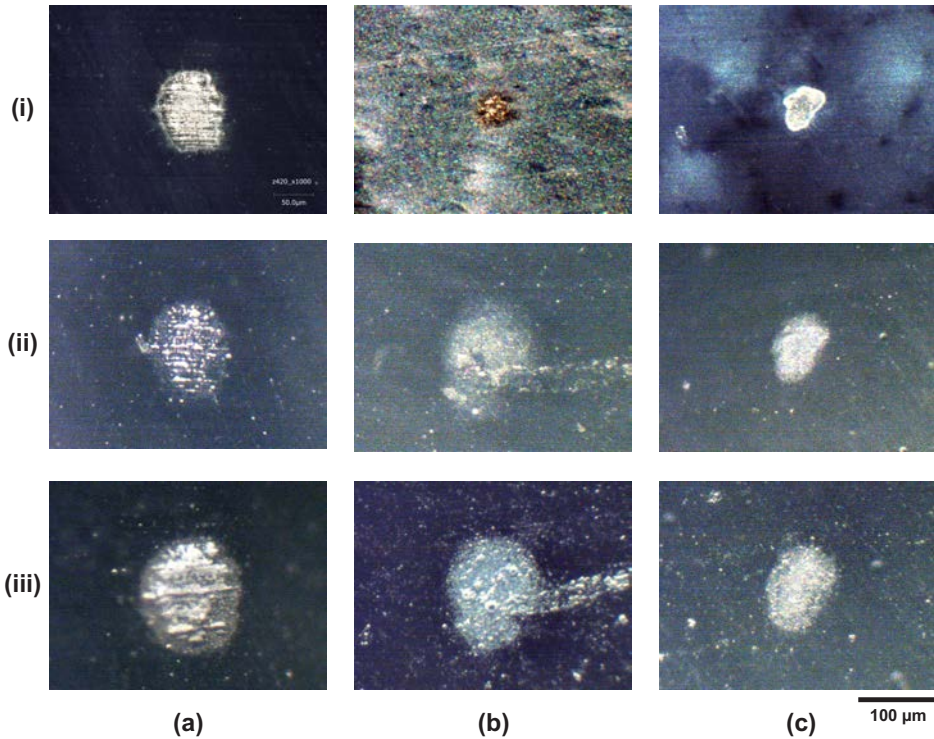
Figure 4.5: Optical microscopy images of the biodegradation process evolution of selected spots produced by single pulse laser irradiation of PLGA at an incident laser pulse fluence and wavelength values of (a) 25.0 J/cm^2 and 800 nm, (b) 1.0 J/cm^2 and 400 nm, (c) 0.3 J/cm^2 and 266 nm. The spots correspond to different stages in the biodegradation process: (i) immediately after laser irradiation, (ii) after 3 days of immersion in PBS, and (iii) after 7 days of immersion in PBS.

case, Figure 4.5(b), shows the biodegradation of a spot produced at 1.0 J/cm^2 and laser wavelength of 400 nm. The visible spot after laser irradiation is clearly smaller than the previous case, but surprisingly the degraded area after 3 days (4.5(ii,b)) shows a very fast degradation rate and appears even larger than case (ii, a). There is also an obvious change in the light dispersion in the irradiated spot after immersion in PBS and this change intensifies after seven days have passed (iii, b). The dimensions of the degraded area after seven days seem to expand a little bit compared to three days, but the speed of increase of the degraded area seems to reduce. Finally, the case observable in 4.5(c) referring to the spot produced at 0.3 J/cm^2 and wavelength of 266 nm shows again a gradual increase of

the degraded area with a progressive alteration of the light dispersion at the spot. The increase of the degraded area expands again in this case clearly exceeding the original borders of the spot observable after laser irradiation.

Further details on the morphology of these spots and the changes experimented by the irradiated material through biodegradation of the samples can be obtained from later experiments presented in [147]. The results explained in this reference show that when femtosecond laser pulses are accumulated on a fixed spot of the surface of PLGA, increased light scattering of the surface observable through optical microscopy can be produced without any perceptible morphology change of the surface when observed with SEM. Only at the highest incident pulse fluence value laser ablation was detected immediately after laser irradiation. Moreover, for spots processed with laser pulses of 400 nm wavelength, no morphology change was observed after laser irradiation in the studied cases processed with lower energy, but a porous structure appeared after immersion in PBS for 2 days. Consequently, it was concluded that degradation of PLGA can be accelerated without direct removal of the irradiated material through laser ablation, and that morphology changes of the processed surfaces can appear during degradation.

After analysis and measurement of the radii of the spots produced under the examined irradiation and biodegradation conditions, the obtained data were plotted in three plots gathered in Figure 4.6. Each value in these plots corresponds to the average of measurements carried out on the five spots produced under identical experimental conditions.

A first observation of the plotted data brings the attention on the significantly larger dimensions of spots shown in Figure 4.6(b), corresponding to the laser wavelength of 400 nm, even though the incident laser pulse fluence values were lower than for 800 nm and the laser beam size was kept constant at a diameter of 100 μm for all the cases. This observation is in agreement with a more efficient laser fluence absorption of radiation at 400 nm than at 800 nm, since for more energetic photons, i.e., shorter wavelengths, a lower number of photos must be simultaneously absorbed to overcome the material band gap through multiphoton absorption. In the case of the used PLGA, with an approximate band gap of 5 eV, 4 photons were necessary at 800 nm (1.5 eV) to induce multiphoton absorption, while only 2 photons were needed at 400 nm (3.1 eV) to exceed the band gap.
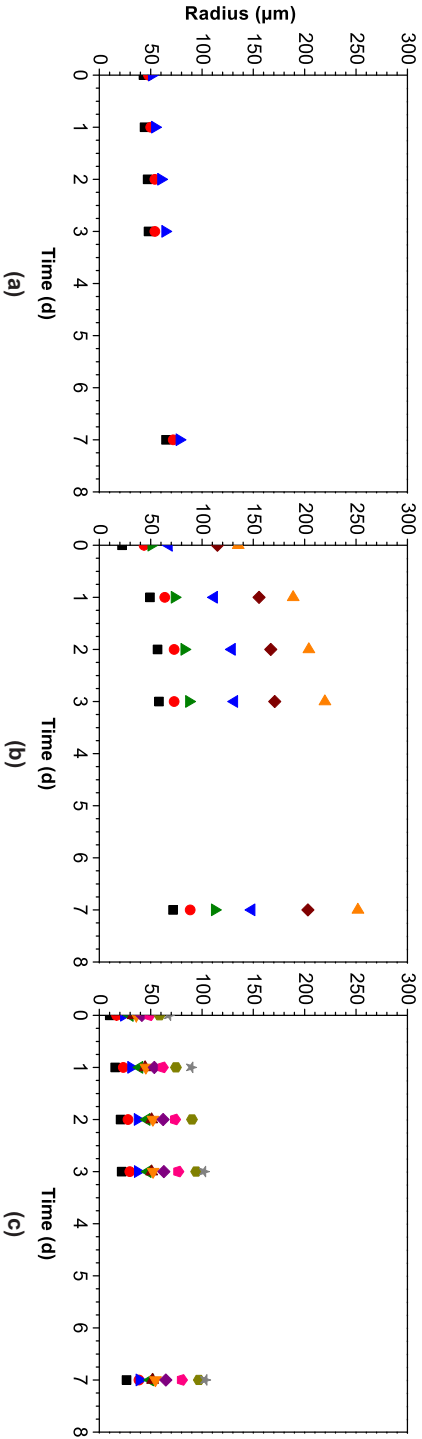
Figure 4.6: Plots showing the evolution in time of the average radius of the irradiated spot area measured through optical microscopy. The time progression in days (d) shows spot dimensions expanding through biodegradation produced by immersion in PBS during a total period of a week. Each plot corresponds to one of the applied laser wavelengths: (a) 800 nm, (b) 400 nm and (c) 266 nm. Each series of points correspond to the time evolution of the spots produced at a certain incident laser pulse fluence. For (a), these fluence values are 10.0 (black squares), 15.0 (red dots) and 25.0 J/cm² (blue triangles). For (b), fluence values are 1.0 (black squares), 2.0 (red dots), 3.0 (green up triangles), 5.2 (blue down triangles) , 10.0 (claret diamonds) and 14.9 J/cm² (orange left triangles). For (c), fluence values are 0.04 (black squares), 0.10 (red dots), 0.30 (blue up triangles), 0.51 (green down triangles), 0.72 (claret left triangles), 0.99 (orange right triangles), 1.5 (purple diamonds), 2.0 (pink pentagons), 2.9 (dark yellow hexagons) and 3.0 J/cm² (grey stars). The three plots are presented with the same scale to facilitate the comparison between them.

This lower number of necessary photons translates into a lower absorption threshold fluence, and therefore laser fluence is absorbed at the PLGA surface in a larger area at 400 nm compared to 800 nm for the same laser beam spot size. The case of 266 nm shown in Figure 4.6(c) has some differences with respect to the previous explanation. At 266 nm (4.7 eV), also 2 photons are necessary to surpass the 5 eV PLGA band gap. However, the lower available laser pulse fluence due to generation of higher harmonic radiation produces spots that are overall smaller compared to 400 nm. Nevertheless, spots produced with the same incident fluence at both 400 nm and 266 nm show comparable sizes, specially immediately after laser irradiation (time corresponding to 0 days). For all these reasons and from a point of view of laser energy absorption efficiency, 400 nm laser wavelength is the best value to produce larger spots with altered biodegradation behavior.

Figure 4.6 also contains information about the temporal evolution of biodegradation of PLGA by immersion in PBS for a total duration of one week. The first result that can be extracted from the analysis of the data is the different time scale of the biodegradation process between spots produced at 800 nm (Figure 4.6(a)) on one side, and 400 nm and 266 nm (Figure 4.6(b-c)) on the other side. In the first case, the radius of the degraded area of the spots discretely increased in a continuous way at a nearly constant rate, probably keeping this increase after the elapsed time of one week of the experiment duration. In contrast, the other case concerning the other two laser wavelengths showed a much relevant increase of the radius of the degraded spot areas. However, a much lower growth rate value was observed after one week of biodegradation, i.e., the expansion of the degraded areas seemed to significantly slow after one week of immersion in PBS had passed. In order to gain a more detailed knowledge about the evolution of biodegradation, the radius growth rate of the degraded spots area was calculated in accordance with equation 4.1

$$R(t_{i+1}) = \frac{r(t_{i+1}) - r(t_i)}{r(t_i)(t_{i+1} - t_i)} \times 100, \tag{4.1}$$

where $R(t_i)$ is the radius growth rate (in %/d), and $r(t_i)$ is the radius of the measured degraded area at a certain time t_i (in days, d) of immersion in PBS. This calculation makes possible a better comparison between the different examined irradiation conditions thanks to the elimination of the role of the observed spot size in the analyzed data. The calculated radius growth rates are plotted in Figure 4.7.

Results concerning the evolution of the biodegradation of the processed PLGA samples in Figure 4.7 point out a clear outcome: degradation occurs faster in spots produced at 400 nm and 266 nm than at 800 nm. While in Figure 4.7(a) radius growth rates at 800 nm oscillate around a daily increase of a 5%, higher values are observed at 400 nm and 266 nm (Figure 4.7(b-c)). Moreover, the degradation growth rate at 800 nm did not show a clear changing behavior with respect to time. This was not the case for the other two wavelengths, where there is a clear reduction of the growth rate along the one week duration of the immersion in PBS, from an average value of 45%/d after one day of degradation for spots produced at 400 nm down to 5%/d after one week. For spots processed at 266 nm, the reduction was from an average value of 30%/d after one day of degradation down to a 5% daily increase after one week. Similarly to what have been commented about radii of the produced spots, biodegradation seemed to happen a little bit faster for spots processed at 400 nm than at 266 nm. At both wavelengths spots produced at the lowest tested fluence show a notably higher growth rate than all the other studied fluences. This might be a consequence of the smaller dimensions of the spots produced at these lower fluences, where the visible spot on the PLGA surface produced by one laser pulse replicates the smaller region of the laser beam where fluence overcame the threshold fluence value for light scattering induction. Even that, the surrounding area was irradiated as well, since the laser beam spot on the surface had an approximate diameter of 100 μm. This contrast between the small visible spot left after laser irradiation and the total extension of the laser beam spot at the surface could be the reason of the higher radius growth rate values observed for the lowest incident fluence values.

To better understand this difference between effects on the biodegradation at the central area of the laser beam where higher fluences are reached and the surrounding area with lower fluences, an additional experiment was devised. The proposed strategy consisted in partially covering the PLGA surface with a piece of dark tape and firing one laser pulse at multiple positions, trying to impinge at the border between the covered part and the uncovered surface. The dark tape was removed after laser irradiation and before immersion of the sample in PBS for the degradation studies. To ensure the obtention of a few spots at the border between the covered and uncovered regions, various laser pulses were fired starting at a position and displacing the sample with a shift at the beginning of each line of

Figure 4.7: Plots showing the evolution in time of the radius growth rate of the degraded spot area according to the immersion time in PBS of the laser processed samples. The time progression in days (d) shows the growth rate evolution of the biodegradation produced by immersion in PBS during a total period of a week. Each plot corresponds to one of the applied laser wavelengths: (a) 800 nm, (b) 400 nm and (c) 266 nm. Each series of points correspond to the time evolution of the spots produced at a certain incident laser pulse fluence. For (a), these fluence values are 10.0 (black squares), 15.0 (red dots) and 25.0 J/cm² (blue triangles). For (b), fluence values are 1.0 (black squares), 2.0 (red dots), 3.0 (blue up triangles), 5.2 (green down triangles) , 10.0 (claret left triangles) and 14.9 J/cm² (orange right triangles). For (c), fluence values are 0.04 (black squares), 0.10 (red dots), 0.30 (blue up triangles), 0.51 (green down triangles), 0.72 (claret left triangles), 0.99 (orange right triangles), 1.5 (purple diamonds), 2.0 (pink pentagons), 2.9 (dark yellow hexagons) and 3.0 J/cm² (grey stars). Note that plot (a) shows a different y axis scale than the one in plots (b) and (c).

consecutive pulses, expecting that some intermediate holes would impinge at the border. To make easier getting the desired semicovered spots, the laser beam size on the sample was enlarged up to a diameter of 200 μm by moving away the focal lens with respect to the PLGA sample surface. The sample position along the surface plane was shifted 400 μm between consecutive laser pulses and each new line of spots started with a shift of 20 μm with regard to the previous line. In that way, at a couple of lines spots would be semicovered because of the laser pulses impinging partially directly onto the surface and partially onto the black tape covering the surface. Some spots with these conditions were obtained. They can be seen in Figure 4.8, which shows that non irradiated areas covered by the dark tape did not experiment any accelerated degradation. Oppositely, irradiated areas degraded in the same way as completely irradiated spots, even no apparent change was observed directly after laser irradiation. This result seems to indicate that the expansion of the degraded areas occur through degradation of the irradiated areas even if the laser fluence at that point does not produce a visible modification of the surface at a first stage rather than because of an expansion of the degraded spot in the surrounding area that has not received any laser radiation.

The commented biodegradation evolution of the irradiated samples followed trends similar to the ones shown in [145]. According to this reference, the origin of the increased PLGA degradation in 400 nm is not because of changes in crystallinity induced by laser processing, but it is based on a decrease in the molecular weight owing to photolysis of the PLGA chemical bonds, both at the polymer surface and bulk material. The shown results are also consistent with further experiments carried out in the same research group [147], which also confirmed the commented changes in the chemical properties of the irradiated PLGA even in the cases where material removal through laser ablation was not detected. Moreover, chemical structure change analysis of the processed PLGA surfaces concluded that faster degradation produced at the laser wavelength of 400 nm can be ascribed to an increased number of broken chemical bonds in comparison to the results produced by laser irradiation at 800 nm.

Furthermore, [145, 147] contain water absorption studies for the comparison of the biodegradation of irradiated samples in contrast with non-irradiated PLGA samples used as a control. This characterization technique adequately describes the degradation evolution of biodegradable materials in a physiological environment
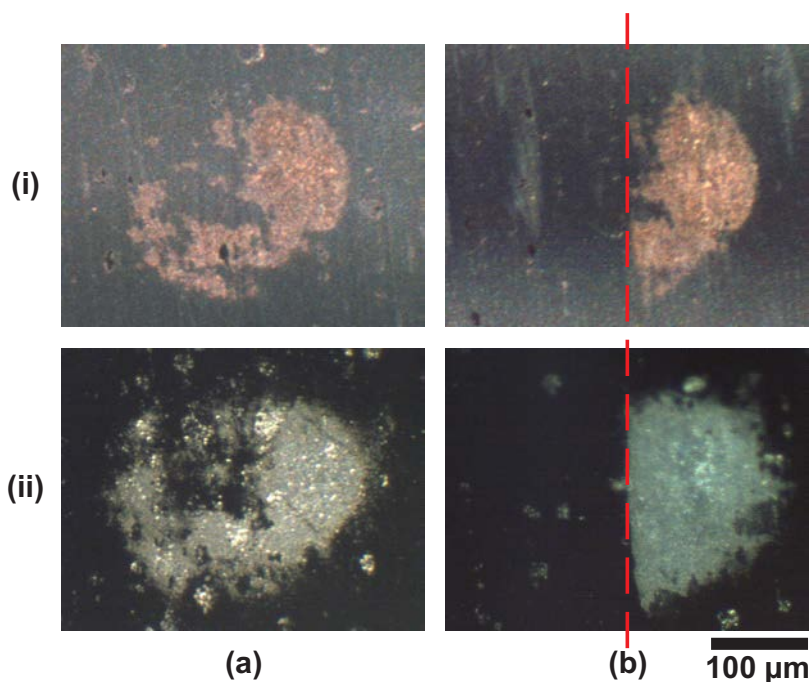
Figure 4.8: Optical microscopy images of the biodegradation process evolution of spots irradiated by single laser pulses at 266 nm wavelength and 0.6 J/cm^2 incident fluence. Row (i) contains the spots imaged immediately after laser irradiation and row (ii) contains spots after immersion during 3 days in PBS. The spot in column (a) was completely irradiated by one laser pulse, while the spot in column (b) was partially irradiated by covering the PLGA surface at that region with black tape. The dashed red line indicates the position of the border of the black tape covering the sample surface to avoid the irradiation of the covered part of the sample (left side of the dashed line).

since this process takes place in two steps. During the first one, hydrolization of the biodegradable polymer occurs, leading to a reduction of its molecular weight. This is followed by diffusion into the water of the lower molecular weight polymer regions, resulting in a reduction of mass of the degraded samples. Results in both references confirmed, through higher measures of the water absorption, the accelerated biodegradation observed in irradiated samples compared to the control, with a faster degradation of the samples processed with 400 nm laser pulses than at 800 nm.

For all these reasons, it can be concluded that material modification induced

by irradiation of biodegradable polymers like PLGA with femtosecond lasers is a feasible option for controlling and accelerating the biodegradation evolution of these materials.

4.2.   Laser perforation for leakage studies on medical use polypropylene bags

The versatility of the laser as a material processing tool with manifold applications becomes materialized in this case as a technique to reproduce commonly observed leaks in consumables with medical applications. Filamentation and other effects produced by laser absorption in the processed materials faithfully reproduce cracks and tears observed at the microscopic level in naturally occurring leaks in these materials.

Holes produced by laser drilling are useful for leakage studies on this materials demanding high performance and compliance of high quality standards. The possibility of controlled leak production through laser perforation makes possible the calibration of leakage detection systems widely used in quality control departments of companies dealing with industrial scale manufacturing of these products.

Bags made of polypropylene were the studied samples in the results presented in this section. Controlled leak production through precise laser perforation of the bag faces (200 μm thickness) for leak evaluation under controlled conditions was the main objective of this work. The executed process to reach this objective will be described in the following lines, together with the obtained results.

First experiments on this material consisted in laser pulse accumulation on a fixed spot on the surface of a polypropylene bag. For the preliminary experiments, rectangular samples were prepared by cutting one of the two faces of a bag to get a flatter piece of material to work with.

The first step of these preliminary experiments was finding the best z position of the laser beam waist with respect to the bag surface to perforate it with the best possible precision. For this reason, the chosen microscope objective to tightly focus the laser pulses onto the sample during this first stage was the $50\times$ 0.55 NA

200 µm
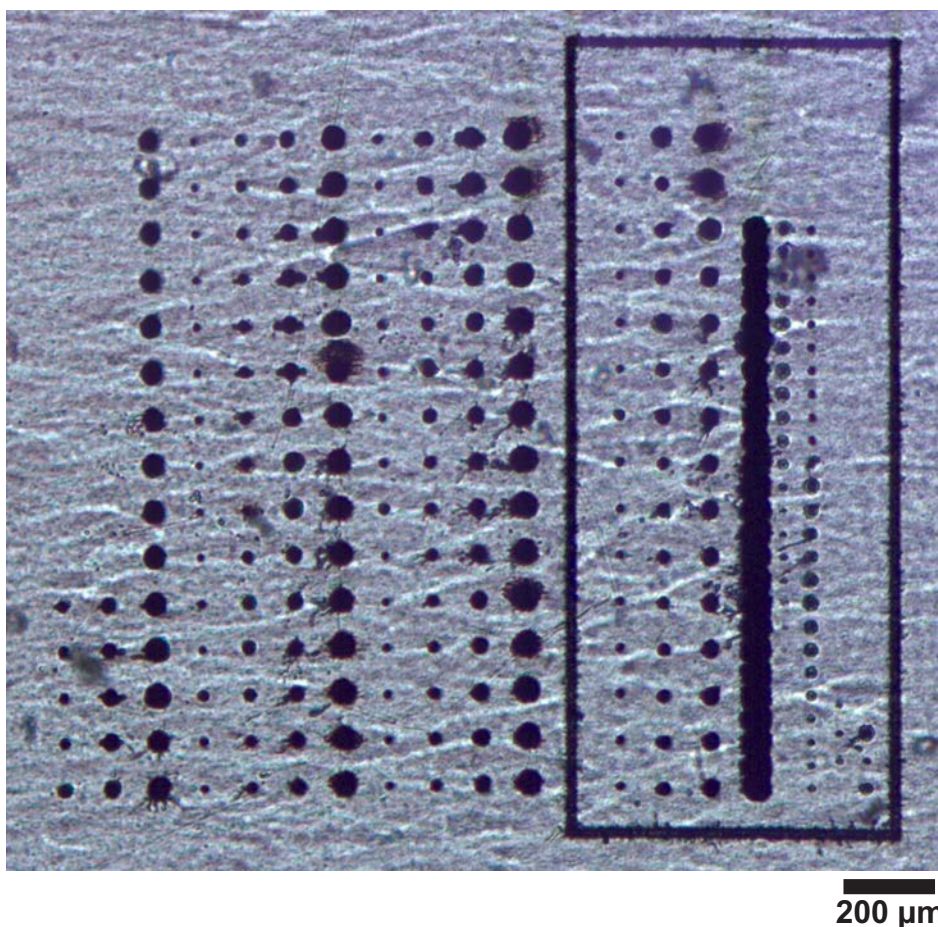
Figure 4.9: Transmitted light optical microscopy image of preliminary experiments carried out to select the best position for hole drilling by focusing of the laser pulses through the $50\times$ objective. All spots were produced at 1 kHz of laser repetition rate. (Rectangle) Each spot inside the right rectangle was produced by accumulation of laser pulses at a fixed z position. Columns of spots contain spots produced at the same incident energy but different z positions around the beam waist position laying at the sample surface. Rows consist of spots produced at the same z position but different incident energies. (Spots outside the rectangle) Each spot was produced by accumulation of laser pulses starting at a specific z position and displacing the laser beam waist inside the material at a constant speed during laser irradiation. Columns of spots correspond to a fixed value of the pulse incident energy for different starting z positions (increasing from top to bottom). Rows correspond to a fixed value of the starting z position for different incident energies (decreasing from right to left). The two spot series of four columns (and an additional smaller one of three columns) were produced at different values for the focus displacement speed. Since no complete drilling of the sample was observed, experiments carried out through this approach were discontinued.

objective. This position along the propagation beam direction (z axis) could be determined in a first approach by inspection at the beam profiler of the beam reflected by the sample (see Figure 2.4) and related then to spots produced on the sample thanks to observation through optical microscopy of the ablated spots produced at different z positions (see the framed spots in Figure 4.9). This figure was obtained through optical microscopy imaging with transmitted light in order to observe light passing through the holes when the bag face is properly perforated. As it can be observed in Figure 4.9, neither holes inside the rectangle (produced through laser pulse accumulation at a fixed z position of the laser beam focus with regard to the sample) nor outside the rectangle (produced through a 400 μm [twice the polypropylene bag face thickness] focus displacement at a fixed speed starting above the sample surface, going inside and crossing it) showed any visible light passing through them, what indicated with high probability an absence of complete hole drilling for all the produced holes. With the purpose of overcoming this situation, a new approach for the laser drilling process was implemented.

The new approach to produce the holes consisted in starting pulse accumulation at a z position of the laser beam focus below the sample (back surface) and displacing the focus beam waist upwards (for a clearer visualization, see Figure 2.4), namely, going through the sample and finishing again outside the sample, above the front sample surface. The total displacement z range was kept at 400 μm. This strategy was devised bearing in mind distortions that previously ablated material might have on the incoming laser pulses, which would arrive with reduced energy because of interactions with the already ablated material. Moreover, the new strategy would take profit of gravity for an easier evacuation of the expanding ablated byproducts and debris. These would follow the laser propagation direction, which coincides with the gravity pull and thus get away from the sample.

First results obtained following this new method can be seen in Figure 4.10, where the different available microscope objectives were put into test so that the one showing the best results with regard to the desired outcome could be selected. It can be seen that this was the case of the 20× objective. Holes produced under various conditions of energy and focus speed by laser pulses focused through this objective showed light passing across them, which seemed to indicate a complete drilling of the polypropylene bag face with regular contours and controllable sizes of the holes according to the different experimental parameters. However,
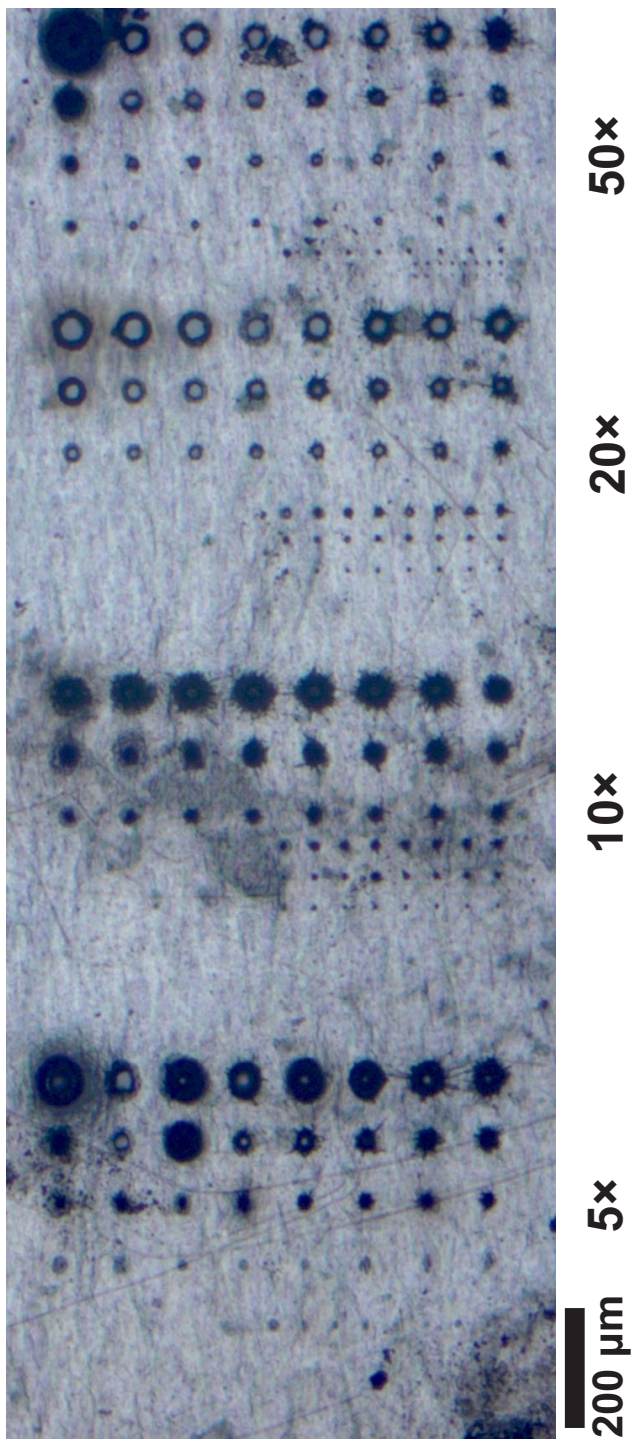
Figure 4.10: Transmitted light optical microscopy image of tests carried out to select the best microscope objective (indicated by its magnification) for the perforation of the bag faces. Each series of holes produced by focusing through one of the objectives contains holes fabricated at seven values of incident energies (16, 8, 4, 2, 1, and 0.5 μJ) decreasing from right to left and eight laser focus displacement speed values (2, 5, 10, 20, 50, 100, 200, and 500 μm/s) increasing from top to bottom. Clearly, the best results for a complete drilling of the bag face was obtained in holes produced through the 20× microscope objective.

the case for holes produced with the other objectives did not show so good light transmittance, as it can be observed with mostly dark spots present in the irradiated positions. This fact seemed to point out only a partial drilling of the sample. For this reason, these results obtained with the other objectives were discarded.
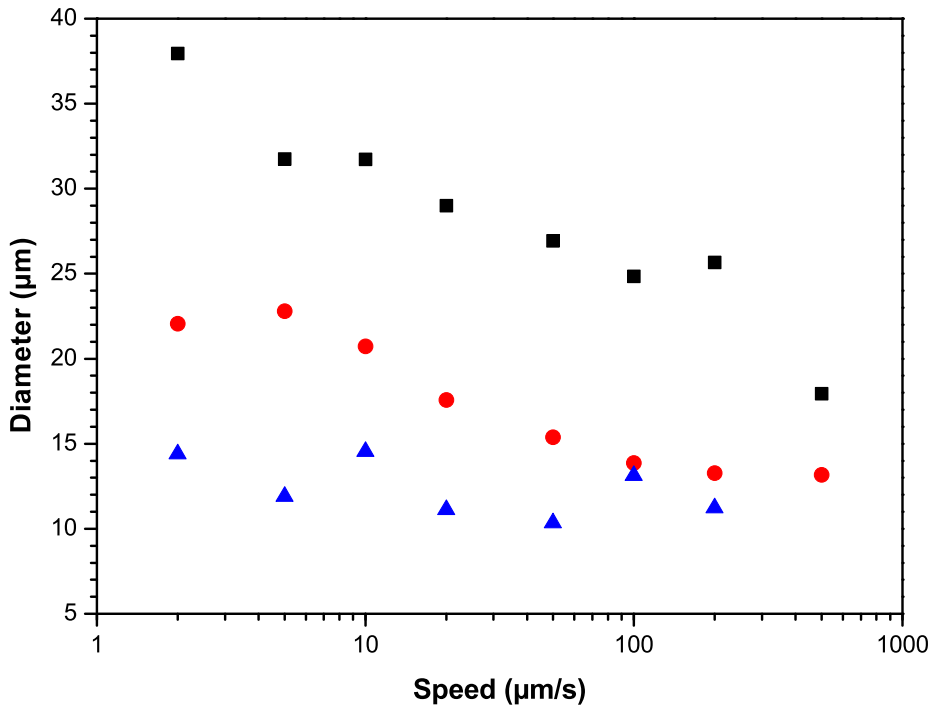
Figure 4.11: Semilogarithmic plot of the measured diameters of the light areas of the holes according to laser focus displacement speed fabricated with the 20× objective at pulse energy values of (**black squares**) 16, (**red dots**) 8, and (**blue triangles**) 4 µJ. The focus displacement along the z axis was 400 µm. The measured holes correspond to the ones shown in Figure 4.10. Some isolated holes were also obtained at lower energies, but they were difficult to properly measure with the optical microscope. Even more, they were out of the scope of a required minimum diameter of the holes of 10 µm.

Once the best focusing conditions were chosen, holes fabricated with the 20× microscope objective were measured in order to select the optimal experimental conditions for production of holes with a controlled size. The measured values are plotted in Figure 4.11. On one hand, the observed tendency for the different pulse energies indicates that for increasing focus displacement speeds, the diameters of

the holes reduced. This appears reasonable since higher speeds mean a higher shift between consecutive laser pulses and thus less overlapping, resulting in narrower holes. On the other hand, this hole diameter reduction seems to cover a wider range of diameter values for higher energies (from 40 to 20 μm at 16 μJ) , while for lower energies the diameter values only decreased a little, mostly oscillating between 10 and 15 μm at 4 μJ. Additionally, the range of measured diameter values for different pulse energies is also higher for lower speeds (from 40 to 15 μm at 2 μm/s) and significantly reduces for faster focus displacements (20 to 15 μm at 500 μm/s). As a consequence and to compromise between an extended availability of diameter values and speed of hole manufacturing, the speed of 50 μm/s was selected as the optimal value for production of through-holes with controllable dimensions satisfying these two conditions.
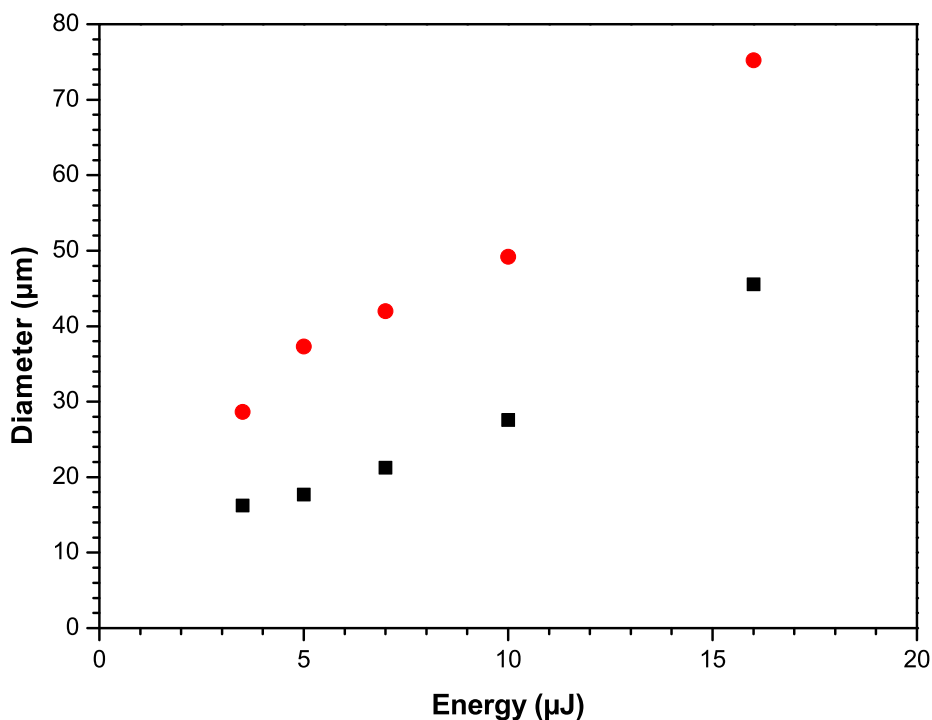
Figure 4.12: Plot of the measured diameters according to laser pulse energy of the (**black squares**) light area and (**red dots**) dark area visible in transmittance light optical microcopy images of the holes produced with the 20× objective at 50 μm/s of laser focus displacement speed along a total displacement of 1000 μm.

Next step consisted in the selection of pulse energies for the obtention of holes with controlled sizes. More specifically, leak sizes with effective hole diameters of 10, 20 and 30 μm were selected. Figure 4.12 shows measurements of tests done at various pulse energies with a fixed focus displacement speed of 50 μm/s along an increased total focus displacement of 1000 μm. This longer focus displacement answered the assurance of a complete and regular through-hole production. Pulse energies took values from the minimum values were through-holes seemed to be present (around 3 μJ) up to the maximum stable value supplied by the laser (in the range of 16 μJ). Measurements in this Figure 4.12 showed that under these conditions, the bag face could be drilled with holes having diameters ranging from 15 to 45 μm. With this results, pulse energy values could be interpolated and selected from the data for the production of holes with controlled diameters of 10, 20 and 30 μm at pulse energies of 3.0, 6.4 and 10.3 μJ, respectively.

Another attainable topic of the results in Figure 4.12 is the larger darker areas, almost double in size, surrounding the central light spots, these last ones related to light going across the sample and therefore associated to the presence of through-holes drilled along the whole sample thickness. The dark areas could be associated to refraction index changes present in the area immediately surrounding the hole and produced through melting by heat accumulation of the propagating laser pulses. To better study and comprehension of the meaning of these light and dark areas, a sample from the bags was conveniently irradiated and examined through scanning electron microscopy (SEM). The outcome of this experiment can be seen in Figure 4.13.

This figure shows holes produced at different experimental conditions for their examination at the SEM. However, more relevant were the series of three hole rows fabricated with exactly the same experimental conditions, which were included for an adequate study of the repeatability of the holes when the pulse energy becomes critically low for through-hole drilling. This is the case of 3 μJ for the obtention of the smallest leaks with 10 μm diameter. Through comparison of the transmitted light optical microscopy image (left) and the SEM image (right), it can be clearly perceived that dark areas correspond to inner material modifications that are not visible in the SEM image of the sample back surface. Furthermore, a detailed inspection of the SEM image showed that obstructed holes matched the completely dark spots observed in the optical microscopy image, while holes without a visible
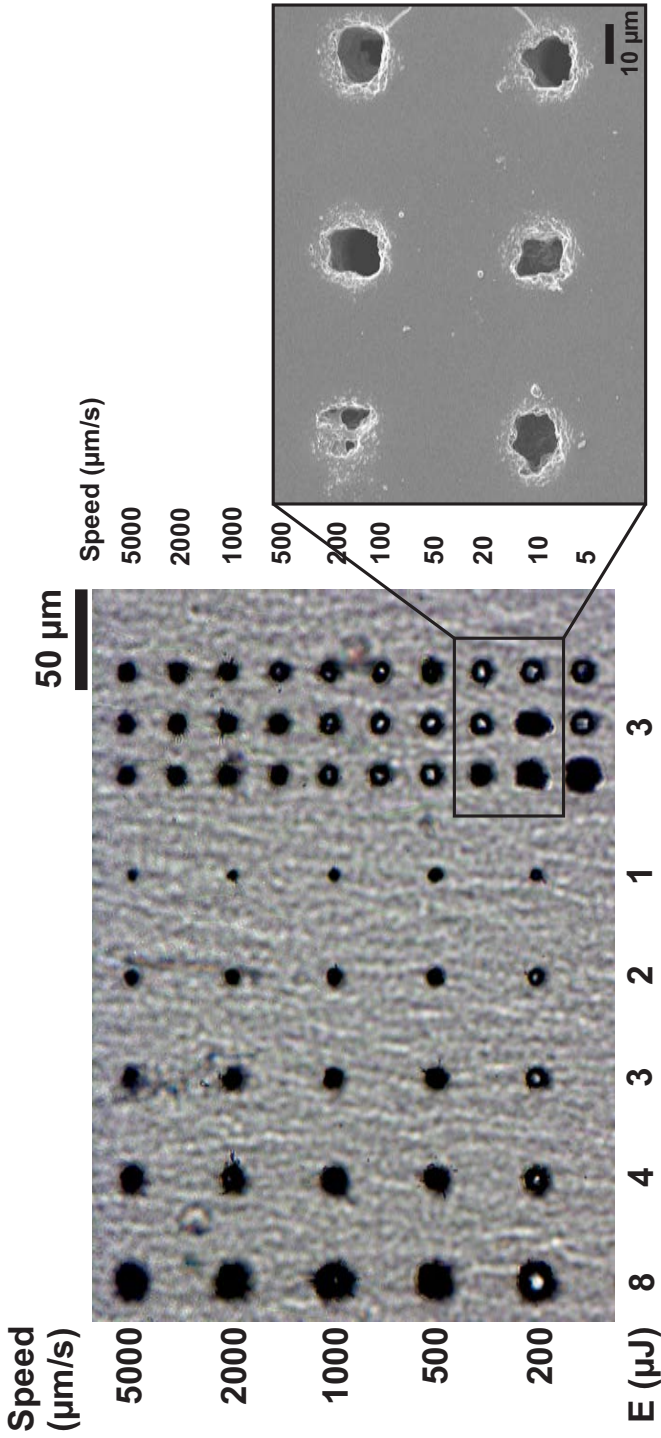
Figure 4.13: Transmitted light optical microscopy image of holes produced with the $20\times$ objective at various laser focus displacement speeds and incident energies along a total displacement of 1000 µm and (inlet) scanning electron microscopy image of the framed holes on the sample back surface. Each of the three right columns of holes contains holes fabricated at a fixed pulse energy of 3 µJ and at ten laser focus displacement speed values decreasing from top to bottom. The three holes in each row were fabricated with exactly the same experimental irradiation conditions. It is noteworthy that even thought the experimental conditions were the same, because of the critical energy value of 3 µJ holes in a same row showed clearly different morphologies, showing the presence or absence of a through-hole.

bottom were the ones with a visible central light area in the optical image. Hence, it could be verified that holes presenting a central light area effectively correspond to through-holes drilled along the whole sample, whereas spots showing a complete dark area without any presence of a central light area indicate that in that case, a complete through-hole was not obtained. No leak was produced under these last circumstances. This situation raised a conflictive question: how could the presence of a through-hole be ensured for critical energies if holes produced under the same experimental parameters could lead to either the presence or the absence of a through-hole? An answer to this question was the proposed strategy explained next.

After the multiple tests, drilling of the bags faces (not only of samples cut from them) was carried out. To obtain a practical shape of the bags, these were inflated with compressed air until the bag walls were tense and the two faces of the bag separated. This procedure also made possible the detection of the effective creation of a through-hole on the bag, namely, a controlled leak. If a leak was not created after laser drilling, the bag remained inflated and no change in the reflected beam was perceived. But when a leak was created by laser drilling, the inflated bag started deflating, producing a detectable change in the laser light reflected by the bag surface after laser drilling. This change was a defocusing of the reflected laser beam, which was visualized at the beam profiler as a modification in the reflected light intensity and energy distribution. The setup was able to detect focus position changes down to 2 μm. The laser light used in this case was radiation coming out from the laser but without being amplified, hence not producing any modification on the sample. It was exclusively employed for the sample surface visualization at the beam profiler through its reflection on the sample surface. This simple method made possible the verification of the fabrication of controlled leaks in all the processed bags for later leakage studies.

In addition to the verification of leak production in the bags through inspection of the reflected laser light, a complementary method was used to completely confirm that the processed bags were perforated. This method consisted in the immersion of the perforated bags in a recipient full of water. Since the produced leaks on the bags were microscopical, the bags remained inflated even when they were strongly compressed by applying pressure with the hands. For this reason, when the bags were immersed in water and at the same time intensely squeezed,

small air bubbles appeared at the location on the bag surface of the laser fabricated leak. This was a definitive proceeding for a conclusive and easy confirmation and location of the produced leaks.
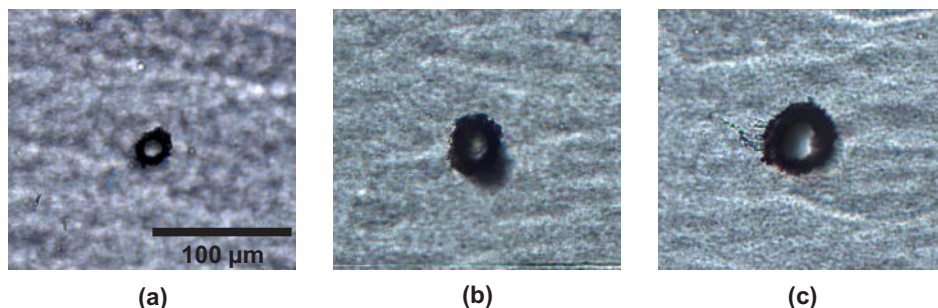
Figure 4.14: Transmitted light optical microscopy image of fabricated leaks with controlled size through-holes of (a) 10, (b) 20, and (c) 30 µm of effective diameter produced with pulse energies of (a) 3.0, (b) 6.4, and (c) 10.3 µJ through laser drilling at a focus displacement speed of 50 µm/s along a total focus displacement of 1000 µm across the sample with the 20× microscope objective. Optical microscope objectives with higher magnification could not be used for imaging of the produced leaks because of the high rugosity of the bag surface.

Controlled size leaks of 10, 20 and 30 µm diameter could be adequately fabricated thanks to implementation of the presented strategies. The fabricated through-holes can be observed in Figure 4.14. These through-holes showed an irregular contour (light central area) and internal modification (surrounding dark area), which faithfully recreate the morphology of leaks naturally occurring in this material. Nevertheless, they contrast with the defined edges and straight walls obtained in experiments carried out on PLA (see Figures 4.1 and 4.3). However, in this case these irregular shapes and inner material alterations are good features as their goal is to replicate leaks in polypropylene bags, which was the pursued aim of this research.

To conclude this part, it is pertinent to highlight that the terms asked in the collaboration with the pharmaceutical company doing leakage studies with the laser drilled bags were satisfactorily accomplished. As a sign of that, leakage detection system studies could been successfully carried out with the prepared bags.

4.3. Laser fabricated microfluidic guides for conductive line printing

The most common digital printing procedure for the fabrication of lines consists in depositing consecutive overlapping droplets. Figure 4.15 illustrates the outcome of this procedure for a test with silver nanoparticle conductive ink printed on a glass substrate. In this experiment, different overlaps were examined with the intention of reaching the optimal conditions leading to formation of stable continuous conductive lines free from defects. The shifts between adjacent droplets (Δx) in Figure 4.15 correspond to the droplet center to center distance and range from 160 to 25 μm. The first two values ($\Delta x = 160$ and 120 μm) result in isolated droplets with diameters around 80 μm. When the shift is reduced to a value equal or smaller than the droplet diameter ($\Delta x \leqslant 80$ μm), droplets coalesce and the printed patterns result first in dashed lines ($\Delta x = 80-72$ μm), and continuous lines for smaller shifts ($\Delta x \leqslant 56$ μm). Unfortunately, in these last cases where continuous lines are achieved bulges are always present, usually at the beginning of the line and occasionally in the middle. This kind of defect is highly detrimental in electronic circuits since it can easily lead to unwanted short-circuits between adjacent lines. For this reason, it is clear that the initial objective is not fulfilled: no continuous lines free from defects could be obtained with this single step printing process.

In previous experiments done at the research group where this thesis was developed, a simple printing strategy to avert the spontaneous formation of bulges was proposed [148]. The approach consisted in the alternate deposition of odd and even droplets with an intermediate drying step in-between. This strategy proved successful as dried pixels helped confining the recently deposited liquid. This advanced along the successive dry pixels, which pinned the contact line and confined capillary flows responsible for bulge formation along the printed lines. However, this procedure was quite inefficient (the intermediate drying step was time consuming) and the final result did not show an acceptable final quality: in spite that the printed lines were free from any bulge formation, they presented a scalloped profile which hindered the definition and homogeneity of the printing outcome. Notwithstanding, the strategy provided an idea for a more efficient and better approach: printing ink droplets in previously manufactured fluidic guides. Since bulging is basically a problem of liquid displacement beyond the parallel edges of

Overlap (%)
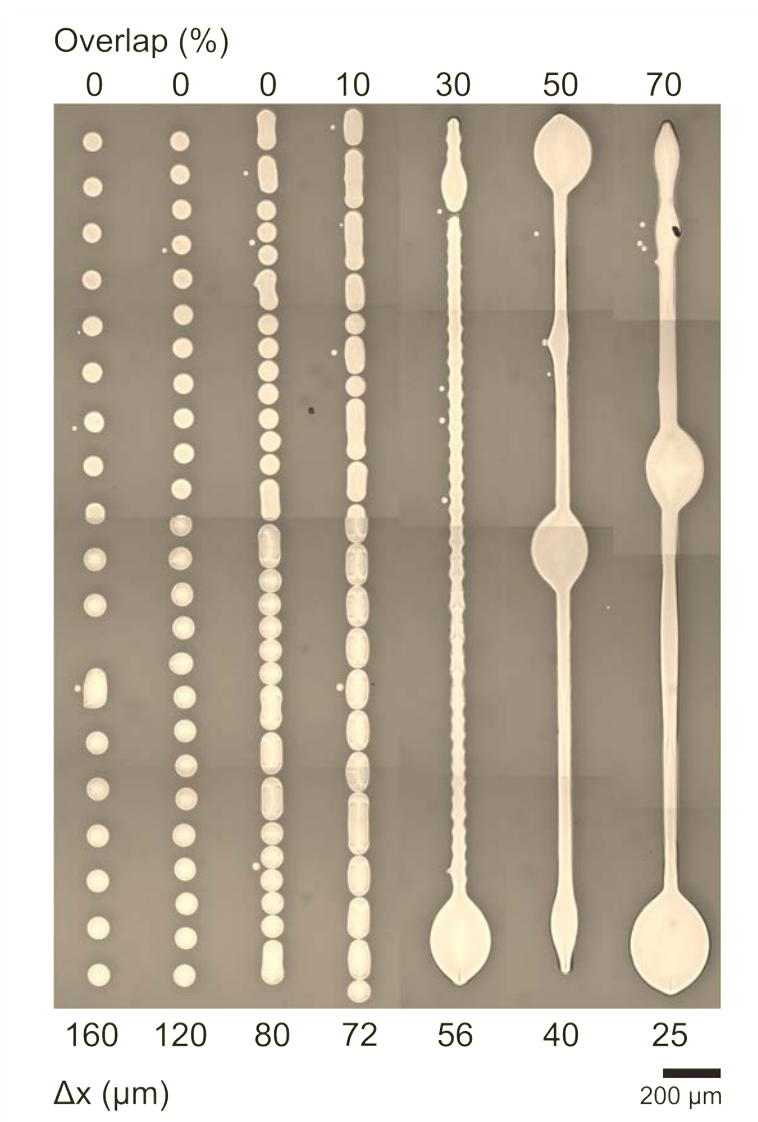
Figure 4.15: Composition of optical microscopy images of lines printed with different shift values between consecutive droplets (Δx, measured from droplet center to center) decreasing from left to right.

the printed line due to the onset of an instability driven by capillary flow arisen from surface tension gradients during the printing process, the presence of a guide should help confining the liquid and thus prevent the formation of bulges.

As it has been already commented in subsection 2.2.2, the experiments in this section were performed using a microscope objective of $50\times$ magnification with a numerical aperture of 0.55 to focus the laser radiation onto the samples. In this case, the position of the laser beam focus along the sample surface plane was controlled thanks to the CMOS camera placed coaxial to the laser beam axis (see Figure 2.4). However, the position of the laser focus beam waist along the z axis and with respect to the processed sample surfaces was controlled through inspection of the reflected laser beam by the sample surface and observed at the beam profiler (Bp in Figure 2.4).

4.3.1.   The Laser Induced Forward Transfer (LIFT) technique

For a better understanding of the experiments presented in this section, a short description of the LIFT printing technique will be introduced. The operational principle of the technique can be easily described with a diagram like the one shown in Figure 4.16. In order to print the desired material onto a receiver substrate, a laser beam (a) is focused through a microscope objective (b) onto a thin film of the material coating a transparent holder (c) that acts as a support for the thin film. In the case of ink printing, the material coating is prepared as a liquid film (d) covering the support holder. As soon as the focused laser beam propagates through the transparent holder and reaches the liquid film, laser radiation is absorbed inside the film, creating a cavitation bubble (f) that expands and, when the laser irradiation conditions are adequate, produces the ejection of a liquid jet (g) that elongates in the incident direction of the impinging laser pulse. For a proper range of values of the gap between the liquid donor film free surface and the receiver substrate (e), the jet contacts the receiver substate and produces a droplet (h) of the liquid donor film ink. This droplet is gently fed by the jet until the jet breaks and recedes to the liquid donor film, leaving a printed droplet onto the receiver substrate. More information about the LIFT technique can be found in an extensive review like [27].

In the LIFT experiments for droplet printing, laser pulse incident energy was
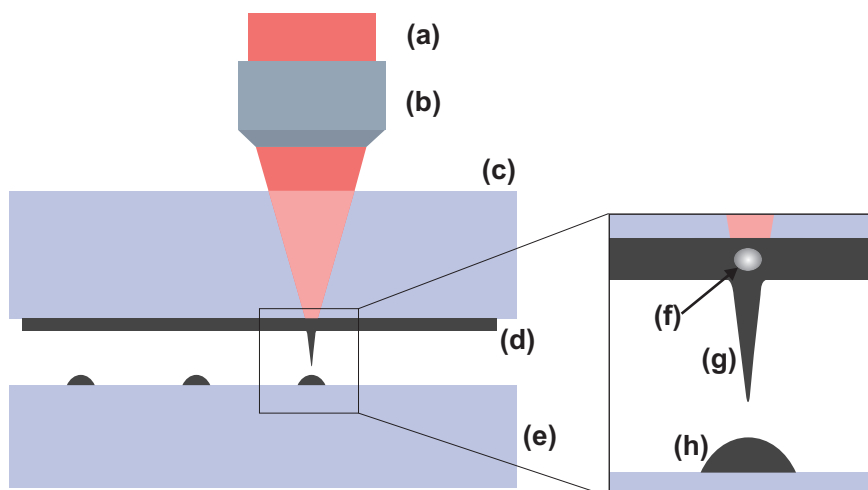
Figure 4.16: Diagram describing the process of LIFT printing experiments: (a) laser beam, (b) microscope objective, (c) glass slide acting as a liquid film support, (d) liquid donor film, (e) receiver substrate, (f) cavitation bubble, (g) liquid jet, and (h) printed droplet.

600 nJ and the laser spot diameter at the interface between the glass slide holder and the ink film where the laser radiation was absorbed was 12 μm. This was significantly larger than the laser spot diameter used in the fabrication of the fluidic guides. The incident energy and spot size combination resulted in a laser fluence of 530 mJ/cm^2 for each laser pulsed used to print the ink droplets by LIFT. In these conditions, printed droplet diameters on the glass receiver substrate had sizes in the range of 180 μm. Although much smaller diameters can be obtained through conventional LIFT [149], the printing conditions required to achieve such precision are very sensitive to non uniformities in the thickness of the liquid donor film. Since the purpose of the presented experiments was to prove the feasibility of the proposed printing strategy and not to optimize its resolution, the most propitious conditions for the tests were chosen. For this reason, relatively large droplets were printed in order not to compromise the reproducibility of the printing process.

4.3.2. Microfluidic guides produced by laser ablation

As introduced previously at the beginning of this section, the new printing approach proposed for production of conductive ink lines free from defects consisted

in a two-step process. The first step was the fabrication of fluidic guides. These were obtained through selective laser ablation of a polymer layer coating the glass receiver substrate on top of it (Figure 4.17a).
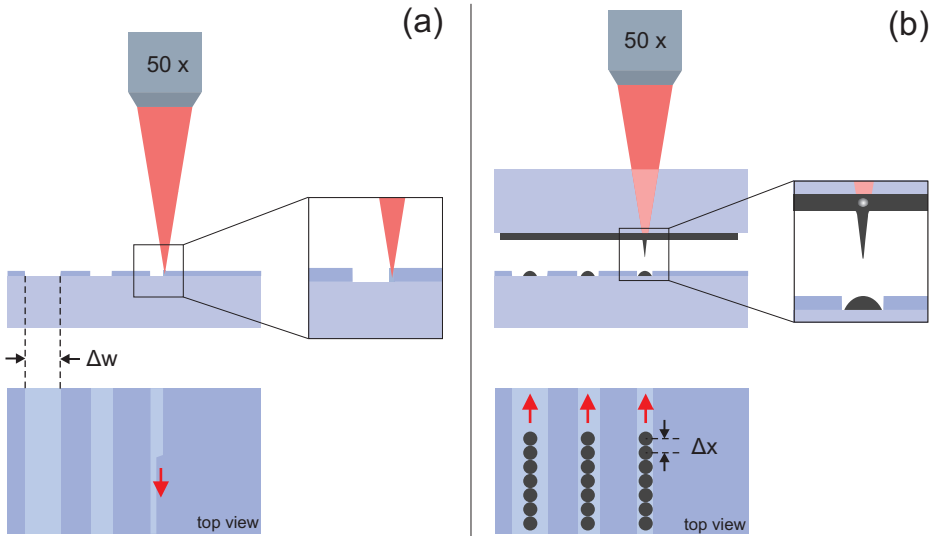
Figure 4.17: Sketch of the setups and procedures used for (a) laser ablation of the fluidic guides with different widths (Δw) and (b) LIFT of the silver nanoparticle ink inside the fluidic guides applying different printing shifts between consecutive droplets (Δx, measured from droplet center to center).

The fluidic guides were produced using a pulse energy of 75 nJ focused into a laser spot with a diameter of 2 μm, which corresponded to a laser fluence of about 2.4 J/cm^2. The production of a single fluidic guide was executed by scanning the interface between the polymer layer and the glass receiver substrate at a speed of 1 mm/s and a laser repetition rate of 2 kHz. This resulted in a shift of 0.5 μm between consecutive overlapping laser shots. A shift of 1.0 μm between successive scans was applied to completely ablate the polymer coating.

The use of this additional polymer coating had advantages over the direct ablation of the glass surface. First of all, the removal of the polymer layer requires substantially lower fluences than those necessary for the direct ablation of glass, between 3.1 and 6.4 J/cm^2 according to [150]. If the laser beam is focused at the polymer-glass interface, it is possible to easily detach the polymer coating at a

low enough fluence, which leaves the glass surface below undamaged. As a consequence of that, a much cleaner ablation could be obtained: as it it can be observed in Figure 4.18, the bottom of the produced fluidic guides in form of channels was flat and its walls showed a sharp and straight finish (the minute scalloping of the joints where the channel walls and bottom meet was a result of the 0.5 μm shift between consecutive laser shots during the laser scanning for channel fabrication). Comparable sharp edge profiles were reported during laser ablation of PMMA films on top of glass [151].
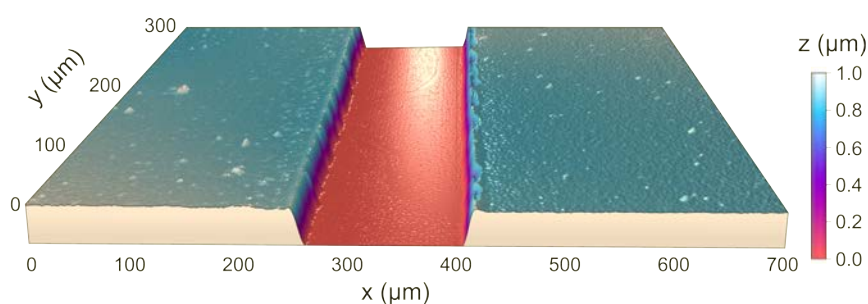
Figure 4.18: Laser ablated fluidic guide on top of the receiver substrate. The clean and complete ablation of the 1.0 μm thick polymer layer, which left the underneath glass unaltered (flat red region), can be observed. The width of the guide is about 150 μm.

In this case, glass receiver substrates were coated with a 1 μm thick hydrophobic cross-linked polymer layer. After the fabrication of the fluidic guides, these were filled with printed conductive ink through LIFT. For the purpose of properly confining the ink inside the guides, it was necessary that the polymer surface was considerably more hydrophobic than the glass substrate. The hydrophobicity of the polymer was achieved through the use of a fluorosurfactant additive. This combination of polymer layer and glass was chosen for convenience, since the main objective of the experiments was to prove the feasibility of the proposed printing approach, but it is expected that a wide range of other combinations might be also effective, provided that both the coating layer and the substrate exhibit an acceptable difference in surface energy to contribute in the confining of the printed lines along the guides.

The second step of the proposed printing strategy was the LIFT of conductive ink inside the fluidic guides (Figure 4.17b). Since the polymer coating is transparent

to most used laser wavelengths, its ablation through interaction with the laser radiation requires femtosecond laser pulses. If tightly focused, they are absorbed essentially by any material, and for that reason the same laser pulses can be used for LIFT as well. As a remarkable consequence, both steps, ablation and printing, could be implemented by the same laser system.

4.3.3.   Printing into laser ablated fluidic guides for conductive line production

Once the fluidic guides were created, conductive nanoparticle ink droplets were directly printed inside the channels by means of LIFT. The results of a first experiment can be observed in Figure 4.19. In this case, fluidic guides of different widths ranging from 60 μm up to 200 μm were fabricated, and the shift between successive droplets (Δx) was fixed at 160 μm. First results showed some promising behavior: for three out of five width values (100, 80 and 60 μm) continuous lines free from bulges or scalloping were obtained. In these three cases, the ink uniformly covered the guide and was tolerably confined within. These lines were significantly narrower than the diameter of each individual printed droplet ($\sim$180 μm, measured for a droplet directly printed on a glass substrate), which clearly implies that the pursued guiding effect was successful. However, the complete confinement of the ink was not totally satisfied. Certainly, there was some overflow beyond the edges defined by the walls of the fluidic guides. The overflow extent was surprisingly similar in the three guides, even though they had different sizes and that the amount of transferred ink was always the same. A first approach to the results would expect the largest amount of overflow to be found in the narrowest guides, which eventually should not be able to contain the excess of ink. In spite of that and in view of these results, it is reasonable to presume that the overflow was not produced to an ink excess. Contrarily, it could be attributed to ink climbing up the polymer walls, which seemed to become hydrophilic after the ablation process (either because of induced roughness and/or a chemical composition change). A close inspection of the borders of non-printed guides revealed the remains of some debris originated from re-deposition of polymer ablation products. Therefore, the crawling ink would then overflow beyond the edge of the guides until it arrives at clean hydrophobic region of the polymer surface. This border between the debris remains and the clean surface would define and contain the advancing contact line of the ink.

For the purpose of assuring a better confinement of the ink within the guides, and with the assumption that the observed overflow is a result of the presence of ablation debris, an air flow that helped removing ablation byproducts was incorporated to the experimental setup. This time, a new experiment consisting in printing inside guides that had been ablated with the air flow on was carried out. But in this case, instead of fabricating guides with different width values and printing droplets at constant shift between them, the parameters were exchanged: droplets separated by shifts ranging from 240 to 60 μm were printed inside 200 μm wide guides (Figure 4.20a). Isolated droplets were obtained at a shift $\Delta x = 240$ μm, since their diameter is about 180 μm and no overlap is possible. As the shift decreased, the printed droplets began to coalesce, but no continuous line was generated until the shift reached 80 μm. At this shift the line was not uniformly covered, probably because of an insufficient printed ink volume. Moreover, some overflow occurred at a localized point, where in spite of the air flow some debris remains probably deposited. Finally, a further reduction of the distance between droplets to 60 μm reached the initial objective: the fabrication of a continuous line uniformly covered by ink completely confined within the guide. In fact the final definition is outstanding, free of bulges, scalloping or overflow at all, which serves as a proof of the feasibility of the proposed strategy.

The results validation of the proof-of-concept test admit some pertinent discussion. The printed lines presented were significantly wider than features with smaller sizes that can be produced through conventional LIFT [149]. The reasons for this situation have already been indicated in the beginning of this subsection, and therefore the initial goal of the studies was fulfilled. Nevertheless, it would be desirable that the new approach could show resolutions close to values attainable with the conventional method. In this direction it can be stated that there is no evident limitation inherent to the presented approach that could hinder that aim. On one hand, it is possible to print droplets through LIFT with minimum diameters close to 10 μm, and on the other, fluidic guides with similar widths can be easily produced through laser ablation. Therefore, it is not unreasonable to expect that resolutions in the range of 10 μm could be achieved with the proposed strategy.

In order to illustrate with an example the possibilities of this printing approach, a demanding test of the degree of control and definition of the technique was pro-
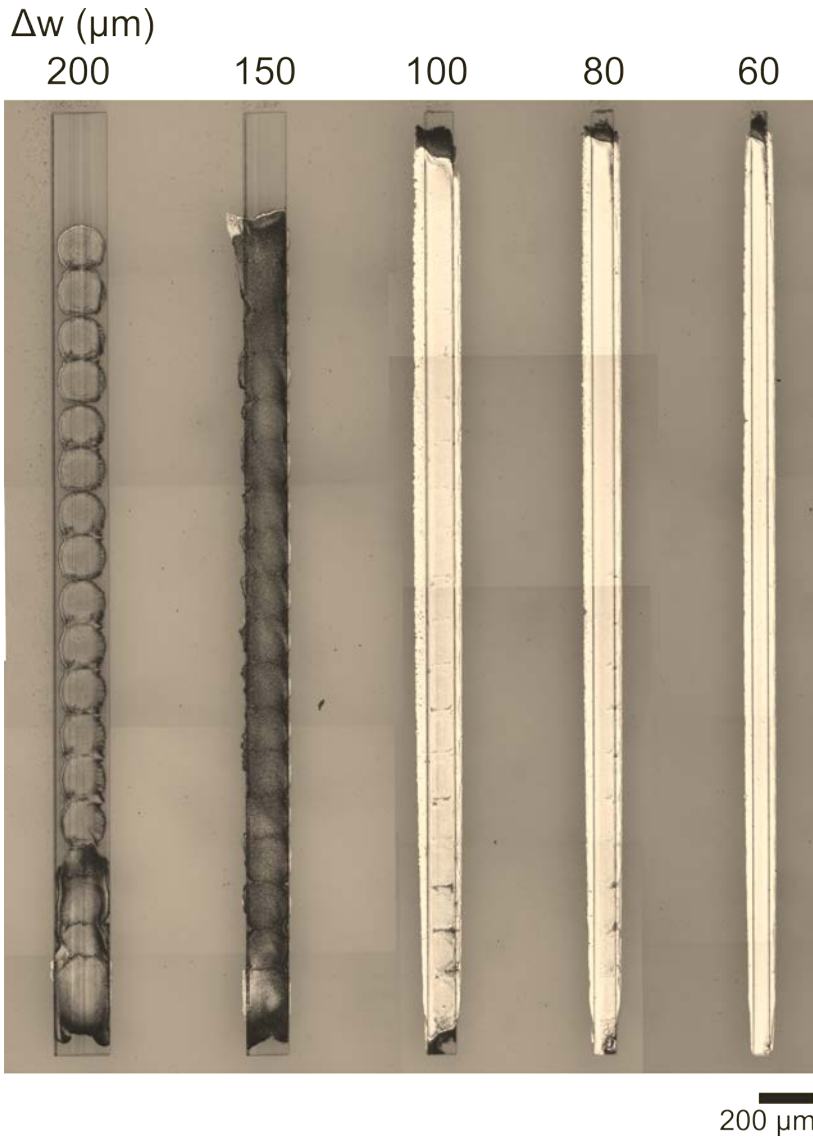
Figure 4.19: Lines generated by printing the silver nanoparticle ink through LIFT inside the fluidic guides of different widths (Δw). The shift between successive droplets (measured from center to center) is constant at 160 µm.
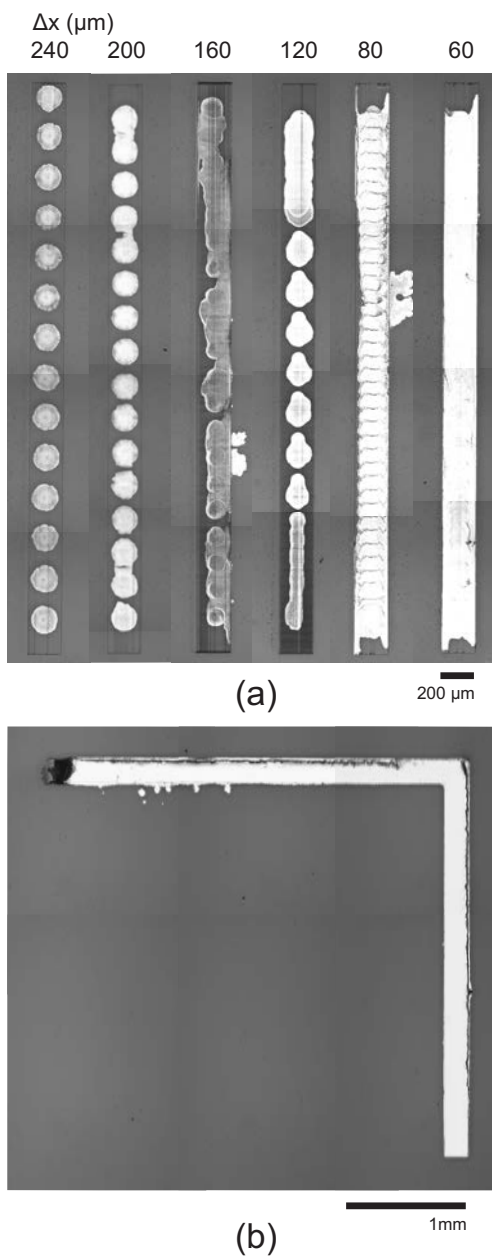
Figure 4.20: (a) Lines generated by printing silver nanoparticle ink through LIFT at different shifts between consecutive droplets (measured from center to center) inside fluidic guides with a constant width of 200 μm. (b) Pattern consisting in two long and connected straight lines forming an angle of 90° fabricated through LIFT of silver nanoparticle ink inside previously ablated fluidic guides of 200 μm width.
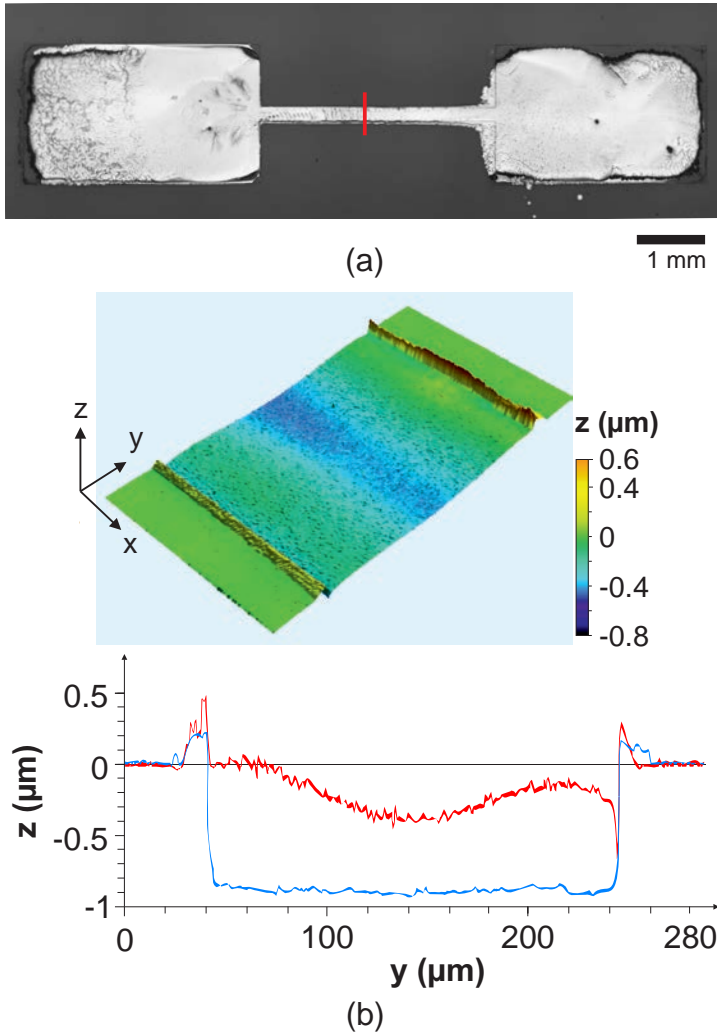
Figure 4.21: (a) Pattern consisting in two 2×3 mm rectangular pads connected by a 200 μm wide line produced by laser ablation and subsequently filled with Ag ink printed through LIFT. (b) Confocal microscopy image and transverse profile of the line indicating the correct filling of the guide with the Ag ink.

posed. For this purpose, the realization of a challenging pattern was chosen: two long and connected straight lines forming an angle of 90°. The obtained result is presented in Figure 4.20b. As it can be observed, the finishing quality of the pattern was quite high, with the most common line printing defects completely eliminated. The lines showed almost perfectly straight edges and the 90° angle exhibited a definition and completion impossible to achieve through the direct printing of overlapping droplets on glass without the guides. In spite of the length of the angle sides (about 3 mm), the liquid confinement within the guides was practically total. Only a few tiny overflow spots are perceptible at the lower edge of the horizontal side, again possibly due to debris which was not completely removed by the air flow during the ablation process. In conclusion, this realization constituted a relevant proof that the strategy of LIFT printing inside laser ablated fluidic guides makes possible the fabrication of complex patterns with a high definition and degree of control.

As a final test, the application of the produced conductive lines as interconnects in electrical circuits was verified. To that end, a pattern consisting in two 2×3 mm rectangular pads connected by a 200 μm wide line was fabricated by laser ablation and filled afterwards with conductive ink through LIFT. The devised pattern should allow measurements of the electrical resistance of the line between the two pads acting as contacts. After leaving the sample some time to dry, the pattern was laser cured to improve the conductivity of the silver nanoparticle ink. Figure 4.21a shows an optical microscopy image of the final pattern after curing, where it can be observed once more that the fluidic guides confine the ink within their limits without significant overfilling. With the intention of measuring the ink level inside the fluidic guide, confocal images of the connecting line were acquired, as shown in Figure 4.21b. The ink covered around 85 % of the ablated volume with good uniformity along the line and has a roughly constant thickness. As a last step, the conductivity was measured, resulting in a value of $10\cdot10^6$ S/m, very close to the nominal value provided by the ink supplier after curing in an oven ($9.1\cdot10^6$ S/m). This indicates that the strategy of LIFT printing inside laser ablated fluidic guides is a convenient technique for the production of high definition conductive patterns free of the most common printing defects.

The presented strategy of depositing a conductive ink through LIFT inside laser ablated fluidic guides was proved feasible for printing stable and continuous lines with remarkable definition and control. The most relevant conclusions that could

be extracted from the presented results are now given. For a fix fluidic guide width, there is a range of overlaps between consecutively printed droplets that results in the perfect confinement of the ink inside the guide. Thanks to that, most typical defects in line printing such as scalloping and bulges were eradicated. The successful application of the described approach to the realization of a challenging pattern consisting in two long and connected straight lines forming an straight angle unveiled the potential of the method for the production of patterns with complex geometries with an outstanding degree of definition. Finally, laser curing of the printed lines has demonstrated that their conductivity can be increased to values similar to the results obtained through curing in an oven. This also demonstrates the potential of the printed patterns as interconnects in electronic circuits.

5 Conclusions

The following conclusions can be extracted from the main results obtained during the development of this doctoral thesis, which met the initial pursued objectives.

- An automatized and fast laser direct-write experimental equipment including an ultrashort pulsed laser for microprocessing of different kinds of materials was successfully devised and put to work.

Z-scan focusing method

- The devised strategy of using in situ transmittance measurements during a z-scan as a technique to keep track of the experimental focusing conditions has proven successful as a method for effectively and precisely positioning transparent materials at the laser beam waist to process their surface.

- The z-scan focusing method was characterized along different z positions on the beam propagation axis. The analysis of the superficial ablation produced along these different z positions made possible the accurate determination of the optimal position range to induce ablation on the surface of a transparent material like PMMA, which for intermediate values of the laser pulse energy extended along 3-4 μm.

- The analysis of the produced superficial ablation also made possible identifying different z position ranges according to the kind of superficial ablation induced. Strict superficial ablation was obtained only in z positions corresponding to the situation where the sample surface starts entering the laser beam waist region. It was observed that positioning at these locations is quite critical, so for a more reliable and regular superficial ablation in the shape and dimensions of the produced spots, the sample should be placed along the intermediate zone in the transmittance curve corresponding to the transmittance z-scans. Swelling of the processed spots in form of bumps was

observed for z positions corresponding to the laser beam waist laying already inside the material but still close to its surface. No superficial modification was observable when the laser beam waist was located well inside.

- The observation through FIB processing of the cross section of the produced spots by single laser pulses revealed that a porous structure inside the bulk material could be found laying directly below the produced spots. Its presence was related to the expansion of the vaporized material inside the sample, leading to an increased final dimension of the produced spots.

- The agreement between experimental and predicted data worked out with vector diffraction theory simulations of the laser beam profile together with their corresponding measured transmittance values made possible identifying the z position corresponding to the laser beam waist laying at the sample surface.

- Similar results for controlling the focusing conditions with the z-scan focusing technique were also obtained in the production of microchannels on the surface of PMMA through laser scanning. The control of the sample surface tilt with respect to the laser beam propagation direction secured the surface ablation along large areas. Continuous channels with widths and depths below 1 μm could be fabricated thanks to the provided focusing control along a total length of 2 mm.

- Owing to pulse accumulation and overlap during the production of microchannels through laser scanning, surface swelling in form of lines of consecutive bumps was observed in two distinct experimental conditions: when the sample surface starts entering the laser beam waist region and when the laser beam waist is already located inside the material but still close to its surface.

- Simultaneous transmittance and reflectance measurements made possible controlling the sample position with respect to the laser beam waist during the surface ablation experiments.

- The control on the focusing position provided by the z-scan focusing technique made possible the obtention even with different incident pulse energy values of superficial spots with a minimum diameter of 140 nm, significantly smaller than the 900 nm diffraction limited spot for the laser wavelength at 1027 nm and the focusing microscope objective with 0.55 NA.

Applications in laser microprocessing of materials

- The studied applications of ultrashort pulse laser processing of advanced materials substantially benefited from the focusing control provided by the z-scan focusing method, which allowed their processing with high spatial accuracy and definition.

- Laser ablation of PLA through laser pulse accumulation for profound hole production showed remarkable results consisting in the obtention of very well defined and smooth holes reaching depths of 500 μm with 15 μm diameter and promising possibilities for through-hole complete perforation.

- Self-focusing of the propagating laser pulses inside the holes was the mechanism accounting for the profound depth obtained though laser pulse accumulation. However, it can lead to detrimental bending effects that must be prevented and overcome for the obtention of satisfactory results.

- Superficial modification through irradiation with ultrashort laser pulses at different wavelengths of a biodegradable polymer like PLGA showed improved biodegradability for the wavelength of 266 nm and specially at 400 nm in comparison with the processing at 800 nm.

- Controlled size leaks with equivalent diameters of 10, 20 and 30 μm could be successfully fabricated thanks to the perforation of the processed medical use polypropylene bags through laser pulse accumulation.

- The focusing strategy used during the generation of leaks in polypropylene bags also made possible the in situ detection of leak formation, verifying the complete perforation of the bag surface.

- Irregular shapes and inner material alterations observed in the optical microscopy images of the produced leaks were favorable for their final goal, which is replicating leaks naturally occurring in the medical consumables. The controlled size of the leaks make possible their use for calibration of leak detection systems.

- The printing of liquid inks through LIFT inside laser ablated fluidic guides was propitiously implemented for the fabrication of conductive lines free from the most common printing defects, specially bulging and scalloping.

Well defined patterns following challenging geometries could be fabricated with the developed strategy.

6 Conclusions en català

Les següents conclusions es poden extreuen dels principals resultats obtinguts durant el desenvolupament d'aquesta tesi doctoral, en la que s'han assolit els objectius plantejats.

- S'ha dissenyat i posat en funcionament un muntatge experimental automatitzat i ràpid d'escriptura directa que inclou un làser d'impulsos ultracurts per al microprocessament de diferents tipus de materials.

Mètode d'enfocament per z-scan

- L'estratègia ideada per fer servir les mesures de transmitància in-situ durant el z-scan com a tècnica per mantenir el control sobre les condicions experimentals d'enfocament s'ha demostrat exitosa com a mètode per situar efectivament i precisa materials transparents a la cintura del feix làser per processar-ne la seva superfície.

- El mètode d'enfocament per z-scan s'ha caracteritzat per diferents posicions sobre l'eix z de propagació del feix làser. L'anàlisi de l'ablació superficial produïda al llarg d'aquestes diferents posicions sobre l'eix z ha fet possible determinar de manera precisa el rang de posicions òptimes per induir l'ablació a la superfície d'un material transparent com el PMMA. Aquest rang s'estén entre 3 i 4 μm per a valors intermedis d'energia dels impulsos làser.

- L'anàlisi de l'ablació superficial produïda també ha fet possible la identificació de diferents rangs de posicions sobre l'eix z depenent de l'ablació superficial induïda. Una ablació estrictament superficial s'ha obtingut només en posicions z corresponents a la situació en la qual la superfície de la mostra comença a entrar en la regió de la cintura del feix làser. S'ha observat que el posicionament de la mostra en aquestes posicions és bastant crític. És per això que per a una ablació superficial més fiable i regular en la forma i dimensions

dels punts creats, la mostra s'ha de situar al llarg de la zona intermèdia de la corba de transmitància dels z-scans. S'ha observat que els punts processats patien una expansió en forma de protuberàncies per les posicions sobre l'eix z corresponents a la cintura del feix làser localitzada a dins del material però encara a prop de la superfície. No s'ha observat cap modificació superficial quan la cintura del feix làser es troba ben endins del material.

- L'observació mitjançant processament FIB de la secció transversal produïda per un únic impuls làser ha revelat que en certes ocasions es troba una estructura porosa al volum del material situat directament a sota dels punts produïts. La seva presència té relació amb l'expansió del material vaporitzat dins la mostra, que comporta dimensions finals superiors dels punts processats.

- La correspondència entre els resultats experimentals i els resultats predits per les dades calculades amb les simulacions amb teoria de difracció vectorial del perfil del feix làser juntament amb els valors mesurats de transmitància ha fet possible identificar la posició z òptima per situar la cintura del feix làser a la superfície de la mostra.

- Resultats similars per controlar les condicions d'enfocament amb la tècnica d'enfocament per z-scan s'han obtingut en la producció de microcanals a la superfície del PMMA mitjançant el rastreig làser. El control de la inclinació de la superfície de la mostra respecte a la direcció de propagació del feix làser assegura l'ablació de la superfície al llarg de grans àrees de la mostra. Canals continus amb amplades i profunditats per sota d'1 µm han pogut ser fabricats gràcies al control de l'enfocament proveït al llarg del recorregut total sobre la mostra de 2 mm.

- Degut a l'acumulació d'impulsos i la superposició durant la producció de microcanals mitjançant el rastreig làser, expansions de la superfície en forma de línies de protuberàncies consecutives s'han observat en dues condicions experimentals diferents: quan la superfície de la mostra comença a entrar a la regió de la cintura del feix làser i quan la cintura del feix làser es troba completament dins del material però encara propera a la seva superfície.

- Mesures simultànies de la transmitància i la reflectància han fet possible controlar la posició de la mostra respecte la cintura del feix làser durant els experiments d'ablació superficial.

- El control de la posició d'enfocament que dona la tècnica d'enfocament per z-scan fa possible l'obtenció, tot i els diferents valors d'energia incident dels impulsos, de punts superficials amb un diàmetre mínim de 140 nm, considerablement inferiors al valor del diàmetre de l'àrea associada a la limitació per difracció, que pren un valor de 900 nm amb la longitud d'ona del làser de 1027 nm i l'enfocament de l'objectiu del microscopi amb 0.55 NA.

Aplicacions en la microprocessament de materials amb làser

- Les aplicacions estudiades de processament amb impulsos làser ultracurts de materials avançats es beneficien de forma substancial del control de l'enfocament que aporta la tècnica d'enfocament per z-scan, que permet el seu processament amb una definició i precisió espacial superior.

- L'ablació làser del PLA mitjançant acumulació d'impulsos làser per produir forats profunds mostra resultats destacables consistents en l'obtenció de forats llisos i molt ben definits amb profunditats de fins a 500 μm amb diàmetres de 15 μm i amb possibilitats molt prometedores per a la completa perforació a través de tot el gruix de les mostres processades.

- L'auto-enfocament dels impulsos làser que es propaguen dins els forats és el mecanisme que explica la notable profunditat obtinguda mitjançant l'acumulació d'impulsos làser. Encara i així, això pot portar a certs efectes de desviament perjudicials que s'han de prevenir i superar per tal d'obtenir resultats satisfactoris.

- La modificació superficial mitjançant la irradiació amb impulsos làser ultracurts en diferents longituds d'ona d'un polímer biodegradable com el PLGA mostra una biodegradabilitat millorada en longituds d'ona com a 266 nm i especialment a 400 nm en comparació al processament amb longitud d'ona a 800 nm.

- Forats de fuites de mides controlades amb diàmetres equivalents a 10, 20 i 30 μm han pogut ser realitzats satisfactòriament en bosses de polipropilè mitjançant l'acumulació d'impulsos làser.

- Les formes irregulars i alteracions internes del material observades en imatges de microscòpia òptica dels forats de fuita produïts són favorables per al

seu objectiu final, que és replicar les fuites que apareixen espontàniament en productes mèdics. La mida controlada dels forats de fuita fa possible el seu ús com a calibratge de sistemes de detecció de fuites.

- La impressió de tintes líquides mitjançant LIFT dins de guies fluídiques fetes per ablació amb làser ha estat implementada favorablement per a la fabricació de línies conductores lliures dels defectes més comuns en impressió, especialment la formació de bonys i les ondulacions del contorn de les línies. Patrons ben definits seguint geometries complexes han pogut ser fabricats amb l'estratègia desenvolupada.

Bibliography

[1] R. Chau, B. Doyle, S. Datta, J. Kavalieros, and K. Zhang, "Integrated nano-electronics for the future," *Nature Materials*, vol. 6, pp. 810–812, 2007.

[2] A. Hierlemann, O. Brand, C. Hagleitner, and H. Baltes, "Microfabrication techniques for chemical/biosensors," *Proceedings of the IEEE*, vol. 91, pp. 839–863, 2003.

[3] Y. Song, J. Hormes, and C. S. S. R. Kumar, "Microfluidic synthesis of nano-materials," *Small*, vol. 4, pp. 698–711, 2008.

[4] E. W. Esch, A. Bahinski, and D. Huh, "Organs-on-chips at the frontiers of drug discovery," *Nature Reviews Drug Discovery*, vol. 14, pp. 248–260, 2015.

[5] D. B. Weibel, W. R. DiLuzio, and G. M. Whitesides, "Microfabrication meets microbiology," *Nature Reviews Microbiology*, vol. 5, pp. 209–218, 2007.

[6] K. Paul, M. Prentiss, and G. Whitesides, "Patterning spherical surfaces at the two-hundred-nanometer scale using soft lithography," *Advanced Functional Materials*, vol. 13, pp. 259–263, 2003.

[7] C. G. Khan Malek, "Laser processing for bio-microfluidics applications (part II)," *Analytical and Bioanalytical Chemistry*, vol. 385, pp. 1362–1369, 2006.

[8] J. L. Wilbur, A. Kumar, E. Kim, and G. M. Whitesides, "Microfabrication by microcontact printing of self-assembled monolayers," *Advanced Materials*, vol. 6, pp. 600–604, 1994.

[9] A. Perl, D. N. Reinhoudt, and J. Huskens, "Microcontact printing: limitations and achievements," *Advanced Materials*, vol. 21, pp. 2257–2268, 2009.

[10] H. Mekaru, T. Yamada, S. Yan, and T. Hattori, "Microfabrication by hot embossing and injection molding at LASTI," *Microsystem Technologies*, vol. 10, pp. 682–688, 2004.

[11] L. Peng, Y. Deng, P. Yi, and X. Lai, "Micro hot embossing of thermoplastic polymers: a review," *Journal of Micromechanics and Microengineering*, vol. 24, p. 013001, 2014.

[12] A. Pimpin and W. Srituravanich, "Review on Micro- and Nanolithography Techniques and their Applications," *Engineering Journal*, vol. 16, pp. 37–56, 2012.

[13] P. van Assenbergh, E. Meinders, J. Geraedts, and D. Dodou, "Nanostructure and Microstructure Fabrication: From Desired Properties to Suitable Processes," *Small*, vol. 14, p. 1703401, 2018.

[14] S. Y. Chou, P. R. Krauss, W. Zhang, L. Guo, and L. Zhuang, "Sub-10 nm imprint lithography and applications," *Journal of Vacuum Science & Technology B: Microelectronics and Nanometer Structures*, vol. 15, p. 2897, 1997.

[15] J. G. Kim, Y. Sim, Y. Cho, J. W. Seo, S. Kwon, J. W. Park, H. G. Choi, H. Kim, and S. Lee, "Large area pattern replication by nanoimprint lithography for LCD-TFT application," *Microelectronic Engineering*, vol. 86, pp. 2427–2431, 2009.

[16] C. B. Arnold, P. Serra, and A. Piqué, "Laser direct-write techniques for printing of complex materials," *MRS Bulletin*, vol. 32, pp. 23–31, 2007.

[17] P. Tseng, C. Murray, D. Kim, and D. Di Carlo, "Research highlights: printing the future of microfabrication," *Lab on a Chip*, vol. 14, p. 1491, 2014.

[18] B. Derby, "Inkjet printing of functional and structural materials: fluid property requirements, feature stability, and resolution," *Annual Review of Materials Research*, vol. 40, pp. 395–414, 2010.

[19] J. Bohandy, B. F. Kim, and F. J. Adrian, "Metal deposition from a supported metal film using an excimer laser," *Journal of Applied Physics*, vol. 60, pp. 1538–1539, 1986.

[20] J. C. Miller, *Laser ablation*, vol. 28 of *Springer Series in Materials Science*. Berlin, Heidelberg: Springer Berlin Heidelberg, 1994.

[21] A. Ostendorf and B. N. Chichkov, "Two-photon polymerization: a new approach to micromachining," *Photonics Spectra*, vol. 40, pp. 72–79, 2006.

[22] R. J. Young, "Micro-machining using a focused ion beam," *Vacuum*, vol. 44, pp. 353–356, 1993.

[23] G. Cummins and M. P. Desmulliez, "Inkjet printing of conductive materials: a review," *Circuit World*, vol. 38, pp. 193–213, 2012.

[24] D. Jang, D. Kim, and J. Moon, "Influence of fluid physical properties on ink-jet printability," *Langmuir*, vol. 25, pp. 2629–2635, 2009.

[25] D. Soltman and V. Subramanian, "Inkjet-printed line morphologies and temperature control of the coffee ring effect," *Langmuir*, vol. 24, pp. 2224–2231, 2008.

[26] A. Lee, K. Sudau, K. H. Ahn, S. J. Lee, and N. Willenbacher, "Optimization of experimental parameters to suppress nozzle clogging in inkjet printing," *Industrial & Engineering Chemistry Research*, vol. 51, pp. 13195–13204, 2012.

[27] P. Serra and A. Piqué, "Laser-Induced Forward Transfer: Fundamentals and Applications," *Advanced Materials Technologies*, vol. 4, p. 1800099, 2019.

[28] R. J. Baseman, N. M. Froberg, J. C. Andreshak, and Z. Schlesinger, "Minimum fluence for laser blow-off of thin gold films at 248 and 532 nm," *Applied Physics Letters*, vol. 56, pp. 1412–1414, 1990.

[29] V. Schultze and M. Wagner, "Laser-induced forward transfer of aluminium," *Applied Surface Science*, vol. 52, pp. 303–309, 1991.

[30] Z. Kántor, Z. Tóth, and T. Szörényi, "Laser induced forward transfer: the effect of support-film interface and film-to-substrate distance on transfer," *Applied Physics A: Materials Science & Processing*, vol. 54, pp. 170–175, 1992.

[31] Q. Li, D. Grojo, A.-P. Alloncle, B. Chichkov, and P. Delaporte, "Digital laser micro- and nanoprinting," *Nanophotonics*, vol. 8, pp. 27–44, 2018.

[32] Z. Tóth, T. Szörényi, and A. Tóth, "Ar+ laser-induced forward transfer (lift): a novel method for micrometer-size surface patterning," *Applied Surface Science*, vol. 69, pp. 317–320, 1993.

[33] J. A. Greer and T. E. Parker, "Laser-induced forward transfer of metal oxides to trim the frequency of surface acoustic wave resonator devices," *Proc. SPIE, Excimer Beam Applications*, vol. 998, pp. 113–125, 1988.

[34] I. Zergioti, D. Papazoglou, A. Karaiskou, N. Vainos, and C. Fotakis, "Laser microprinting of inox active optical structures and time resolved imaging of the transfer process," *Applied Surface Science*, vol. 197–198, pp. 868–872, 2002.

[35] K. S. Kaur, R. Fardel, T. C. May-Smith, M. Nagel, D. P. Banks, C. Grivas, T. Lippert, and R. W. Eason, "Shadowgraphic studies of triazene assisted laser-induced forward transfer of ceramic thin films," *Journal of Applied Physics*, vol. 105, p. 113119, 2009.

[36] W. A. Toldbert, I.-Y. S. Lee, M. M. Doxtader, E. W. Ellis, and D. D. Dlott, "High-speed color imaging by laser ablation transfer with a dynamic release layer: Fundamental mechanisms," *Journal of Imaging Science*, vol. 37, pp. 411–421, 1993.

[37] A. Doraiswamy, R. Narayan, T. Lippert, L. Urech, A. Wokaun, M. Nagel, B. Hopp, M. Dinescu, R. Modi, R. Auyeung, and D. Chrisey, "Excimer laser forward transfer of mammalian cells using a novel triazene absorbing layer," *Applied Surface Science*, vol. 252, pp. 4743–4747, 2006.

[38] R. Fardel, M. Nagel, F. Nüesch, T. Lippert, and A. Wokaun, "Laser forward transfer using a sacrificial layer: Influence of the material properties," *Applied Surface Science*, vol. 254, pp. 1322–1326, 2007.

[39] S. H. Ko, H. Pan, S. G. Ryu, N. Misra, C. P. Grigoropoulos, and H. K. Park, "Nanomaterial enabled laser transfer for organic light emitting material direct writing," *Applied Physics Letters*, vol. 93, p. 151110, 2008.

[40] N. T. Kattamis, N. D. McDaniel, S. Bernhard, and C. B. Arnold, "Laser direct write printing of sensitive and robust light emitting organic molecules," *Applied Physics Letters*, vol. 94, p. 103306, 2009.

[41] M. Duocastella, J. M. Fernández-Pradas, J. L. Morenza, and P. Serra, "Sessile droplet formation in the laser-induced forward transfer of liquids: a time-resolved imaging study," *Thin Solid Films*, vol. 518, pp. 5321–5325, 2010.

[42] A. Palla-Papavlu, M. Dinescu, A. Wokaun, and T. Lippert, "Laser-induced forward transfer of single-walled carbon nanotubes," *Applied Physics A Materials Science & Processing*, vol. 117, pp. 371–376, 2014.

[43] P. Wu, B. Ringeisen, J. Callahan, M. Brooks, D. Bubb, H. Wu, A. Piqué, B. Spargo, R. McGill, and D. Chrisey, "The deposition, structure, pattern deposition, and activity of biomaterial thin-films by matrix-assisted pulsed-laser evaporation (MAPLE) and MAPLE direct write," *Thin Solid Films*, vol. 398-399, pp. 607–614, 2001.

[44] P. Serra, M. Colina, J. M. Fernández-Pradas, L. Sevilla, and J. L. Morenza, "Preparation of functional DNA microarrays through laser-induced forward transfer," *Applied Physics Letters*, vol. 85, pp. 1639–1641, 2004.

[45] M. Duocastella, J. M. Fernández-Pradas, J. Domínguez, P. Serra, and J. L. Morenza, "Printing biological solutions through laser-induced forward transfer," *Applied Physics A Materials Science & Processing*, vol. 93, pp. 941–945, 2008.

[46] A. Palla-Papavlu, V. Dinca, C. Luculescu, J. Shaw-Stewart, M. Nagel, T. Lippert, and M. Dinescu, "Laser induced forward transfer of soft materials," *Journal of Optics*, vol. 12, p. 124014, 2010.

[47] A. Palla-Papavlu, A. Patrascioiu, F. Di Pietrantonio, J. M. Fernández-Pradas, D. Cannatà, M. Benetti, S. D'Auria, E. Verona, and P. Serra, "Preparation of surface acoustic wave odor sensors by laser-induced forward transfer," *Sensors and Actuators B: Chemical*, vol. 192, pp. 369–377, 2014.

[48] F. Guillemot, A. Souquet, S. Catros, B. Guillotin, J. Lopez, M. Faucon, B. Pippenger, R. Bareille, M. Rémy, S. Bellance, P. Chabassier, J. Fricain, and J. Amédée, "High-throughput laser printing of cells and biomaterials for tissue engineering," *Acta Biomaterialia*, vol. 6, pp. 2494–2500, 2010.

[49] I. A. Paun, M. Zamfirescu, M. Mihailescu, C. R. Luculescu, C. C. Mustaciosu, I. Dorobantu, B. Calenic, and M. Dinescu, "Laser micro-patterning of biodegradable polymer blends for tissue engineering," *Journal of Materials Science*, vol. 50, pp. 923–936, 2015.

[50] C. B. Arnold, T. Sutto, H. Kim, and A. Piqué, "Direct-write laser processing creates tiny electrochemical systems," *Laser Focus World*, vol. 40, p. S9, 2004.

[51] N. T. Kattamis, P. E. Purnick, R. Weiss, and C. B. Arnold, "Thick film laser induced forward transfer for deposition of thermally and mechanically sensitive materials," *Applied Physics Letters*, vol. 91, p. 171120, 2007.

[52] C. Boutopoulos, V. Tsouti, D. Goustouridis, S. Chatzandroulis, and I. Zergioti, "Liquid phase direct laser printing of polymers for chemical sensing applications," *Applied Physics Letters*, vol. 93, p. 191109, 2008.

[53] M. Baum, H. Kim, I. Alexeev, A. Piqué, and M. Schmidt, "Generation of transparent conductive electrodes by laser consolidation of LIFT printed ITO nanoparticle layers," *Applied Physics A: Materials Science & Processing*, vol. 111, pp. 799–805, 2013.

[54] G. B. Blanchet, Y.-L. Loo, J. A. Rogers, F. Gao, and C. R. Fincher, "Large area, high resolution, dry printing of conducting polymers for organic electronics," *Applied Physics Letters*, vol. 82, pp. 463–465, 2003.

[55] N. T. Kattamis, N. D. McDaniel, S. Bernhard, and C. B. Arnold, "Ambient laser direct-write printing of a patterned organo-metallic electroluminescent device," *Organic Electronics*, vol. 12, pp. 1152–1158, 2011.

[56] J. Shaw-Stewart, T. Mattle, T. Lippert, M. Nagel, F. Nüesch, and A. Wokaun, "The optimisation of the laser-induced forward transfer process for fabrication of polyfluorene-based organic light-emitting diode pixels," *Applied Surface Science*, vol. 278, pp. 341–346, 2013.

[57] H. Kim, R. C. Y. Auyeung, S. H. Lee, a. L. Huston, and a. Piqué, "Laser-printed interdigitated Ag electrodes for organic thin film transistors," *Journal of Physics D: Applied Physics*, vol. 43, p. 085101, 2010.

[58] L. Rapp, J. Ailuno, A. P. Alloncle, and P. Delaporte, "Pulsed-laser printing of silver nanoparticles ink: control of morphological properties," *Optics Express*, vol. 19, pp. 21563–21574, 2011.

[59] I. Zergioti, "Laser printing of organic electronics and sensors," *Journal of Laser Micro/Nanoengineering*, vol. 8, pp. 30–34, 2013.

[60] E. Biver, L. Rapp, A.-P. Alloncle, and P. Delaporte, "Multi-jets formation using laser forward transfer," *Applied Surface Science*, vol. 302, pp. 153–158, 2014.

[61] A. Palla-Papavlu, C. Córdoba, A. Patrascioiu, J. M. Fernández-Pradas, J. L. Morenza, and P. Serra, "Deposition and characterization of lines printed through laser-induced forward transfer," *Applied Physics A Materials Science & Processing*, vol. 110, pp. 751–755, 2013.

[62] H. Kim, R. C. Y. Auyeung, S. H. Lee, a. L. Huston, and A. Piqué, "Laser forward transfer of silver electrodes for organic thin-film transistors," *Applied Physics A*, vol. 96, pp. 441–445, 2009.

[63] S. A. Mathews, R. C. Y. Auyeung, H. Kim, N. A. Charipar, and A. Piqué, "High-speed video study of laser-induced forward transfer of silver nanosuspensions," *Journal of Applied Physics*, vol. 114, p. 064910, 2013.

[64] R. L. Kubena, "A low magnification focused ion beam system with 8 nm spot size," *Journal of Vacuum Science & Technology B: Microelectronics and Nanometer Structures*, vol. 9, p. 3079, 1991.

[65] K. Thyagarajan and A. Ghatak, *Lasers, fundamentals and applications*. Graduate Texts in Physics, Boston, MA: Springer US, 2011.

[66] M. von Allmen, *Laser-beam interactions with materials*, vol. 2 of *Springer Series in Materials Science*. Berlin, Heidelberg: Springer Berlin Heidelberg, 1987.

[67] C. B. Schaffer, A. Brodeur, and E. Mazur, "Laser-induced breakdown and damage in bulk transparent materials induced by tightly focused femtosecond laser pulses," *Measurement Science and Technology*, vol. 12, pp. 1784–1794, 2001.

[68] S. H. Chung and E. Mazur, "Femtosecond laser ablation of neurons in c. elegans for behavioral studies," *Applied Physics A: Materials Science & Processing*, vol. 96, pp. 335–341, 2009.

[69] A. K. Dharmadhikari, J. a. Dharmadhikari, and D. Mathur, "Visualization of focusing–refocusing cycles during filamentation in BaF2," *Applied Physics B*, vol. 94, pp. 259–263, 2009.

[70] R. R. Gattass and E. Mazur, "Femtosecond laser micromachining in transparent materials," *Nature Photonics*, vol. 2, pp. 219–225, 2008.

[71] K. C. Phillips, H. H. Gandhi, E. Mazur, and S. K. Sundaram, "Ultrafast laser processing of materials: a review," *Advances in Optics and Photonics*, vol. 7, pp. 684–712, 2015.

[72] H. Becker and C. Gärtner, "Polymer microfabrication technologies for microfluidic systems," *Analytical and Bioanalytical Chemistry*, vol. 390, pp. 89–111, 2008.

[73] L. Rusen, M. Cazan, C. Mustaciosu, M. Filipescu, S. Sandel, M. Zamfirescu, V. Dinca, and M. Dinescu, "Tailored topography control of biopolymer surfaces by ultrafast lasers for cell–substrate studies," *Applied Surface Science*, vol. 302, pp. 256–261, 2014.

[74] A. Vogel and V. Venugopalan, "Mechanisms of pulsed laser ablation of biological tissues," *Chemical reviews*, vol. 103, pp. 577–644, 2003.

[75] K. Sugioka, "Progress in ultrafast laser processing and future prospects," *Nanophotonics*, vol. 6, pp. 393–413, 2017.

[76] C. De Marco, R. Suriano, M. Levi, S. Turri, S. Eaton, G. Cerullo, and R. Osellame, "Femtosecond laser fabrication and characterization of microchannels and waveguides in methacrylate-based polymers," *Microsystem Technologies*, vol. 18, pp. 183–190, 2012.

[77] E. N. Glezer, M. Milosavljevic, L. Huang, R. J. Finlay, T. H. Her, J. P. Callan, and E. Mazur, "Three-dimensional optical storage inside transparent materials." *Optics Letters*, vol. 21, pp. 2023–2025, 1996.

[78] Y. Hu, Y. Chen, J. Li, D. Hu, J. Chu, Q. Zhang, and W. Huang, "Femtosecond laser induced surface deformation in multi-dimensional data storage," *Applied Physics Letters*, vol. 101, p. 251116, 2012.

[79] R. Osellame, H. Hoekstra, G. Cerullo, and M. Pollnau, "Femtosecond laser microstructuring: an enabling tool for optofluidic lab-on-chips," *Laser & Photonics Reviews*, vol. 5, pp. 442–463, 2011.

[80] Y. Li, K. Itoh, W. Watanabe, K. Yamada, D. Kuroda, J. Nishii, and Y. Jiang, "Three-dimensional hole drilling of silica glass from the rear surface with femtosecond laser pulses," *Optics Letters*, vol. 26, p. 1912, 2001.

[81] Y. Liao, Y. Ju, L. Zhang, F. He, Q. Zhang, Y. Shen, D. Chen, Y. Cheng, Z. Xu, K. Sugioka, and K. Midorikawa, "Three-dimensional microfluidic channel with arbitrary length and configuration fabricated inside glass by femtosecond laser direct writing," *Optics Letters*, vol. 35, p. 3225, 2010.

[82] Y. Liao, J. Song, E. Li, Y. Luo, Y. Shen, D. Chen, Y. Cheng, Z. Xu, K. Sugioka, and K. Midorikawa, "Rapid prototyping of three-dimensional microfluidic mixers in glass by femtosecond laser direct writing," *Lab on a Chip*, vol. 12, p. 746, 2012.

[83] J. M. Fernández-Pradas, D. Serrano, J. L. Morenza, and P. Serra, "Microchannel formation through Foturan® with infrared femtosecond and ultraviolet nanosecond lasers," *Journal of Micromechanics and Microengineering*, vol. 21, p. 025005, 2011.

[84] J. Fernández-Pradas, D. Serrano, S. Bosch, J. Morenza, and P. Serra, "3D features of modified photostructurable glass–ceramic with infrared femtosecond laser pulses," *Applied Surface Science*, vol. 257, pp. 5219–5222, 2011.

[85] Y. Cheng, K. Sugioka, K. Midorikawa, M. Masuda, K. Toyoda, M. Kawachi, and K. Shihoyama, "Control of the cross-sectional shape of a hollow microchannel embedded in photostructurable glass by use of a femtosecond laser," *Optics letters*, vol. 28, pp. 55–57, 2003.

[86] F. He, H. Sun, M. Huang, J. Xu, Y. Liao, Z. Zhou, Y. Cheng, Z. Xu, K. Sugioka, and K. Midorikawa, "Rapid fabrication of optical volume gratings in Foturan glass by femtosecond laser micromachining," *Applied Physics A*, vol. 97, pp. 853–857, 2009.

[87] F. He, Y. Cheng, J. Lin, J. Ni, Z. Xu, K. Sugioka, and K. Midorikawa, "Independent control of aspect ratios in the axial and lateral cross sections of a focal spot for three-dimensional femtosecond laser micromachining," *New Journal of Physics*, vol. 13, p. 083014, 2011.

[88] S. M. Eaton, C. De Marco, R. Martinez-Vazquez, R. Ramponi, S. Turri, G. Cerullo, and R. Osellame, "Femtosecond laser microstructuring for polymeric lab-on-chips.," *Journal of biophotonics*, vol. 5, pp. 687–702, 2012.

[89] F. Sima, K. Sugioka, R. M. Vázquez, R. Osellame, L. Kelemen, and P. Ormos, "Three-dimensional femtosecond laser processing for lab-on-a-chip applications," *Nanophotonics*, vol. 7, pp. 613–634, 2018.

[90] C. G. Khan Malek, "Laser processing for bio-microfluidics applications (part I)," *Analytical and Bioanalytical Chemistry*, vol. 385, pp. 1351–1361, 2006.

[91] A. Kurella, "Review paper: surface modification for bioimplants: the role of laser surface engineering," *Journal of Biomaterials Applications*, vol. 20, pp. 5–50, 2005.

[92] Z. Wang, R. Zhou, F. Wen, R. Zhang, L. Ren, S. H. Teoh, and M. Hong, "Reliable laser fabrication: the quest for responsive biomaterials surface," *Journal of Materials Chemistry B*, vol. 6, pp. 3612–3631, 2018.

[93] Y. Ou, Q. Yang, F. Chen, Z. Deng, G. Du, J. Wang, H. Bian, J. Yong, and X. Hou, "Direct fabrication of microlens arrays on PMMA with laser-induced structural modification," *IEEE Photonics Technology Letters*, vol. 27, pp. 2253–2256, 2015.

[94] M. T. B. Najam, K. M. Arif, and Y.-G. Lee, "Novel method for laser focal point positioning on the cover slip for TPP-based microfabrication and detection of the cured structure under optical microscope," *Applied Physics B*, vol. 111, pp. 141–147, 2013.

[95] M. Antti, H. Ville, and V. Jorma, "Precise online auto-focus system in high speed laser micromachining applications," *Physics Procedia*, vol. 39, pp. 807–813, 2012.

[96] S. Campbell, F. C. Dear, D. P. Hand, and D. T. Reid, "Single-pulse femtosecond laser machining of glass," *Journal of Optics A: Pure and Applied Optics*, vol. 7, pp. 162–168, 2005.

[97] W. T. Silfvast, *Laser fundamentals*. Cambridge University Press, 2nd ed., 2004.

[98] E. T. J. Nibbering, G. Grillon, M. A. Franco, B. S. Prade, A. Mysyrowicz, and O. Applique, "Determination of the inertial contribution to the nonlinear refractive index of air , N 2 , and O 2 by use of unfocused high-intensity femtosecond laser pulses NONLINEAR PROPAGATION THROUGH," *Journal of the Optical Society of America B*, vol. 14, pp. 650–660, 1997.

[99] E. Spyratou, I. Asproudis, D. Tsoutsi, C. Bacharis, K. Moutsouris, M. Makropoulou, and A. Serafetinides, "UV laser ablation of intraocular lenses: SEM and AFM microscopy examination of the biomaterial surface," *Applied Surface Science*, vol. 256, pp. 2539–2545, 2010.

[100] K. Yamasaki, S. Juodkazis, S. Matsuo, and H. Misawa, "Three-dimensional micro-channels in polymers: one-step fabrication," *Applied Physics A: Materials Science & Processing*, vol. 77, pp. 371–373, 2003.

[101] W. Watanabe, S. Sowa, T. Tamaki, K. Itoh, and J. Nishii, "Three-dimensional waveguides fabricated in poly(methyl methacrylate) by a femtosecond laser," *Japanese Journal of Applied Physics*, vol. 45, pp. L765–L767, 2006.

[102] R. Suriano, A. Kuznetsov, S. M. Eaton, R. Kiyan, G. Cerullo, R. Osellame, B. N. Chichkov, M. Levi, and S. Turri, "Femtosecond laser ablation of polymeric substrates for the fabrication of microfluidic channels," *Applied Surface Science*, vol. 257, pp. 6243–6250, 2011.

[103] Z. K. Wang, H. Y. Zheng, C. P. Lim, and Y. C. Lam, "Polymer hydrophilicity and hydrophobicity induced by femtosecond laser direct irradiation," *Applied Physics Letters*, vol. 95, p. 111110, 2009.

[104] Z. K. Wang, H. Y. Zheng, and Y. C. Lam, "Investigation on femtosecond laser irradiation energy in inducing hydrophobic polymer surfaces," *Applied Surface Science*, vol. 257, pp. 10427–10433, 2011.

[105] X. Ma, H. Huo, M. Wei, L. Wang, M. Shen, C. Barry, and J. Mead, "Enhanced protein binding on femtosecond laser ablated poly(methyl methacrylate) surfaces," *Applied Physics Letters*, vol. 98, pp. 2009–2012, 2011.

[106] S. H. Oh and J. H. Lee, "Hydrophilization of synthetic biodegradable polymer scaffolds for improved cell/tissue compatibility," *Biomedical Materials (Bristol)*, vol. 8, 2013.

[107] F. Alexis, "Factors affecting the degradation and drug-release mechanism of poly(lactic acid) and poly[(lactic acid)-co-(glycolic acid)]," *Polymer International*, vol. 54, pp. 36–46, 2005.

[108] R. A. Miller, J. M. Brady, and D. E. Cutright, "Degradation rates of oral resorbable implants (polylactates and polyglycolates): Rate modification with changes in PLA/PGA copolymer ratios," *Journal of Biomedical Materials Research*, vol. 11, pp. 711–719, 1977.

[109] F. Haghighat and S. A. H. Ravandi, "Mechanical properties and in vitro degradation of PLGA suture manufactured via electrospinning," *Fibers and Polymers*, vol. 15, pp. 71–77, 2014.

[110] H. Ito, A. Minami, H. Tanino, and T. Matsuno, "Fixation with poly-L-lactic acid screws in hip osteotomy: 68 hips followed for 18-46 months," *Acta Orthopaedica Scandinavica*, vol. 73, pp. 60–64, 2002.

[111] L. Wang, M. Cai, Y. Liu, T. Yang, Y. Zeng, Y. Zhang, Q. Li, B. Zhu, and G. Ma, "Polymer hydrophobicity regulates paclitaxel distribution in microspheres, release profile and cytotoxicity in vitro," *Powder Technology*, vol. 275, pp. 77–84, 2015.

[112] H. Gasmi, F. Danede, J. Siepmann, and F. Siepmann, "Does PLGA microparticle swelling control drug release? New insight based on single particle swelling studies," *Journal of Controlled Release*, vol. 213, pp. 120–127, 2015.

[113] C. Wang, K. Zhang, H. Wang, S. Xu, and C. C. Han, "Evaluation of biodegradability of poly (DL-lactic-co-glycolic acid) scaffolds for post-surgical adhesion prevention: In vitro, in rats and in pigs," *Polymer (United Kingdom)*, vol. 61, pp. 174–182, 2015.

[114] P. Rychter, E. Pamula, A. Orchel, U. Posadowska, M. Krok-Borkowicz, A. Kaps, N. Smigiel-Gac, A. Smola, J. Kasperczyk, W. Prochwicz, and P. Dobrzynski, "Scaffolds with shape memory behavior for the treatment of large bone defects," *Journal of Biomedical Materials Research - Part A*, vol. 103, pp. 3503–3515, 2015.

[115] L. Pálfalvi, B. C. Tóth, G. Almási, J. a. Fülöp, and J. Hebling, "A general Z-scan theory," *Applied Physics B*, vol. 97, pp. 679–685, 2009.

[116] S. Lazare, A. Sionkowska, M. Zaborowicz, A. Planecka, J. Lopez, M. Dijoux, C. Louména, and M. C. Hernandez, "Bombyx mori silk protein films microprocessing with a nanosecond ultraviolet laser and a femtosecond laser workstation: Theory and experiments," *Applied Physics A: Materials Science and Processing*, vol. 106, pp. 67–77, 2012.

[117] D. F. Farson, H. W. Choi, B. Zimmerman, J. K. Steach, J. J. Chalmers, S. V. Olesik, and L. J. Lee, "Femtosecond laser micromachining of dielectric materials for biomedical applications," *Journal of Micromechanics and Microengineering*, vol. 18, p. 035020, 2008.

[118] J.-M. Guay, A. Villafranca, F. Baset, K. Popov, L. Ramunno, and V. R. Bhardwaj, "Polarization-dependent femtosecond laser ablation of poly-methyl methacrylate," *New Journal of Physics*, vol. 14, p. 085010, 2012.

[119] L. Shah, J. Tawney, M. Richardson, and K. Richardson, "Self-focusing during femtosecond micromachining of silicate glasses," *IEEE Journal of Quantum Electronics*, vol. 40, pp. 57–68, 2004.

[120] M. Miwa, S. Juodkazis, T. Kawakami, S. Matsuo, and H. Misawa, "Femtosecond two-photon stereo-lithography," *Applied Physics A Materials Science & Processing,* vol. 73, pp. 561–566, 2001.

[121] J. K. Koga, K. Moribayashi, Y. Fukuda, S. V. Bulanov, A. Sagisaka, K. Ogura, H. Daido, M. Yamagiwa, T. Kimura, T. Fujikawa, M. Ebina, and K. Akihama, "Simulation and experiments of the laser induced breakdown of air for femtosecond to nanosecond order pulses," *Journal of Physics D: Applied Physics*, vol. 43, p. 025204, 2010.

[122] S. Baudach, J. Bonse, J. Kruger, W. Kautek, J. Krüger, and W. Kautek, "Ultrashort pulse laser ablation of polycarbonate and polymethylmethacrylate," *Applied Surface Science*, vol. 154-155, pp. 555–560, 2000.

[123] J. Krüger, S. Martin, H. Mädebach, L. Urech, T. Lippert, A. Wokaun, and W. Kautek, "Femto- and nanosecond laser treatment of doped polymethylmethacrylate," *Applied Surface Science*, vol. 247, pp. 406–411, 2005.

[124] L. Novotny and B. Hecht, *Propagation and focusing of optical fields*, pp. 45–85. Cambridge University Press, 2 ed., 2012.

[125] G. D. Gillen, C. M. Seck, and S. Guha, "Analytical beam propagation model for clipped focused-Gaussian beams using vector diffraction theory," *Optics Express*, vol. 18, pp. 4024–4040, 2010.

[126] Y. Afanasiev, V. Isakov, I. Zavestovskaya, B. Chichkov, F. Von Alvensleben, and H. Welling, "Hydrodynamic model for UV laser ablation of polymers," *Laser and Particle Beams*, vol. 17, pp. 561–572, 1999.

[127] S.-S. Wellershoff, J. Hohlfeld, J. Güdde, and E. Matthias, "The role of electron–phonon coupling in femtosecond laser damage of metals," *Applied Physics A Materials Science & Processing*, vol. 69, pp. S99–S107, 1999.

[128] C. Momma, S. Nolte, B. N. Chichkov, F. v. Alvensleben, and A. Tünnermann, "Precise laser ablation with ultrashort pulses," *Applied Surface Science*, vol. 109-110, pp. 15–19, 1997.

[129] F. Baset, K. Popov, A. Villafranca, J.-M. Guay, Z. Al-Rekabi, A. E. Pelling, L. Ramunno, and R. Bhardwaj, "Femtosecond laser induced surface swelling in poly-methyl methacrylate," *Optics Express*, vol. 21, pp. 12527–12538, 2013.

[130] D. Gómez and I. Goenaga, "On the incubation effect on two thermoplastics when irradiated with ultrashort laser pulses: Broadening effects when machining microchannels," *Applied Surface Science*, vol. 253, pp. 2230–2236, 2006.

[131] K. Sugioka and Y. Cheng, "Femtosecond laser processing for optofluidic fabrication," *Lab on a chip*, vol. 12, pp. 3576–3589, 2012.

[132] F. Baset, A. Villafranca, J.-M. Guay, and R. Bhardwaj, "Femtosecond laser induced porosity in poly-methyl methacrylate," *Applied Surface Science*, vol. 282, pp. 729–734, 2013.

[133] E. Rebollar, J. R. Vázquez de Aldana, I. Martín-Fabiani, M. Hernández, D. R. Rueda, T. A. Ezquerra, C. Domingo, P. Moreno, and M. Castillejo, "Assessment of femtosecond laser induced periodic surface structures on polymer films.," *Physical Chemistry Chemical Physics*, vol. 15, pp. 11287–11298, 2013.

[134] M. Huang, F. Zhao, Y. Cheng, N. Xu, and Z. Xu, "Origin of laser-induced near-subwavelength ripples: interference between surface plasmons and incident laser.," *ACS nano*, vol. 3, pp. 4062–4070, 2009.

[135] T.-L. Chang, T.-K. Tsai, H.-P. Yang, and J.-Z. Huang, "Effect of ultra-fast laser texturing on surface wettability of microfluidic channels," *Microelectronic Engineering*, vol. 98, pp. 684–688, 2012.

[136] D. Teixidor, F. Orozco, T. Thepsonthi, J. Ciurana, C. a. Rodríguez, and T. Özel, "Effect of process parameters in nanosecond pulsed laser micromachining of PMMA-based microchannels at near-infrared and ultraviolet wavelengths," *The International Journal of Advanced Manufacturing Technology*, vol. 67, pp. 1651–1664, 2012.

[137] K. Sokolowski-Tinten and D. von der Linde, "Generation of dense electron-hole plasmas in silicon," *Physical Review B*, vol. 61, pp. 2643–2650, 2000.

[138] P. A. Danilov, A. A. Ionin, S. I. Kudryashov, S. V. Makarov, A. A. Rudenko, P. N. Saltuganov, L. V. Seleznev, V. I. Yurovskikh, D. A. Zayarny, and T. Apostolova, "Silicon as a virtual plasmonic material: Acquisition of its transient optical constants and the ultrafast surface plasmon-polariton excitation," *Journal of Experimental and Theoretical Physics*, vol. 120, pp. 946–959, 2015.

[139] A. E. Ongaro, I. Keraite, A. Liga, G. Conoscenti, S. Coles, H. Schulze, T. T. Bachmann, K. Parvez, C. Casiraghi, N. Howarth, V. La Carubba, and M. Kersaudy-Kerhoas, "Laser Ablation of Poly(lactic acid) Sheets for the Rapid Prototyping of Sustainable, Single-Use, Disposable Medical Microcomponents," *ACS Sustainable Chemistry & Engineering*, vol. 6, pp. 4899–4908, 2018.

[140] S. Döring, J. Szilagyi, S. Richter, F. Zimmermann, M. Richardson, A. Tünnermann, and S. Nolte, "Evolution of hole shape and size during short and ultrashort pulse laser deep drilling," *Optics Express*, vol. 20, p. 27147, 2012.

[141] T. V. Kononenko, V. I. Konov, S. V. Garnov, S. M. Klimentov, and F. Dausinger, "Dynamics of Deep Short Pulse Laser Drilling: Ablative Stages and Light Propagation," *Laser Physics*, vol. 11, pp. 343–351, 2001.

[142] B. Xia, L. Jiang, X. Li, X. Yan, and Y. Lu, "Mechanism and elimination of bending effect in femtosecond laser deep-hole drilling," *Optics Express*, vol. 23, p. 27853, 2015.

[143] L. Shah, J. Tawney, M. Richardson, and K. Richardson, "Femtosecond laser deep hole drilling of silicate glasses in air," *Applied Surface Science*, vol. 183, pp. 151–164, 2001.

[144] B. Stępak, M. Gazińska, M. Nejbauer, Y. Stepanenko, and A. Antończak, "Diverse nature of femtosecond laser ablation of poly(L-lactide) and the influence of filamentation on the polymer crystallization behaviour," *Scientific Reports*, vol. 9, p. 3069, 2019.

[145] A. Shibata, S. Yada, and M. Terakawa, "Biodegradability of poly(lactic-co-glycolic acid) after femtosecond laser irradiation," *Scientific Reports*, vol. 6, p. 27884, 2016.

[146] A. Shibata, M. Machida, N. Kondo, and M. Terakawa, "Biodegradability of poly(lactic-co-glycolic acid) and poly(l-lactic acid) after deep-ultraviolet femtosecond and nanosecond laser irradiation," *Applied Physics A*, vol. 123, p. 438, 2017.

[147] N. Kondo and M. Terakawa, "Biodegradability of poly(lactic-co-glycolic acid) irradiated with femtosecond laser pulses without material removal," *Applied Physics A*, vol. 125, p. 135, 2019.

[148] C. Florian, F. Caballero-Lucas, J. Fernández-Pradas, R. Artigas, S. Ogier, D. Karnakis, and P. Serra, "Conductive silver ink printing through the laser-induced forward transfer technique," *Applied Surface Science*, vol. 336, pp. 304–308, 2015.

[149] M. Duocastella, M. Colina, J. Fernández-Pradas, P. Serra, and J. Morenza, "Study of the laser-induced forward transfer of liquids for laser bioprinting," *Applied Surface Science*, vol. 253, pp. 7855–7859, 2007.

[150] J. M. Fernández-Pradas, D. Comas, J. L. Morenza, and P. Serra, "Irradiation of glass with infrared femtosecond laser pulses," *Applied Physics A*, vol. 112, pp. 203–207, 2013.

[151] D. A. Higgins, T. A. Everett, A. Xie, S. M. Forman, and T. Ito, "High-resolution direct-write multiphoton photolithography in poly(methylmethacrylate) films," *Applied Physics Letters*, vol. 88, p. 184101, 2006.

Publications

The developed work has resulted in the publication of eight research papers in scientific journals. Their references are given in the following lines of this section.

Paper 1 - J.M. Fernández-Pradas, C. Florian, F. Caballero-Lucas, J.L. Morenza, P. Serra. "Femtosecond laser ablation of polymethyl-methacrylate with high focusing control," *Applied Surface Science* **278** 185-189 (2013).
Impact factor JDR 2013: 2.538 - (Q1).

Paper 2 - C. Florian, F. Caballero-Lucas, J.M. Fernández-Pradas, J.L. Morenza, P. Serra. "Surface ablation of transparent polymers with femtosecond laser pulses," *Applied Surface Science* **302** 226-230 (2014).
Impact factor JDR 2014: 2.711 - (Q1).

Paper 3 - C. Florian, F. Caballero-Lucas, J.M. Fernández-Pradas, R. Artigas, S. Ogier, D. Karnakis, P. Serra. "Conductive silver ink printing through the laser-induced forward transfer technique," *Applied Surface Science* **336** 304-308 (2015).
Impact factor JDR 2015: 3.150 - (Q1).

Paper 4 - C. Florian, F. Caballero-Lucas, J.M. Fernández-Pradas, S. Bosch, J.L. Morenza, P. Serra. "Femtosecond laser surface ablation of polymethyl-methacrylate with position control through z-scan," *Journal of Physics D: Applied Physics* **48** 335302 (2015).
Impact factor JDR 2015: 2.772 - (Q1).

Paper 5 - F. Caballero-Lucas, C. Florian, J.M. Fernández-Pradas, J.L. Morenza, P. Serra. "Precise surface modification of polymethyl-methacrylate with near-infrared femtosecond laser," *Applied Surface Science* **336** 170-175 (2015).
Impact factor JDR 2015: 3.150 - (Q1).

Paper 6 - F. Caballero-Lucas, C. Florian, J.M. Fernández-Pradas, J.L. Morenza, P. Serra. "Beam waist position study for surface modification of polymethyl-methacrylate with femtosecond laser pulses," *Applied Surface Science* **374** 353-358 (2016).
Impact factor JDR 2016: 3.387 - (Q1).

Paper 7 - C. Florian, F. Caballero-Lucas, J.M. Fernández-Pradas, S. Ogier, L. Winchester, D. Karnakis, R. Artigas, P. Serra. "Printing of silver conductive lines through laser-induced forward transfer," *Applied Surface Science* **374** 265-270 (2016).
Impact factor JDR 2016: 3.387 - (Q1).

Paper 8 - J.M. Fernández-Pradas, C. Florian, F. Caballero-Lucas, P. Sopeña, J.L. Morenza, P. Serra. "Laser-induced forward transfer: Propelling liquids with light," *Applied Surface Science* **418** 559–564 (2017).
Impact factor JDR 2017: 4.439 - (Q1).

Curriculum Vitae

Francesc Caballero Lucas

PhD Candidate

Tel: +34 616 437 825 | francesc.caballero@gmail.com | Barcelona

Personal Information

Birth date: January 7, 1989

Birth place: Barcelona (Catalonia, Spain)

Education

2013 – Present	PhD Student in Nanosciences, Universitat de Barcelona, Physics Faculty, Department of Applied Physics, Barcelona (Catalonia, Spain).
2017	Research Internship: Study of the influence of laser irradiation in biodegradability. Supervised by Prof. Mitsuhiro Terakawa. Keio University, Department of Electronics and Electrical Engineering, Yokohama (Japan).
2012 – 2013	Master in Nanoscience and Nanotechnology, Universitat de Barcelona, Physics Faculty, Department of Applied Physics, Barcelona (Catalonia, Spain).
	Final grade: 9.0/10
	Thesis work: Femtosecond laser microfabrication in poly(methyl methacrylate)
	Advisor: Prof. Pere Serra Coromina
2007 – 2012	Bachelor in Physics, Universitat de Barcelona, Physics Faculty, Barcelona (Catalonia, Spain).
	Final grade: 8.24/10
2010 – 2011	Erasmus exchange student, Technische Universität München, Physics Department, Munich (Germany).
2005 – 2007	Scientific technical high school, Institució Pere Vergés, Badalona (Catalonia, Spain).
	Final grade: 10/10

Publications

J.M. Fernández-Pradas, C. Florian, F. Caballero-Lucas, P. Sopeña, J.L. Morenza, P. Serra, "Laser-induced forward transfer: Propelling liquids with light," Applied Surface Science, vol. 418, pp. 559-564, 2017.

F. Caballero-Lucas, C. Florian, J.M. Fernández-Pradas, J.L. Morenza, P. Serra, "Beam waist position study for surface modification of polymethyl-methacrylate with femtosecond laser pulses," Applied Surface Science, vol. 374, pp. 353–358, 2016.

C. Florian, F. Caballero-Lucas, J.M. Fernández-Pradas, S. Ogier, L. Winchester, D. Karnakis, R. Geremia, R. Artigas, P. Serra, "Printing of silver conductive lines through laser-induced forward transfer," Applied Surface Science, vol. 374, pp. 265–270, 2016.

C. Florian, F. Caballero-Lucas, J.M. Fernández-Pradas, S. Bosch, J.L. Morenza, P. Serra, "Femtosecond laser surface ablation of polymethyl-methacrylate with position control through z-scan," Journal of Physics D: Applied Physics, vol. 48, 335302, 2015.

C. Florian, F. Caballero-Lucas, J.M. Fernández-Pradas, R. Artigas, S. Ogier, D. Karnakis, P. Serra, "Conductive silver ink printing through the laser-induced forward transfer technique," Applied Surface Science, vol. 336, pp. 304-308, 2015.

F. Caballero-Lucas, C. Florian, J.M. Fernández-Pradas, J.L. Morenza, P. Serra, "Precise surface modification of polymethyl-methacrylate with near-infrared femtosecond laser," Applied Surface Science, vol. 336, pp. 170-175, 2015.

C. Florian, F. Caballero-Lucas, J. M. Fernández-Pradas, J.L. Morenza, P. Serra, "Surface ablation of transparent polymers with femtosecond laser pulses," Applied Surface Science, vol. 302, pp. 226–230, 2014.

J. M. Fernández-Pradas, C. Florian, F. Caballero-Lucas, J.L. Morenza, P. Serra, "Femtosecond laser ablation of polymethyl-methacrylate with high focusing control," Applied Surface Science, vol. 278, pp. 185–189, 2013.

Scolarships and Recognition

2014	Scholarship FPU for doctorate studies and teaching assistantship of the Education, Culture and Sport Ministry (MEC). Barcelona (Catalonia, Spain).
2013	Scholarship FI for doctorate studies of the University and Research Grant Management Agency (AGAUR). Barcelona (Catalonia, Spain).
2012	Collaboration grant with university departments of the Education Ministry (MEC). Barcelona (Catalonia, Spain).
2007	Scholarship for academic excellence of Caixa Manresa. Barcelona (Catalonia, Spain).
-	Honours registration by academic excellence. Full year. Universitat de Barcelona, Barcelona (Catalonia, Spain).

Conferences and Meetings

2016   Juan Marcos Fernández-Pradas, Camilo Florian, Francesc Caballero-Lucas, Pol Sopeña, José Luis Morenza, Pere Serra

Ink microprinting through laser-induced forward transfer

Contribution: Oral presentation

International Symposium "Fundamentals of Laser Assisted Micro- and Nanotechnologies" (FLAMN-16), Sant Petersburg, Russia

-    Juan Marcos Fernández-Pradas, Camilo Florian, Francesc Caballero-Lucas, Pol Sopeña, José Luis Morenza, Pere Serra

Laser direct-write methods for inks microprinting

Contribution: Oral presentation

International Conference on Small Science (ICSS), Prague, Czech Republic

-    Francesc Caballero-Lucas, Camilo Florian, Juan Marcos Fernández-Pradas, Simon Ogier, Lee Winchester, Dimitris Karnakis, Riccardo Geremia, Roger Artigas, Pere Serra

Laser printing in fluidic guides: production of high-resolution conductive lines through capillary flow along the guide

Contribution: Poster presentation

European Materials Research Society (E-MRS) Spring Meeting, Lille, France

- Camilo Florian, Francesc Caballero-Lucas, Pol Sopeña, Adrian Patrascioiu, Juan Marcos Fernández-Pradas, José Luis Morenza, Pere Serra

  Laser-induced forward transfer: propelling líquids with light

  Contribution: Oral presentation

  European Materials Research Society (E-MRS) Spring Meeting, Lille, France

2015 Francesc Caballero-Lucas, Camilo Florian, Juan Marcos Fernández-Pradas, José Luis Morenza, Pere Serra

  Control of beam waist position for surface modification of transparent materials with femtosecond laser pulses

  Contribution: Poster presentation

  European Materials Research Society (E-MRS) Spring Meeting, Lille, France

- Camilo Florian, Francesc Caballero-Lucas, Juan Marcos Fernández-Pradas, Simon Ogier, Lee Winchester, Dimitris Karnakis, Riccardo Geremia, Roger Artigas, Pere Serra

  Printing of silver conductive lines through laser-induced forward transfer

  Contribution: Oral presentation

  European Materials Research Society (E-MRS) Spring Meeting, Lille, France

- Dimitris Karnakis, Riccardo Geremia, Lee Winchester, Simon Ogier, Roger Artigas, Camilo Florian, Francesc Caballero-Lucas, Juan Marcos Fernández-Pradas, Pere Serra

  Laser-assisted conductive silver ink printing with inkjet and laser-induced forward transfer techniques for organic transistor fabrication

  Contribution: Oral presentation

  SPIE Photonics West, San Francisco, United States of America

2014 Francesc Caballero-Lucas, Camilo Florian , Juan Marcos Fernández-Pradas, José Luis Morenza, Pere Serra

  Precise surface modification of polymethyl-methacrylate with near-infrared femtosecond laser

  Contribution: Poster presentation

  European Materials Research Society (E-MRS) Spring Meeting, Lille, France

- Camilo Florian, Francesc Caballero-Lucas, Juan Marcos Fernández-Pradas, José Luis Morenza, Pere Serra

  Ag conductive ink printing through LIFT technique

  Contribution: Oral presentation

  European Materials Research Society (E-MRS) Spring Meeting, Lille, France

- Juan Marcos Fernández-Pradas, Adrian Patrascioiu, Camilo Florian, Francesc Caballero-Lucas, José Luis Morenza, Pere Serra

  Laser Transfer Methods for the Printing of Complex Materials from Liquid Suspensions

  Contribution: Oral presentation

  WCPT7, The 7th World Congress on Particle Technology, Beijing, China

2013 Camilo Florian, Francesc Caballero-Lucas, Juan Marcos Fernández-Pradas, José Luis Morenza, Pere Serra

  Femtosecond laser ablation of transparent polymer materials

  Contribution: Poster presentation

Conference On Laser Ablation (COLA), Ischia, Italia

- Francesc Caballero-Lucas, Camilo Florian , Juan Marcos Fernández-Pradas, José Luis Morenza, Pere Serra

  Study of the ablation of transparent materials with near-infrared femtosecond laser

  Contribution: Poster presentation

  Laser Advanced Materials Processing (LAMP), Niigata, Japan

- Camilo Florian, Francesc Caballero-Lucas, Juan Marcos Fernández-Pradas, José Luis Morenza, Pere Serra

  Surface laser ablation of polymethyl-methacrylate using 1027 nm femtosecond laser

  Contribution: Poster presentation

  Laser Advanced Materials Processing (LAMP), Niigata, Japan

- Juan Marcos Fernández-Pradas, Camilo Florian, Francesc Caballero-Lucas, José Luis Morenza, Pere Serra

  Surface ablation of transparent polymers with femtosecond laser pulses

  Contribution: Oral presentation

  European Materials Research Society (E-MRS) Spring Meeting, Strasbourg, France

Professional Experience

2017 Teaching Assistance, Electromagnetism Laboratory, Bachelor in Physics, Universitat de Barcelona, Barcelona (Catalonia, Spain).

- Teaching Assistance, Basic Laboratory for Engineering, Bachelor in Chemical Engineering, Universitat de Barcelona, Barcelona (Catalonia, Spain).

2016 Teaching Assistance, Laboratory Fundaments, Bachelor in Physics, Universitat de Barcelona, Barcelona (Catalonia, Spain).

- Teaching Assistance, Basic Laboratory for Engineering, Bachelor in Chemical Engineering, Universitat de Barcelona, Barcelona (Catalonia, Spain).

2015 Teaching Assistance, Electromagnetism Laboratory, Bachelor in Physics, Universitat de Barcelona, Barcelona (Catalonia, Spain).

2012 Assistant Student, Universitat de Barcelona, Physics Faculty, Department of Applied Physics, Barcelona (Catalonia, Spain).

2011 Assistant Student, PENeLOPE experiment, E18 research group in Particle Experimental Physics, Physics Department, Technische Universität München, Munich (Germany).

Languages

Catalan	Native Speaker
Spanish	Native Speaker
English	First Certificate in English (FCE): level B2
German	Goethe-Zertifikat C2: Großes Deutsches Sprachdiplom (GDS): level C2
Japanese	Advanced Level Certificate: level B2

Levels correspond to the Common European Framework of Reference (CEFR).

Computer Skills

OS	MacOS, Windows and Linux
Tools	LabView, Office Package, Corel Draw, ImageJ
Others	Origin, Gnuplot